



Michael Machhammer, Dipl.-Ing.

Tailored properties of Al-Mg-Si alloys produced through a short-term heat treatment for the application of sheet metal forming

DISSERTATION

zur Erlangung des akademischen Grades

Doktor der technischen Wissenschaften

eingereicht an der

Technischen Universität Graz

Betreuer

Univ.-Prof. Dipl.-Ing. Dr.techn. Christof Sommitsch

Institut für Werkstoffkunde, Füge­technik und Umformtechnik

Univ.-Prof. Dipl.-Ing. Dr.mont. Bruno Buchmayr
Lehrstuhl für Umformtechnik

Graz, im Mai 2017

EIDESSTATTLICHE ERKLÄRUNG

Ich erkläre an Eides statt, dass ich die vorliegende Arbeit selbstständig verfasst, andere als die angegebenen Quellen/Hilfsmittel nicht benutzt, und die den benutzten Quellen wörtlich und inhaltlich entnommen Stellen als solche kenntlich gemacht habe. Das in TUGRAZonline hochgeladene Textdokument ist mit der vorliegenden Dissertation identisch.

Datum

Unterschrift

Danksagung

Die vorliegende Arbeit wurde im Rahmen meiner Tätigkeit als Universitätsassistent am Institut für Werkzeugtechnik und Spanlose Produktion an der Technischen Universität Graz durchgeführt. Die wissenschaftliche Betreuung wurde anfangs von Univ.-Prof. Dr.-Ing. Ralf Kolleck durchgeführt, leider verstarb er unerwartet und viel zu früh. Ich möchte mich bei Ralf Kolleck für die warmherzige Unterstützung bedanken und insbesondere für die Freiheit, die mir während der gesamten Zeit am Institut gewährt wurde, was maßgeblich zum Erfolg diese Arbeit beitrug.

Besonderer Dank und Respekt gebührt Herrn Univ.-Prof. Dipl.-Ing. Dr. techn. Christof Sommitsch, der vorbehaltlos die weitere Betreuung dieser Arbeit übernahm und mich in der Schlussphase meiner Dissertation unterstützte. Ebenfalls danke ich Herrn Univ.-Prof. Dipl.-Ing. Dr. mont. Bruno Buchmayr für die Bereitschaft, als Zweitgutachter zur Verfügung zu stehen.

Für die sehr große Unterstützung bei fertigungstechnischen Aufgaben und bei der Durchführung der Umformversuche bedanke ich mich herzlich bei Heinz Fasching, Nino Müllner und Andreas Swoboda.

Ebenso geht mein Dank an meine Kolleginnen und Kollegen, die mich in den vergangenen Jahren mit bereichernden Tipps und Diskussionsbeiträgen wiederholt in neue und zielführenden Bahnen gelenkt haben. Dabei gilt insbesondere mein Dank Vladimir Bošković, Raphael Hatzer, Florian Hönsch, Christian Gasser, Michael Preininger, Philipp Reischl, Eva Keinrath und Daniela Neukam.

Eine herausragende Stellung in jeglicher Hinsicht nehmen meine Familie und meine Freundin Verena ein.

Abstract

Heat-treatable Al-Mg-Si alloys (6xxx) have a low formability compared to steel grades which are usually used for drawing operations. A promising method for the enhancement of the forming behavior of 6xxx alloys is the local reduction of strength due to a short-term heat treatment (SHT) conducted before the forming process. The SHT applied on selected areas on the initial blank, leads to a local reduction of strength aiming at the decrease of critical stress during the deep drawing process. For the successful procedure of the SHT, a solid knowledge about the crucial process parameters, such as the design of the SHT layout, the SHT process time, and the maximum SHT temperature are urgently required. It should also be noted that the storage time between the SHT and the forming processes affects the mechanical properties of the SHT area, due to natural aging. In this study, the effect of diverse SHT process parameters and various storage time-frames on the material properties and on the drawing performance is discussed and analysed. Furthermore, the influence of SHT and natural aging on the bake-hardening behaviour is evaluated. For a controlled SHT operation, a contact heating tool was developed and used to achieve near series condition, such as homogeneous temperature distributions and short heating times. A further focus in this work is the modelling of the SHT and the drawing process in a commercial FEM simulation software. Therefore, not only a thermo-mechanically coupled but also an only mechanical approach was used to model the problem. In order to prove the accuracy of both model approaches the simulation results were validated for different SHT layouts on a real part geometry.

Kurzfassung

Aushärtbare Al-Mg-Si Legierungen (6xxx) weisen gegenüber Stählen die im Bereich der Blechumformung Anwendung finden ein relativ niedriges Umformvermögen auf. Eine vielversprechende Methode zur Verbesserung des Umformverhaltens von 6xxx Legierungen ist eine Kurzzeitwärmebehandlung (SHT), die vor dem Umformprozess durchgeführt wird. SHT führt zu einer Entfestigung des Materials in ausgewählten Bereichen der Platine. Durch die inhomogene Festigkeitsverteilung der Platine können kritische Spannungen reduziert werden, um Risse im Bauteil zu vermeiden. Eine erfolgreiche Durchführung von SHT erfordert fundierte Kenntnisse über die wesentlichen Prozessparameter wie das SHT-Layout, die maximale SHT-Temperatur und die SHT Prozesszeit. Außerdem führt die natürliche Alterung von 6xxx, im Zeitraum zwischen SHT und dem folgenden Umformprozess (Lagerzeit), zu einer Veränderung der mechanischen Eigenschaften in den SHT-behandelten Bereichen. In dieser Studie wurde analysiert wie sich die unterschiedlichen SHT Prozessparameter und Lagerzeiten auf die mechanischen Eigenschaften und Umformeigenschaften der 6xxx Legierung auswirken. Des Weiteren wurde der Einfluss von SHT und der natürlichen Alterung des Materials auf die Bake-Hardening-Eigenschaften untersucht. Um eine homogene Temperaturverteilung und kurze Aufheizzeiten bei der SHT Behandlung zu erreichen wurde eine Kontaktheizung entwickelt und eingesetzt. Ein weiterer Schwerpunkt dieser Arbeit ist die Modellierung der Kurzzeitwärmebehandlung und die des Umformprozesses mittels einer kommerziellen FEM Software. Um dieses Problem modellieren zu können, wurde ein thermo-mechanisch gekoppelter und ein mechanischer Modellierungsansatz verwendet. Die Genauigkeit, beider Modellierungsansätze wurde für unterschiedliche SHT Layouts an einem Realbauteil validiert.

Table of content

1	Introduction	1
2	State of the art.....	3
2.1	Classification and application of aluminum alloys	3
2.2	Deep drawing fundamentals.....	5
2.2.1	Remedial measures for the enhancement of the limit drawing ratio	7
2.3	Forming behavior of aluminum car body sheets	7
2.3.1	Influence of EDT surface textures on the forming behavior of aluminum sheets.....	8
2.3.2	Influence of pre-coated aluminum sheets on the forming behavior	9
2.3.3	Dry film lubricants	10
2.4	Tailored blanks	10
2.5	The method of tailored heat treated blanks (THTB)	11
2.5.1	THTB of non- heat treatable aluminum alloys.....	12
2.5.2	THTB of heat treatable aluminum alloys	12
2.5.3	Conducted heating strategies for THTB.....	12
2.5.4	Design principles for THTB.....	13
2.6	Natural aging and artificial aging of Al-Mg-Si alloys.....	14
2.6.1	Enhanced artificial aging kinetics due to pre-heat treatment	16
2.7	The influence of SHT on Al-Mg-Si alloys.....	17
2.7.1	Time-temperature-profile of the SHT process.....	17
2.7.2	The influence of SHT on the conventional alloy AA6016.....	18
2.7.3	The influence of SHT on the fast hardening alloy AA6181PX.....	18
2.7.4	The influence of SHT on vertical anisotropy and the strain hardening exponent ...	19
2.7.5	The influence of SHT on artificial aging.....	20
2.7.6	The influence of the storage time on artificial aging of AA6181PX.....	21
2.8	SHT integrated in the process chain of car body construction.....	22
2.8.1	The influence of SHT on dry lubricants	22
2.9	Virtual design of sheet metal forming processes.....	23
2.9.1	Mathematical definition of the flow curve	24
2.9.2	Material modelling of the multiaxial stress state.....	26
2.10	Barlat Yld2000-2d and Hill 48 validated for AA6016T4	27
2.10.1	Influence of the SHT on the yield surface.....	28
2.11	The evaluation of sheet metal forming processes and simulations by the FLD	29
2.12	Influence of the SHT on the formability of a AA6016 alloy	30
2.13	FEM simulation of SHT on 6xxx alloys	31

Table of content

2.13.1	Mechanical approach	31
2.13.2	Thermo-mechanically coupled approach	32
3	Objective	34
4	Material and conducted methods.....	36
4.1	Investigated material.....	36
4.2	Test facilities for material characterisation	37
4.2.1	Tensile tests.....	37
4.2.2	In-plane tensile test	37
4.2.3	Planar simple shear test.....	38
4.2.4	Bulge test.....	38
4.2.5	Nakajima test.....	40
4.2.6	Quenching- and deformation dilatometer	41
4.3	SHT facility for tensile, bulge and Nakajima test samples	41
4.4	SHT facility for partial heat treatment of tensile specimens	42
4.5	Experimental methods for strain measurements	43
4.5.1	ARGUS	43
4.5.2	ARAMIS	43
4.6	Determination of the heat transfer coefficient (HTC).....	44
4.7	Forming facility and part geometries	45
4.7.1	Deep drawing tools	45
4.7.2	Forming behaviour of the defined geometries	46
4.8	SHT facility for the production of THTB	47
4.8.1	Design of the SHT layouts	47
4.8.2	Construction of the SHT facility	48
4.8.3	Evaluation of the temperature distribution.....	49
5	Material characterisation - SHT temperature and paint baking.....	52
5.1	Characterisation of the optimal SHT temperature	52
5.1.1	Process control of conducted heat treatment and material tests.....	52
5.1.2	Measurement results - mechanical properties	53
5.2	Investigation of the effect of natural aging on the paint baking response.....	54
5.2.1	Process control of conducted heat treatment and material tests.....	54
5.2.2	Measurement results - mechanical properties	55
5.3	Summarizing evaluation of the analysed SHT process parameters	57
6	Material characterisation - FEM simulation.....	58
6.1	Mechanical parameters and flow curves.....	58
6.2	Forming limit curve (FLC)	59

Table of content

6.3	Heat transfer coefficient (HTC)	60
7	The influence of the SHT on the dry lube and its consequences on the drawing performance.....	61
7.1	Process control experiment	61
7.2	Measurement results.....	62
7.3	Conclusion.....	63
8	Analyses of the influence of SHT process parameters on the drawing performance	64
8.1	Experimental procedure SHT and forming	64
8.2	Investigation of different SHT temperature levels	67
8.3	Evaluation of different SHT layouts	68
8.4	Investigation of different holding times	69
8.5	Investigation of different storage times.....	70
8.6	Determination of the maximum drawing depth	72
8.7	Conclusion.....	72
9	Analyses of the influence of SHT and paint baking on the final part properties.....	74
9.1	Process control and used process parameters.....	74
9.2	Forming result multi-stage process	75
9.3	Mechanical properties of the drawn part.....	75
9.4	Conclusion.....	77
10	FEM simulation model	78
10.1	Material modelling	78
10.1.1	Mechanical approach.....	78
10.1.2	Thermo-mechanical coupled approach.....	79
10.1.3	Modelling of the yield locus through Barlat1989 and Barlat-Yld2000-2d.....	82
10.2	SHT simulation of a partial heat treated tensile specimen	84
10.2.1	FEM Simulation model – input parameter	84
10.2.2	Validation and discussion of the simulation results	84
10.3	SHT simulation and forming simulation	86
10.3.1	Validation and discussion of the simulation results	88
10.4	Summarizing evaluation of the analysed simulation model.....	92
11	Summary and Outlook.....	93
	References.....	95

Symbol directory and list of abbreviations

Symbol	Unit	Description
A	MPa	Physical parameter (hardening law)
a		Hocket-Scherby parameter
B	MPa	Physical parameter (hardening law)
b	-	Hocket-Scherby parameter
C	-	Free parameter (hardening law)
c	-	Hocket-Scherby parameter
D_{blank}	mm	Diameter blank
D_{punch}	mm	Diameter punch
d	-	Hocket-Scherby parameter
d		day
d_L	mm	Laser spot diameter
d_m	mm	Diameter of wall section
d_p	mm	Outer diameter of the flange when maximum drawing force has been reached
E_f	-	Elongation at fracture
E_u	-	Uniform elongation
F	N	Punch force
F_N	N	Blank holder force
h		hour
I	-	Free parameter (hardening law)
k_{fm1}	MPa	Average yield stress in flange section
k_{fm2}	MPa	Average yield stress in the radius section
m	-	Parameter of Barlat yield criterion to define the shape of the yield locus
n	-	Hardening exponent (hardening law) or number of conducted experiment
μ	-	Coefficient of friction
p	bar	Oil pressure during bulge test
R	mm	Bulge radius
R_a	μm	Roughness of surface
R_p	MPa	Yield strength
r	-	Lankford parameter
$r_{0,45,90}$	-	Lankford parameter determined at 0°, 45° and 90 ° to the rolling direction
r_R	mm	Draw ring radius radius
s_0	mm	Sheet thickness
t_0	mm	Sheet thickness of bulge specimen
T	°C	SHT temperature (linear interpolation)
T_{crit}	°C	SHT critical temperature
T_E	°C	SHT end temperature
T_{max}	°C	Maximum temperature during SHT
T_s	°C	SHT start temperature
t_1, t_t	mm	sheet thickness 1 and 2
t	mm	Sheet thickness measured in the middle of the bulge
v_L	m/s	Velocity of laser

Symbol directory and list of abbreviations

α_{1-2}	-	8 coefficients of the Barlat YLD2000 yield criterion
β	-	Drawing ratio
β		Precipitation in shape of platelets
β'		Bar-formed precipitation
β''		Needle formed precipitation
β_{heating}	K/s	Heating rate
β_{cooling}	K/s	Cooling rate
$\Delta\varepsilon$	-	Gap between maximum major strain and forming limit curve
$\Delta\sigma$	MPa	Amount of reduced strength through SHT
ε_p	-	Plastic strain
ε_p^0	-	Plastic strain (pre-strained)
$\dot{\varepsilon}$	1/s	Strain rate
λ	W/mK	Thermal conductivity
φ' and φ''	-	Convex function of deviatoric stress tensor
φ_1	-	Strain in direction x
φ_2	-	Strain in direction y
φ_t	-	Strain at the largest degree of thinning
φ_v	-	Equivalent strain
σ_f	MPa	Flow stress
σ_b	MPa	Biaxial stress
σ_0	MPa	Yield stress under plane stress condition
$\sigma_{1,2}$	MPa	Component of principle stress tensor (0° and 90° to the rolling direction)
σ_{12}	MPa	Component of principle stress tensor (shear stress)

ASTM	American society for testing and materials
BCC	Body-centred cubic materials
COF	Coefficient of friction
DFL	Dry film lubricants
DSC	Differential scanning calorimetry
EDT	Electro discharged texturing
FEM	Finite element method
FCC	Faced-centred cubic materials
FLC	Forming limit curve
GP	Gunier Preston
HTC	Heat transfer coefficient
SHT	Short-term heat treatment
THTB	Tailored heat treated blanks
UTS	Ultimate tensile strength
YS	Yield strength

1 Introduction

One of the central goals of the global community, is reducing greenhouse gas emissions [1]. To achieve this aim, research and development is conducted in different economic sectors, to optimize processes and to develop new technologies aiming to decrease the greenhouse gas emissions. Economic activities which lead primarily to greenhouse gas production are the sectors of transportation, electricity and heat production, agriculture, forestry and industry [2]. Especially in regards to the sector of transportation, the further advancement of light weight design of the vehicle is essential for the reduction of CO₂-emission. Figure 1 shows that light weighting of a car is the second best measure for the reduction of consumption beside the enhancement of the drivetrain, the aerodynamic resistance and the rolling resistance [3].

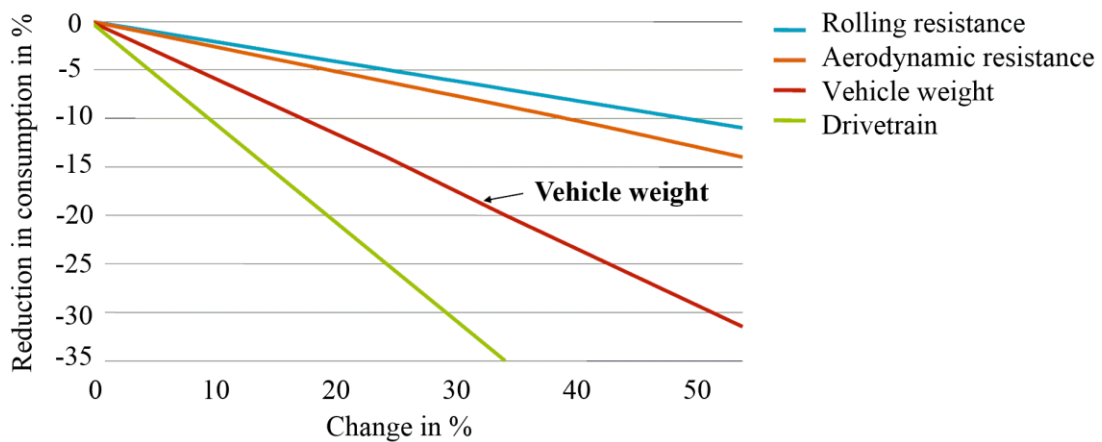


Figure 1 Light weighting is the 2nd best measure for emission reduction [3]

Additionally the light weighting of cars leads to a lower inertia of the vehicle, which has a positive influence on the driving dynamics [4]. Due to the beneficial terms of performance and environmental impact, the trend to using lighter materials in cars is increasing over time [5]. Figure 2 clearly demonstrates this increase of the materials which are used for light weight car design, such as aluminum, high strength steel, polymers and magnesium, compared to conventional steel grades [6].

Approximately one-quarter of the overall vehicle mass consists of the car body and closure parts [7,8]. Therefore, it proves efficient to reduce the weight of these components when a mass-optimised design of cars is required. An effective approach to reduce the weight of the body and closure parts, is the substitution of low-alloyed steel grades by lightweight materials, such as aluminum [9]. It is significant to point out that the car body of premium vehicles already includes 20%, sometimes even-up to 30% of aluminum [10,11], which leads to a significant weight reduction of approximately 20% to 40 % compared to the conventional design [12,13].

A substantial proportion of body and closure parts is manufactured through a sheet metal forming operation [14]. It should be noted that aluminum sheets have a lower plastic anisotropy compared to steel grades, which is an indicator for the drawability of sheet metal materials [15,16]. A low plastic anisotropy means that the material has a poor resistance against thinning when plastic deformation is conducted [17].

Therefore, the substitution of low alloyed steel grades by aluminum does, in fact, not result in manufacturing processes which show high-quality and robustness [18,19].

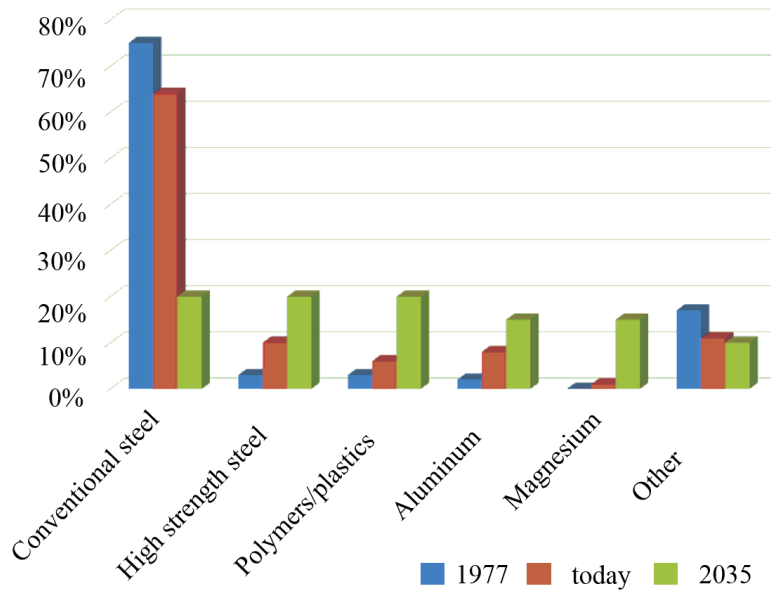


Figure 2 Material mix in cars over time [6]

In order to guarantee high-quality and robust processes, it is absolutely necessary to consider all crucial elements which are affecting the manufacturing system, such as the properties of the forming material, the process design of the manufacturing operation and the final part properties. A promising method to improve the drawing properties of the forming material of heat treatable aluminum alloys, is the local reduction of strength due to a short term heat treatment (SHT), conducted before the forming process [20].

The technological challenge to implement the SHT in the manufacturing system is the sound knowledge of the SHT process parameters and their influence on the drawing and artificial hardening performance, as well as its consequences on final part properties. Also, the use of computer aided process designs, which show an excellent agreement with the real manufacturing process, is absolutely essential for high-quality and robust manufacturing processes of the SHT

2 State of the art

2.1 Classification and application of aluminum alloys

Over recent years a considerable increase in the use of aluminum alloys can be detected, specifically due to the good properties in low density, high specific strength and stiffness, corrosion resistance and adequate formability [21,22]. Aluminum alloys are developed by alloying aluminum with other materials such as manganese, magnesium, silicon, copper, tin, and zinc. Thus, mechanical properties are optimized for various fields of applications, by the use of different alloying compositions. These alloys are divided into wrought and casting materials. To be specific, a characteristic of wrought aluminum alloys is its ability of plastic deformation, whereby casting materials are adjusted for the mould-filling capacity. Depending on how the hardening of the required strength is conducted, by cold working or heat treatment, aluminum alloys are categorized into non-heat-treatable or heat-treatable aluminum materials [23].

The identification of the alloy type is clarified through a four-figure numerical code. The main alloying element is identified by the first number, and the last three numbers are classifying the specific alloy more detailed, especially recognizing the alloying composition. An overview, which provides information about the differentiation of aluminum alloys through the main alloying elements and the associated areas of application, is presented in Table 1.

Table 1 Alloy type of aluminum with regard to their properties and field of application [23]

groupe	alloy type	hardenable	application
1xxx	pure aluminum	no	packing foil, road signs..
2xxx	Al-Cu	yes	aircraft construction, shipbuilding..
3xxx	Al-Mn	no	packing industry, heat exchanger..
4xxx	Al-Si	yes/no	heat exchanger, machinery industry..
5xxx	Al-Mg	no	body construction (car), facades, shipbuilding..
6xxx	Al-Mg-Si	yes	body construction (car), shipbuilding...
7xxx	Al-Zn-Mg	yes	aircraft construction

It has to be noted that for the calibration of the material's properties, additional alloying elements are used, which are neglected in Table 1, due to their low percentage, compared to the main elements. Furthermore, the four-figure numerical code can be complemented by capital letters in order to inform about the microstructure (-O), the conducted heat treatment (-T) or strain hardening (-H). Particularly the group of the hardenable aluminum alloys is characterized through T and divided by the following numbers ranging from 1 to 9 (Table 2) [23].

Table 2 Overview of the relevant material condition with regard to the conducted heat treatment [24]

condition	
T1	hot rolled + quenched + natural aging
T2	hot rolled + quenched + cold rolled + natural aging
T3	solution annealed + quenched + cold rolled + natural aging
T4	solution annealed + quenched + natural aging
T5	hot rolled + quenched + artificial aging
T6	solution annealed + quenched + artificial aging
T7	solution annealed + quenched + artificial overaged
T8	solution annealed + quenched + cold rolled + artificial aging
T9	solution annealed + quenched + artificial aging + cold rolled
T10	hot rolled + quenched + cold rolled + artificial aging

The car body construction these days primarily focuses on semi-finished products of aluminum cast, profiles and sheet metals. For sheet metal alloys, for example, the alloy composition of Al-Mg (5xxx) and Al-Mg-Si (6xxx) is commonly used in car bodies [25]. One of the advantages of alloys of the group 6xxx is that the material can increase its strength through a heat treatment after the conducted forming process, by artificial aging (i.e. paint baking). Moreover, alloys of the group 6xxx are free of flow lines compared to the alloys of the group 5xxx. Due to the possibility of an increase in strength by a heat treatment and the unsusceptible behavior of flow lines, alloys of the group 6xxx are mainly used in the European automotive market [4]. Therefore, Table 3 shows an overview of the most used aluminum alloys of the group 6xxx and their field of application in car body construction. The letters PX are used to characterize the material that has the ability of fast hardening.

Table 3 Aluminum alloys of the group 6xxx which are often used in the car body [4]

condition	application
AA6016PX	outer panels
AA6014PX	outer panels with high cupping requirements
AA6111T4	outer panels with high strength requirements
AA6181T4	inner panels
AA6014T4	structural parts
AA6501T4	inner parts, pedestrian protection

2.2 Deep drawing fundamentals

The deep drawing process is one of the most important manufacturing processes for the production of complex sheet metal parts in the industrial field [26]. The application of deep drawing is widely used for small and major serial products in the metal processing industry, as well as for mass production in the packing industry. According to DIN 8584, deep drawing is categorized as tensile compression forming of a sheet metal without the interest of modifying the sheet thickness [27]. The process principle of the deep drawing process is described through the forming of a circular blank into a simple cylindrical cup geometry in Figure 3.

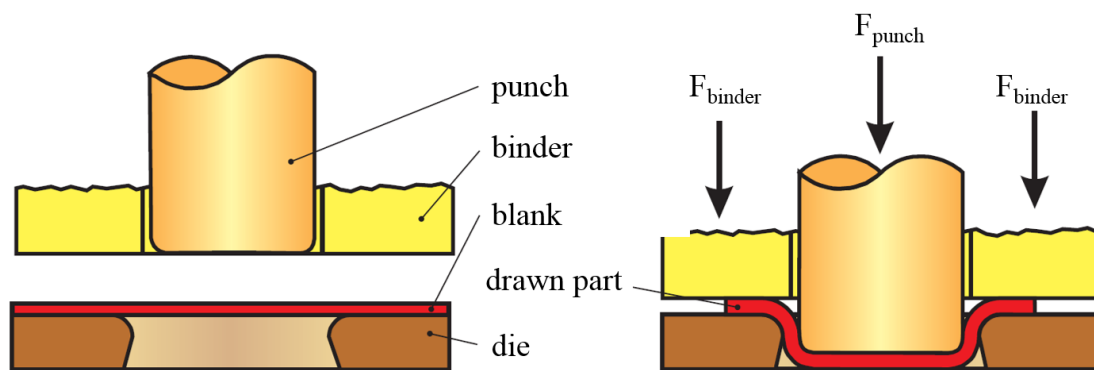


Figure 3 Deep drawing with a binder [28]

Thereby, the cut sheet (blank) is clamped between the draw ring (die) and the blank holder (binder) with the purpose of being formed over the punch. The relative movement of the punch and die brings the flat blank into shape. When forming is conducted, the initial diameter of the blank is continuously decreasing with the increase of the drawing depth. While the part is formed, different stress states can be assigned to the geometry of it. In the area of the flange, tangential compression stress occurs due to the material flow to a smaller diameter. Consequently, this stress state leads to a wrinkling of the material which needs to be controlled by applying a binder force on the blank. The wall area is stressed by a uniform load state, which means that the material is hindered in the direction of minor strain. Thus, stretch forming occurs in the bottom area of the part through a biaxial load state. The force which is required for the plastic deformation of the material's flange section is applied through the punch on the bottom side of the part. The load path, initiated by the applied force, moves from the bottom and wall section into the area of the flange. Therefore, the bottom and wall area is defined as the force transmission zone and the flange area, the so-called forming zone (Figure 4) [29].

In addition to the wrinkling of the material, the appearance of splits in the wall or bottom area of the part is further characteristic of the process boundary in terms of the process design of deep drawing operations. However, the phenomenon of wrinkling can be avoided by increasing the binder force. Simultaneously, by increasing the binder force, the possibility of material failure through splits (cracks) also increases. To illustrate, Figure 4 shows a schematic representation of the interaction between binder force and the wrinkling and appearance of splits. In the presented scheme, a binder force can be applied in a defined range without producing splits or wrinkles during the forming.

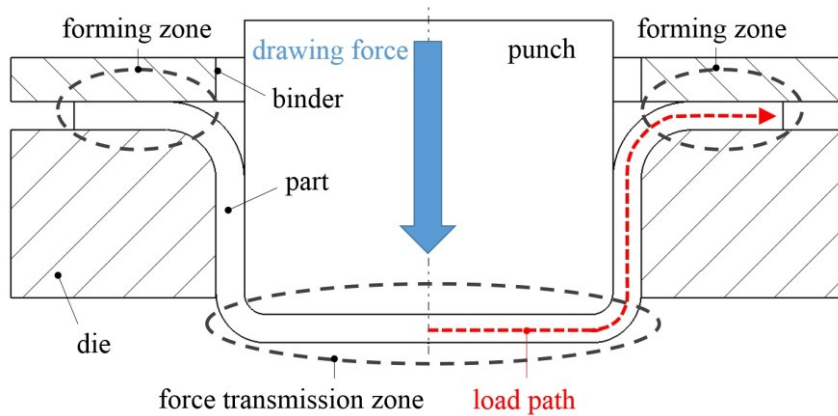


Figure 4 Representation of the forming zone, force transmission zone and load path

In brief, if the binder force is too low, wrinkles will occur. The maximum achievable drawing depth without the occurrence of material failure can be obtained through an optimal binder force (Figure 5). The principle in Figure 5 can also be applied to more complex part geometries, which have the characteristic areas, such as flange, wall and bottom [25].

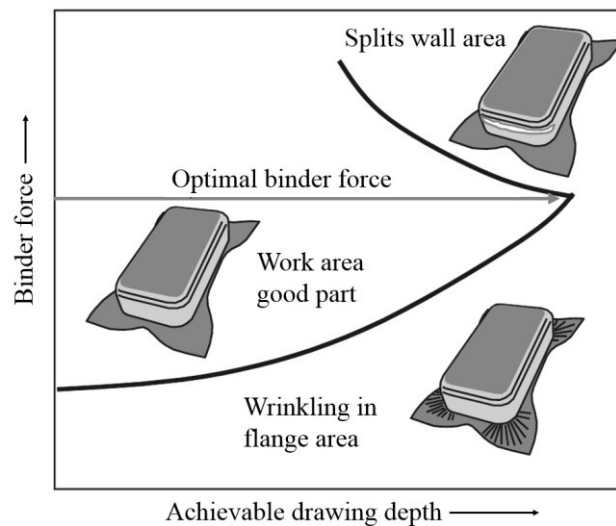


Figure 5 Operational diagram for the adjustment of binder force for a rectangular shaped cup [30]

A relevant parameter for the design of simple cup (i.e. rotationally symmetric, rectangular and oval blank geometries) drawing parts is the limit drawing ratio β (equation 1). To be precise, the limit drawing ratio β defines the allowed maximum blank diameter, by a given punch diameter, which can still be drawn without producing cracks in the wall section of the part [25,31].

$$\beta = \frac{D_{blank}}{D_{punch}} \quad [29] \quad \text{Equation 1}$$

By increasing the blank diameter the forming zone also increases, however, only if the punch geometry stays constant. A larger forming zone requires a higher drawing force in order to achieve plastic deformation. Due to the larger drawing force, the stress in the wall section is consequently higher, which leads to early crack deformations when the critical stress value is reached. In this sense, for every

specific combination of relevant process parameters, there is one specific drawing ratio. The following process parameters are influencing the drawing ratio for deep drawing processes [25]:

- Material
- Sheet thickness
- Tribological properties (sheet surface, tool surface, lubrication, etc.)
- Punch and die radius
- Gap between punch and die
- Binder force

2.2.1 Remedial measures for the enhancement of the limit drawing ratio

The enhancement of the forming limit of deep drawing processes requires the same measures which are needed for a higher limit drawing ratio. These measures are also crucial for lowering the deep drawing force.

This can be realized through the reduction of the work of deformation in the forming zone, for instance through

- heating the flange area in order to decrease the yield stress,
- reduction of the dissipation due to minimization of friction in the flange area and drawing radius by the use of lubricants,
- reduction of the work of bending, through increasing the die radius,

and by optimizing the force transfer mechanisms in the wall section, for instance by

- higher friction force between punch and wall due to a rougher punch surface, and
- higher friction force between punch and wall due to a higher contact pressure between wall and punch, for instance through hydromechanical deep drawing.

With the exception of the optimized die radius and the reduction of friction in the flange section, due to the use of coated tool surfaces and targeted lubrications, these measures are not used in practice to improve the drawing process of car body parts. However, those fundamental aspects/characteristics are essential for the sound understanding of the complex factors of a real deep drawing process in order to define the right measure in the process of optimization [25].

2.3 Forming behavior of aluminum car body sheets

The forming behavior of aluminum car body sheets was investigated by Dinkel [32]. It is noted that, compared to steel, aluminum sheets have a fundamentally different forming behaviour. For instance, the values of the uniform elongation of aluminum sheets are similar to steel sheets, but simultaneously, aluminum shows a much smaller uniform elongation region. Steel grades also have a higher plastic anisotropy, compared to aluminum sheets, which is an indicator of the drawability of sheet metal materials [15–17,33]. For Dinkel, the crucial element for the car body sheets' successful processing is a sufficient consideration of their properties and boundaries with regard to the tooling and the sheet metal forming process.

These properties and boundaries are:

- The technical achievable deep drawing results of aluminum sheets are lower compared to steel grades.
- Essentially, compared to steel, more steps at the multi-stage drawing operation are necessary when aluminum sheets are used.
- Highest surface quality of the forming tools is required.
- Drawing gap must be larger if aluminum is formed.
- Lowest possible blank holder force is necessary.
- Drawbeads which are used for sheet metal forming operation of steel blanks cannot be adapted for aluminum sheet metal forming processes. Therefore, drawbeads must be adjusted to the lower formability of aluminum materials.

Due to the lower formability of aluminum, Siegert [34] has noted that it is certainly necessary to exploit all the available potential of the process and the semi-finished product, to ensure a high feasibility of car body parts. This means that the enhancement of the tribological system of the sheet metal forming process and the tailoring of the semi-finished product [35], has a relevant impact on the drawing performance.

The phenomenon of friction, between the formed sheet metal and the forming tool, occupies a significant role in regards to the feasibility of complex part geometries, and calls for a targeted modification, aiming to enhance the forming conditions (2.2.1). The improvement of the forming process due to the optimized tribological system, was recently achieved by the availability of pre-coated aluminum sheets and a large spectrum of surface qualities [32].

2.3.1 Influence of EDT surface textures on the forming behavior of aluminum sheets

Normally, the surface of an aluminum sheet after it exits a rolling mill, is not target textured but has a surface texture, which is called mill finish (MF (Figure 6-left).

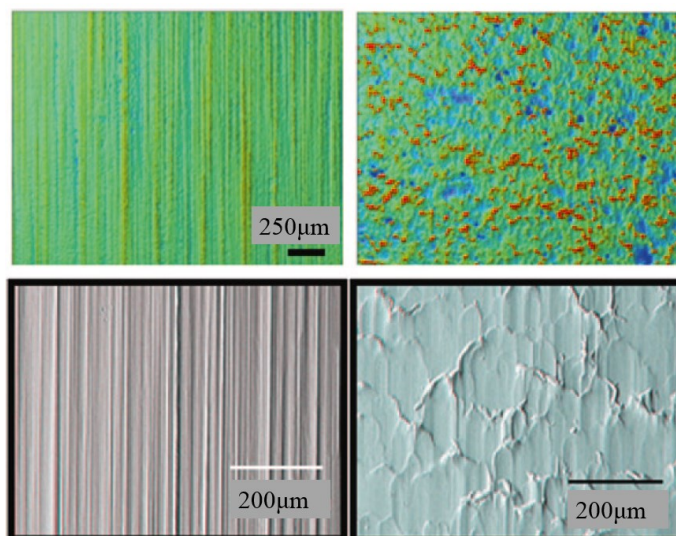


Figure 6 left: Mill finish texture; right: EDT texture [4]

Through targeted surface morphologies of higher roughness, the forming properties of aluminum sheets can be positively influenced [32,36–38]. For instance, the forming and friction behavior of electro discharge texturing (EDT) (Figure 6-right) surfaces, which have a value of roughness of about $R_a > 1 \mu\text{m}$, are less dependent on the viscosity of the used lubricant. These kinds of surfaces are roughening less during forming and have the ability to be properly lubricated due to a uniformly high level of smoothening. Furthermore, the obtained isolated pockets through EDT serve as a reservoir for lubrication, which is beneficial for the forming. In addition, EDT sheets have a higher volume of closed lubricant pockets, compared to mill finished sheets, resulting in less sensitivity to galling. Despite the higher coefficient of friction (COF) of EDT surfaces (Figure 7) compared to mill finish surfaces, the rougher surface enables a higher capacity for lubricants. Consequently, the use of lubricants which show a low-viscosity, results in an enhanced drawing performance. High viscous lubricants show better drawing properties when surface qualities with $R_a < 1 \mu\text{m}$ are used [39].

2.3.2 Influence of pre-coated aluminum sheets on the forming behavior

Due to coil-coating, a completely new micro texture is generated. Hence, a new type of texture, with an isotropic characteristic and a high COF (Figure 7), is produced. For instance, the pre-coating, which consists of zinc-rich primers (Bonazinc), has a rough and heavily rugged texture, which shows a high capacity for the needed lubricants. The drawability of bonazinc coated sheets strongly depends on the properties of the lubricant viscosity. Blanks coated with high-viscosity lubricants show an enhancement towards untreated surfaces in the deep drawing performance. By using low viscosity lubricants, lower deep drawing properties, compared to uncoated blanks, can be achieved. Characteristic of the friction behavior of Bonazinc coated blanks, is the relative constant COF at the forming operation [32].

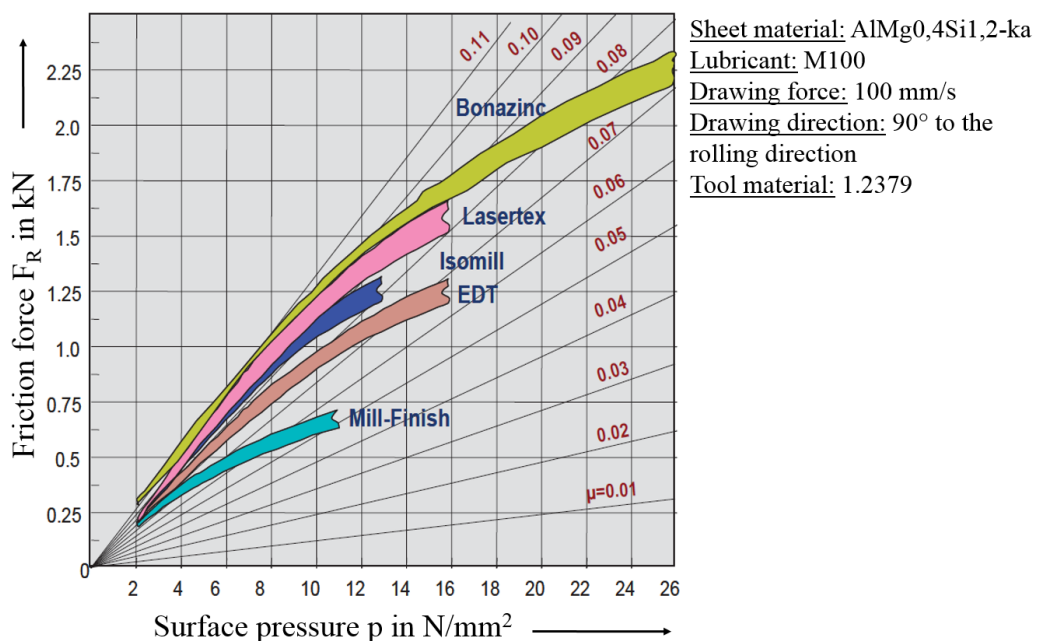


Figure 7 Behaviour of friction of various aluminum sheet surfaces determined through strip drawing test [40]

2.3.3 Dry film lubricants

Lubricants for sheet metal forming operations are categorized into oil-based liquid lubricants and dry film or coil lubricants (DFL). The group of oil-based lubricants can be divided into mineral oils or emulsions. Dry film lubricants are distinguished into water-soluble dry film lubricants and water-free dry film lubricants. Water-soluble dry film lubricants are applied to the rolling mill in the amount of $0.5\text{-}1.5\text{ g/m}^2$. Furthermore, these lubricants possess excellent properties for corrosion protection, but do not operate with most adhesives used in car body construction. Water-free dry lubricants are coated, similarly, in a small amount on the sheet surface, such as water-soluble dry film lubricants. A benefit, when using water-free dry lubricants, is not only the compatibility with adhesives, but also a good drawing performance. The application of DFL in sheet metal forming processes, especially in the area of car body construction, is widely used due to enhanced performances in deep drawing, cleanliness and reduced requirements for recycling and disposal [38,41].

Furthermore, DFL provides [41,42]:

- a homogeneously distributed coating thickness on the sheet surface,
- less amount of DFL ($0.5\text{-}1.5\text{ g/m}^2$) to be needed, compared to oil-based lubricants ($1.5\text{-}3.0\text{ g/m}^2$),
- the possibility of neglecting the washing process which is absolutely paramount when oil-based lubricants are used,
- compatibility with joining processes, such as welding, bonding, clinching and riveting, and
- minimal environmental compliance.

2.4 Tailored blanks

In general, tailored blanks are sheets which have an inhomogeneous distributed sheet thickness or mechanical properties. As a result of the possibility of specific adjustable local properties of the sheet, an enhancement of the formability and functionality of the final part becomes feasible. Thus, the use of tailored blanks, with differently adapted sheet thickness, has the advantage of a significant reduction of weight and material costs.

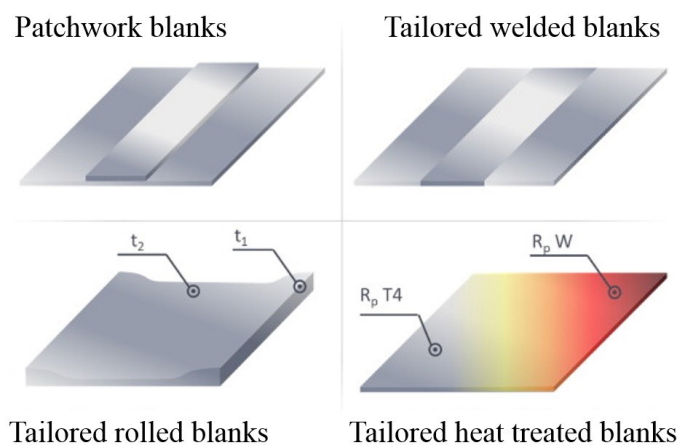


Figure 8 Classification of tailored blanks [43]

For instance, only the highly loaded areas of the part require a higher sheet thickness, whereby all zones, which are dealing with minor loads, are showing a reduced sheet thickness in order to minimize weight and costs. Essentially, tailored blanks can be categorized into four different technologies: patchwork blanks, tailored welded blanks, tailored rolled blanks and tailored heat treated blanks (Figure 8).

Tailor welded blanks are sheets with different properties joined through welding operations. Usually, sheets with various sheet thicknesses or materials are used, with the aim to produce parts with a specific characteristic in terms of strength, crash performance and weight [44,45].

A further technology which provides locally modified material properties, is the so-called patchwork blanks [46]. In regards to the production of patchworks blanks, patches are fixed through spot welding, laser welding or bonding on the basic sheet. Because of the modified sheet thickness and material combination, the patch locally increases strength and stiffness [47].

The method of tailored rolled blanks modifies the sheet properties through flexible cold rolling of the blank. The flexible cold rolling leads to an inhomogeneous distribution of the mechanical properties due to the cold working and the reduction of sheet thickness [48]. In addition, the special design of the rollers ensures a smooth transition of the change in sheet thickness, and prevents concentrations of stress, which occur in the notch of tailored welded blanks [49].

In brief, “Tailored heat treated blanks” (THTB) is a production technology which uses local modified material properties along the sheet plane, aiming to improve the forming limit [50]. To be precise, the principle of THTB is based on the selective reduction of the yield strength in the forming zone. Thus, the needed drawing force (punch force) is decreasing, while the initial strength in the force transmission zone (often the critical area) stays constant. The result is an improved material flow and the lowering of the critical stress, where failure may occur during forming. The approach of THTB works differently compared to warm forming and hot forming technologies. When THTB is used in order to improve the formability of blanks, the needed heat treatment is conducted in a separated process step before the actual drawing operation. To be more specific, it means that the blank is formed at room temperature under cold forming conditions. The ability to carry out cold forming instead of warm forming is the key advantage to using lubricants and tools which are designed for the conventional cold forming process [43]. Based on this technological principle several scientific investigations were performed.

2.5 The method of tailored heat treated blanks (THTB)

The first basic research on the technology of THTB was conducted by Siebel and Beisswanger in 1953 [51]. In this research study, the materials steel (St8, V2AE), brass (CuZn37), aluminum (Al 99,7) and nickel silver were used. Thereby, in the first step of the experiment, circular blanks were strain hardened through cold rolling. In the second operation, in order to obtain an inhomogeneous strength distribution, the flange area (forming zone) was softened by recrystallization. The softening was carried out through the use of a simple welding torch conducted in a temperature range of 500°C to 1000°C. Thus, the deep drawn circular blanks reached a significantly higher limit drawing ratio than the blanks which had a homogeneous strength distribution. Although the enhancement of formability, as a result of the local heat treatment, was proven through this study, the method was not industrially implemented. The essential reason for this is not only the intensive process, but also the non-robust heat treatment. However, further investigations were focused on the application of THTB on steel and aluminum.

2.5.1 THTB of non- heat treatable aluminum alloys

For non- heat treatable aluminum alloys, such as 5xxx, Hogg and Liewald found that the modification of strength is possible through a local heat treatment [52]. In order to obtain this, a solution annealed state of the non- heat treatable aluminum is needed. To be more specific, a heat treatment temperature of about 500°C to 540°C and a holding time of around 30s are required during the heat treatment procedure. Also THTB for multi-stage forming operations was successfully tested on non- heat treatable aluminum alloys. Due to the high temperature and holding time, heating methods, such as conduction or induction, are required [53].

2.5.2 THTB of heat treatable aluminum alloys

Heat treatable aluminum alloys, such as the group of 6xxx, are more suitable for the application of THTB than 5xxx alloys. The local softening of those materials is achieved by the reduction of strength through a reversible dissolution of the precipitation structure [54]. In 1941 Haase [55] already discovered that contrary to the heat treatment of 5xxx, the softening of 6xxx can be conducted through a short term heat treatment (SHT).

2.5.3 Conducted heating strategies for THTB

The most commonly conducted methods for the procedure of the SHT are based on radiation, heat conduction and heat induction. Heating through radiation, for instance by laser technology, has the advantage of short set-up times and a very flexible system, which is beneficial for the try-out of different SHT-layouts. Indeed, the advantage of heating through induction or conduction (contact plates) is the ability to achieve short cycle times of the heat treatment procedure, as a result of the concurrent heating of the complete SHT layout (Figure 9). Due to the beneficial terms of flexibility and short set-up time, laser technologies are particularly suitable for the prototype manufacture, small-scale production, and research of THTB. Otherwise, the SHT conducted, resulting from the contact heating, fulfils all requirements for mass production of THTB. Moreover, the use of contact heating ensures a homogenous temperature distribution in the softened zone, a high reproducibility, as well as the ability to realize defined holding times (Figure 9).

During contact heating the blank is heated by contact plates from both sides, as opposed to the SHT which is carried out through laser or inductive heating technologies. Scientific investigations have demonstrated that blanks, which have a smaller sheet thickness than 1.5 mm, are suitable for one side heating approaches, such as laser or induction [54]. If the sheet thickness stays in a range of 1.5 mm, a fast and homogeneous heat treatment can be guaranteed. This means that on the bottom and top of the blank's surface the temperature during the SHT is nearly identical [54].

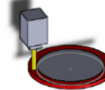

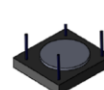
	unfavorable ← ---	favorable → +++	Laser 	Induction 	Heat conduction 
Heating rate			+++	+++	++
Homogenous temperature distribution				--	+++
Reproducibility			0	-	+++
Possibility of a holding time			---	-	+++
Investment cost - machine			---	0	0
Investment cost - tool			+++	--	--
Set up time			+++	--	0
Productivity			--	+++	+++

Figure 9 Overview of the used heating technologies for the application SHT [56]

2.5.4 Design principles for THTB

A crucial element of the SHT process is the design of the SHT layout. Along those lines, Geiger and Merklein [50] derived design principles for the layout of SHT through the evaluation of different layout combinations on simple deep drawing parts. The different SHT layouts were realized through the use of an ND:YAG laser, with a defocused optic and the ability to use variable laser spot diameters. The conducted SHT layouts were evaluated based on the decrease of the punch force and the increase of the maximum drawing depth. Based on the local modified areas of a THTB, two fundamental active principles were categorized into the force oriented, and, into the material flow oriented principle (Figure 10) [50].

The first active principle is based on the reaction forces, which do occur during the forming process along a load path of a drawn part. The source of these load paths is located in the force transmission zone, more specifically, in the region of the punch, and finally ends in the forming zone (flange area). The highest reaction forces along the load path are mostly found in the forming zone, due to the highest work of plastic deformation. This is derived from the notion that the punch force, which is assigned to the work of deformation, essentially presents the largest component of force. Thus, if plasticized areas are softened by a local heat treatment, the needed work of deformation also decreases. This leads to the lowering of reaction forces along the load path, and consequently to the decrease of stress in critical zones where failure may occur during the forming operations. Due to the lowered stress situation, the possibility that the ultimate tensile strength exceeds locally and, consequently, the occurrence of cracks is reduced. For instance, SHT conducted in the flange area (forming zone) of a simple cup geometry leads to lowered reaction forces along the load path, this means that also the stress in the critical cup radius is reduced (1. active principle). The decrease of the punch force, through the reduction of the flow stress in the flange area, can also be described through equation 2, derived from Siebel [57]. By using equation 2, the punch force, which is needed for the drawing process of a cup geometry, can be calculated. Apparently, due to the reduction of the averaged flow stress k_{fm1} (average flow stress in the section of the flange), the punch force is also decreasing [50].

$$F = \pi d_m s_0 \left[e^{\mu \frac{\pi}{2}} \left(1, 1 k_{fm1} \ln \frac{d_p}{d_m} + \frac{2\pi F_N}{\pi d_p s_0} \right) \right] + k_{fm2} \frac{s_0}{2r_R} \quad [57] \quad \text{Equation 2}$$

Within the second active principle, softened zones are not intended to reduce the punch force of the forming process in order to reduce critical stresses. However, due to the lower strength level in the heat treated zones of THTB, the plastic deformation of the material starts earlier, compared to the zones located in the untreated area. This flow behavior can be controlled through the right positioning of the softened zones located near the critical spots, aiming to enhance the material flow to the critical areas.

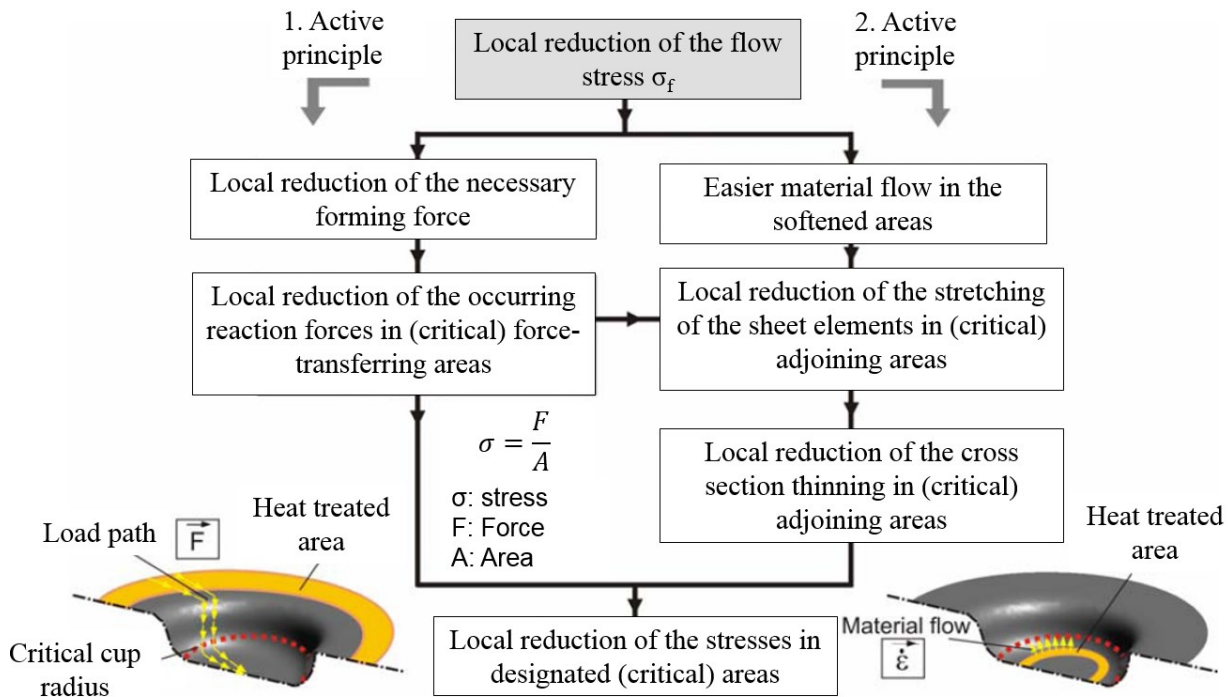


Figure 10 Active principles of local softened areas of THTB [50]

The softened zones in the second active principle can also be seen as so-called “sacrificing zones”, which underlie higher thinning for the benefit of the critical areas. Through this principle, strain in the critical area is reduced and therefore thinning and stress is minimized.

For instance, a circular softened zone of the bottom area of a cup geometry can serve as a sacrificing zone in order to increase thinning with the aim to reduce critical stress and the reduction of the sheet thickness in the critical radius area (Figure 10). Out of these two active principles the most essential design principle can be derived. To avoid a decrease of the formability, when SHT is used, it is absolutely essential that critical zones are not allowed to be modified. Because the softening of critical zones would lead to an earlier appearance of cracks [50].

2.6 Natural aging and artificial aging of Al-Mg-Si alloys

Aluminum alloys of the group 6xxx are alloyed through the main alloying elements magnesium (Mg) and silicon (Si). In the European automotive sector the standard alloys AA6016 and AA6181 of the group 6xxx are commonly used [58]. An increase in strength of these alloys can be achieved via decreased solubility of silicon and magnesium, by falling temperatures, and the thereby related precipitation of the

intermetallic Mg_2Si phase. These alloys have a surplus of silicon, which lead to a fast response during the artificial aging procedure, as well as an increase of strength [59]. The heat treatment procedure, which is used to adjust the final strength of the material, is presented in Figure 11. Therefore, the solution heat treatment is conducted after the cold rolling process in a time period of circa 1 hour and in a temperature range of $500^{\circ}C - 580^{\circ}C$. This heat treatment activates a substantial dissolution of the Mg_2Si phase. The subsequently quenching process after the solution heat treatment results in a supersaturation, and consequently amounts to a thermodynamically unstable state (condition-W). It should be noted that this unstable state is essential for the aging processes of heat treatable aluminum sheets [60].

The precipitation sequence for Al-Mg-Si alloys of a conventional artificial aging procedure is made up as follows (Figure 12) [38,61]:

Supersaturated solid solution \rightarrow clusters and/or Guinier Preston I (GP-I) zones \rightarrow GP II zones (β'' - needle-formed) \rightarrow β' bar-formed \rightarrow β platelets (equilibrium phase of Mg_2Si)

If the artificial aging process is conducted with temperatures lower than $70^{\circ}C$, only GP-I zones are formed. Thus, this state is comparable to the condition of natural aged materials. Natural aging is conducted after the quenching process, at room temperature, in a time period of 14 days. In this time frame finely distributed $MgSi$ -clusters are built in the material's micro structure, which are also named the Guinier-Preston-zones (GP-zones). To be more precise, GP-zones are coherent finely distributed precipitations which are responsible for the distortion of the aluminum matrix.

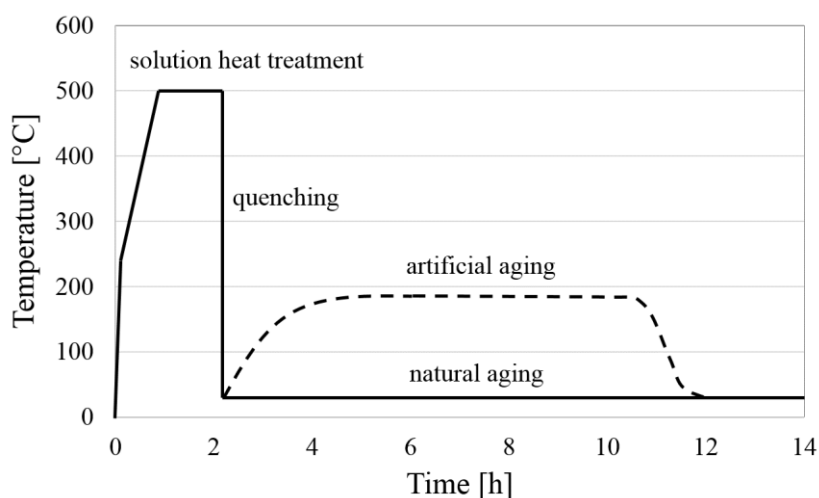


Figure 11 Scheme of the heat treatment of heat treatable aluminum alloys [62]

By the distortion of the aluminum matrix the dislocation motion is disrupted and thus the material strength increases [63]. The GP-II zones, which lead to higher strengthening, are obtained through artificial aging at a temperature of around $170^{\circ}C - 210^{\circ}C$, during a heat treatment process of 2 to 16 hours [64]. In conclusion, due to the different morphology of the precipitations (type, size and distribution) which are obtained by the different aging processes, an increase to a different strength level occurs. This is the reason why natural aged 6xxx materials show lower strength, compared to artificial aged materials. Furthermore, it needs to be pointed out that when GP-II zones (β'') turn into β' and β through over-aging, it can be noted that the material's strength is decreasing [60,63]. In Figure 12 the evolution of the strength over the

conducted aging time for 6xxx alloys is presented. For various industrially used Al-Mg-Si alloys the maximum strength is reached in the transition of β'' to β' precipitations [60,65].

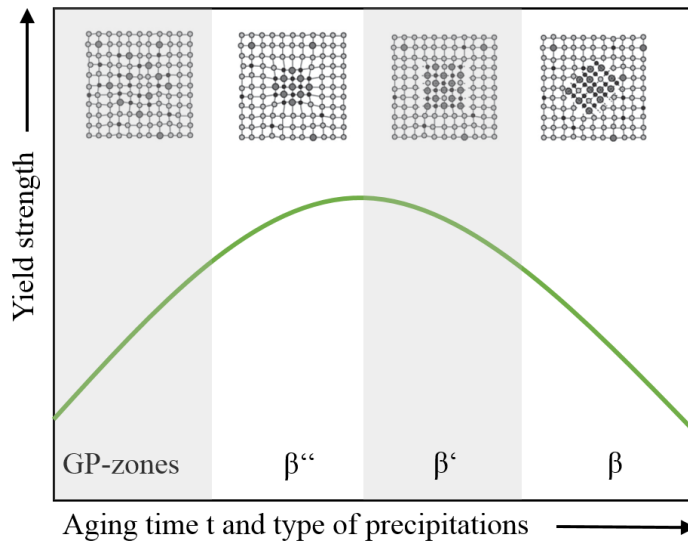


Figure 12 Principle of the precipitation sequence over time [60,63]

2.6.1 Enhanced artificial aging kinetics due to pre-heat treatment

The last step within the process chain of car body production (Table 4) is the surface treatment or rather the painting process. The conducted temperature of 185°C, in a time frame of 20 minutes, at the so-called “paint baking process”, is used for the artificial aging of the heat treatable aluminum components, with the objective of increasing their strength. It needs to be noted that the given temperature of 185°C at the paint baking process would not lead to an efficient strengthening if conventional AA6016 alloys were used [64].

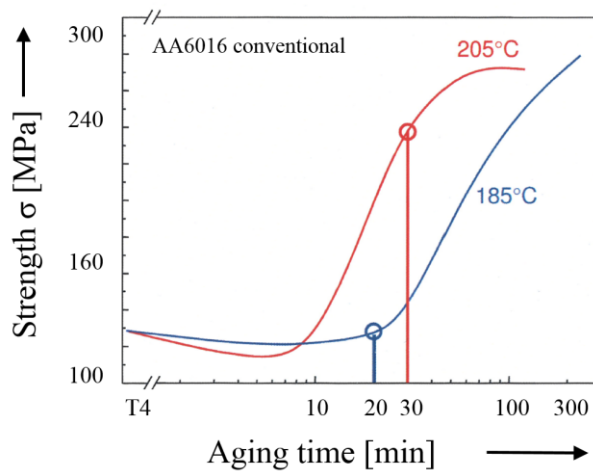


Figure 13 Artificial aging at 205°C and 185°C of AA6016 T4 in dependence of the aging time [64]

Figure 13 shows that the conducted paint baking process on a conventional aluminum alloy AA6016T4 does not subsequently result in an increase of strength when process parameters, such as a temperature of

185°C and a time period of 20 minutes, are used. To overcome this aging behaviour, a heat treatment carried out for a few minutes at temperatures of 200°C to 250°C can be applied to the material. This heat treatment leads to a partial reversal of the increased strength through natural aging and to enhanced artificial aging kinetics [66,67]. Thereby the clusters formed through natural aging are partially dissolved and it is assumed that the nucleation of the β'' phase has already started. For naturally aged alloys, such as EN AW-6016, Uchida and Mitsubishi [68,69] recommend a heat treatment of 1 to 2 minutes at a temperature of 225°C.

2.7 The influence of SHT on Al-Mg-Si alloys

Within several investigations the influence of SHT on Al-Mg-Si alloys was analysed [52,54,56,70–72]. In these studies, in particular, heat-treatable materials of the type AA6016 and AA6182 were analysed. Thereby, tensile tests were carried out to study the modification of strength and ductility due to various conducted SHT temperatures on the specimen. The SHT processes were performed through heating strategies based on conduction (heat plates) and radiation (laser technologies) (Figure 14-left). Furthermore, microscopic studies on the heat treated alloys were conducted, as well as the technique of differential scanning calorimetry (DSC) was used. Its objective was to generate a better understanding of the micro-structural evolution.

2.7.1 Time-temperature-profile of the SHT process

In general, time-temperature-profiles for the efficient procedure of SHT processes on Al-Mg-Si alloys are characterized by short heating times, short holding times and a moderate cooling rate in the air at room temperature [54,71] (Figure 14-right). However, previous studies have also conducted different SHT heating times of 93 K/s, 198 K/s and 489 K/s on tensile test specimen, which have not shown a modification on the mechanical properties of a AA6016 alloy [71]. The influence of the holding time on the mechanical properties has not been investigated so far. But when long holding times are performed, the heat treatment on complex SHT layouts becomes difficult if the cooling of the untreated zones is neglected. This is particularly relevant for the partial heating of aluminum sheets, due to the high thermal conductivity of these materials.

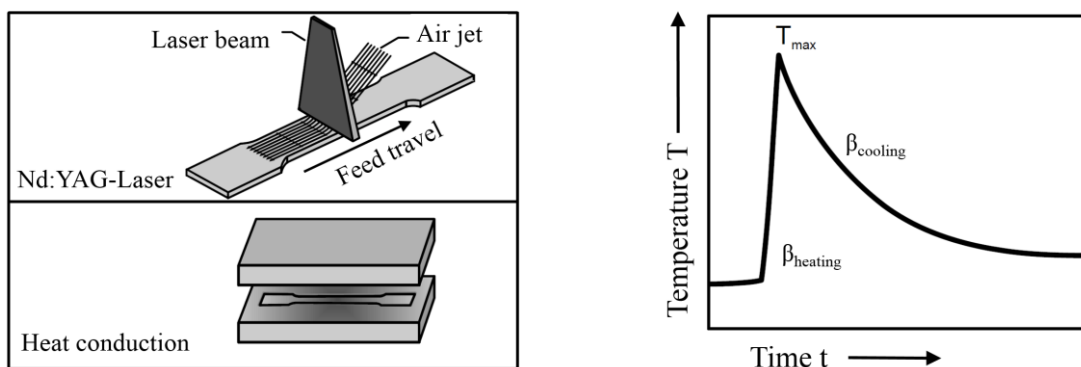


Figure 14 left: Heating principle; right: characteristic temperature time profile during SHT [71,73]

Kerausch [71] argues that the cooling rate after the SHT procedure of a conventional AA6016 aluminum alloy is affecting the softening of the material. It was discovered that fast cooling rates are shifting the beginning of the softening to higher SHT temperatures. However, in conclusion to the results of the investigations carried out so far, the crucial SHT process parameter, which primarily influences the softening of the material, is the maximum SHT temperature.

2.7.2 The influence of SHT on the conventional alloy AA6016

The influence of an SHT procedure on AA6016 and AA6181PX materials characterized by the Yield strength (YS), ultimate tensile strength (UTS), and elongation at fracture (E_F), is presented in Figure 15 [50,56,71,74]. In these investigations the strength characteristic of the conventional AA6016 alloy in dependency on the maximum conducted SHT temperature, showed the beginning of softening at a temperature of circa 200°C (T_S). The maximum softening of 50 %, compared to the initial strength, is reached at a temperature of approximately 320°C (T_E). Continuing to increase the maximum SHT temperature did not lead to further modifications of the mechanical properties of strength due to the obtained quasi-solution annealed state (W) of the material. Additionally to the modification of strength, the measurement results of the elongation at fracture (E_F) showed nearly a constant characteristic of an SHT temperature of 383°C (T_{crit}). After T_{crit} a significant decrease of E_F was measured [71]. So concluding from the results in [71], the optimal working area of the maximum SHT temperatures for the conventional AA6016 alloy was derived. Therefore, the optimal working area lies between the SHT temperature T_E , which is needed to achieve maximum softening, and the critical SHT temperature T_{crit} . In conclusion, the short term heat treatment (SHT) conducted with a maximum SHT temperature of $T_{max} > 200^\circ\text{C}$ leads to partial or total dissolution of the coherent distributed MgSi-clusters in the micro structure of Al-Mg-Si alloys [55,56,69,75].

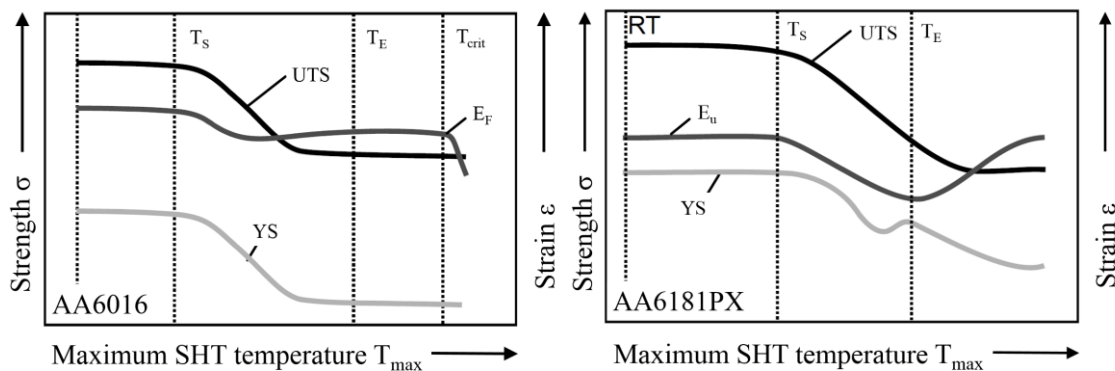


Figure 15 The influence of SHT on mechanical properties of AA6016 and AA6181 alloys [56,71,73,76]

2.7.3 The influence of SHT on the fast hardening alloy AA6181PX

The evolution of the mechanical properties for the fast hardening alloy AA6181PX through SHT is not entirely identical to the conventional aluminum alloy AA6016 (Figure 15). At an SHT temperature (T_S) of circa 200°C the softening starts and continues to an SHT temperature of 400°C [50]. The maximum reduction in yield strength (YS) of 40% and 37% of the ultimate tensile strength (UTS), compared to the initial condition, occurs at an SHT temperature of 400°C [50]. While the reduction of the UTS proceeds quasi-linear in an SHT temperature range of $200^\circ\text{C} < T < 400^\circ\text{C}$, the reduction of YS shows a temporary

renewed increase in strength at a temperature of 300°C. In previous studies, a similar strength characteristic, but with a lower magnitude of strength for conventional 6xxx alloys, was already observed [52]. Beside the decrease in strength, also a significant decrease of the uniform elongation was measured at an SHT temperature range of 250°C < T < 350°C [56]. Similar effects, but not to the same extent, were measured in previous studies on conventional hardenable aluminum alloys of the group 6xxx [52].

This phenomenon is caused by complex precipitation mechanisms, which are analysed through DSC measurements in [74]. The outcome of this study has shown that conducted SHT temperatures at a range of 250°C to 350°C lead to the dissolution of the MgSi clusters and also to the formation of sporadic concentrations of β'' and β' precipitations (Figure 16). These needle formed β'' precipitations created through SHT temperatures of 300°C, and bar formed β' precipitations, which did occur by conducted SHT temperatures of 350°C, are shown in Figure 16. The β'' and β' phase are presented as the type of semi-coherent and incoherent precipitations, which have the characteristic of increasing strength. Simultaneously the dissolution of the MgSi clusters leads to a softening of the material. This conflicting phenomenon can be observed in Figure 15 (AA6181PX) at an SHT temperature of 300°C (T_E), when the renewed increase in strength reaches its maximum value. It can be concluded that the β'' and β' precipitations have reached their maximum levels at the SHT temperature of 300°C. It should be noted that the semi-coherent and incoherent precipitations, particularly those created in the SHT temperature range of 250°C to 350°C, have an inhomogeneous microstructure consisting of Si and Mg atoms in solution, or formed as small clusters. Furthermore, the Si and Mg atoms are grouped as larger β'' and β' precipitations with a high level of lattice deformation [72]. However, this evolution of the microstructure influenced by the conducted SHT temperature leads to a decrease in ductility. The low point of the uniform elongation was found at approximately 350°C SHT temperature. By reaching the SHT temperature of 400°C the mechanical properties of ductility show the same level as the material's initial condition in the state of T4. This is explained through the complete dissolution of the MgSi clusters and an obtained microstructure, which is more homogeneous and consists of all Si and Mg atoms in solution.

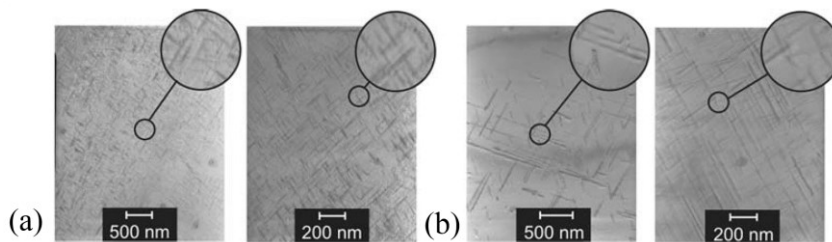


Figure 16 a: β'' precipitations ($T_{max}=300^\circ\text{C}$), b: β' precipitations ($T_{max}=350^\circ\text{C}$) for AA6181PX [74]

2.7.4 The influence of SHT on vertical anisotropy and the strain hardening exponent

The value of the vertical anisotropy is an important measure for the evaluation of sheet metal forming materials. Therefore, [71] has proven that SHT has no influence on the value of the vertical anisotropy. Contrarily to the vertical anisotropy, the strain hardening exponent is affected by the SHT. The findings of [71] show that the strain hardening exponent is increasing simultaneously with the increase of the maximum SHT temperature. The research results of [54] present a similar outcome, with regard to the strain hardening exponent. In contrast to these findings [52] has measured a decrease of the strain hardening exponent in a temperature range of 200°C to 350°C. The difference of the measured strain

hardening characteristic in [52] compared to [52,54,71] could be generated through the different heat treatment strategies by differently conducted holding times.

2.7.5 The influence of SHT on artificial aging

In [56] the influence of SHT on the artificial aging process was analysed through SHT treated tensile specimen, by the determination of YS, UTS and E_F . In this study, SHT was administered through laser heating on pre-strained (2%) specimen that have undergone an artificial aging procedure before the Al-Mg-Si alloys were tested. Usually, a process temperature of 185°C in a time frame of 20 minutes is typically used for paint baking processes in the application field of car body constructions [77]. To generate industrial-related conditions during the experiment, a combination of these two process parameters was used for the artificial aging treatment.

In Figure 17 the mechanical properties of AA6016PX and AA6181PX are illustrated in an artificially aged condition and in dependency on the maximum conducted SHT temperature [56]. The measurement results of AA6181PX show a moderate characteristic of the decrease in strength shortly after 200°C (T_s) to 300°C (T_E) SHT temperature. By reaching T_E , a sudden decrease of the YS and UTS occurs. Due to DSC measurements, [56] found out that the morphology of the precipitation of AA6181PX alloys is characterized through β'' and β' precipitations and dissolute Mg and Si atoms, when SHT temperatures in a range of 300°C to 350°C are conducted. Through these results, [56] has assumed that during the artificial aging procedure the β'' and β' precipitations are growing to larger particles which are formed into a stable Mg_sSi -phase. These larger particles have a significant smaller effect on the hardening, compared to the finely distributed β'' and β' precipitations. In [56] it was also noted that the dissolute Mg and Si atoms are grouped into smaller and coherent precipitations, with the ability of a lower distortion of the aluminum matrix. The combined impact of both effects at a maximum SHT temperature of 300°C leads to a sudden decrease in strength.

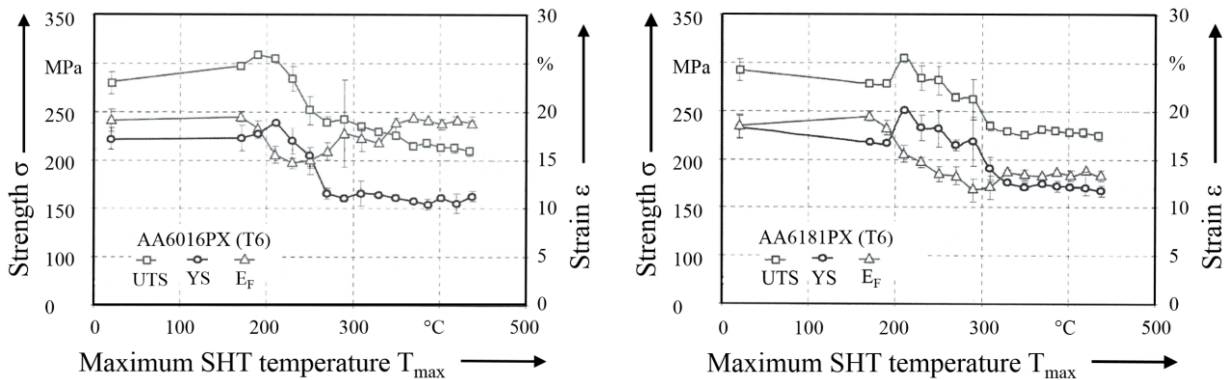


Figure 17 left: Mechanical properties of pre-strained (2%) AA6016PX; right: AA6181PX alloys in T6 condition depending on the maximum conducted SHT temperature [56]

Al-Mg-Si car body parts gain final strength after the artificial aging process, or rather, during the paint baking process. Therefore, minimum requirements do exist for strength and ductility of the car body part. For instance, within the Volkswagen-Konzern, the specification of $YS > 210$ MPa, $UTS > 250$ MPa and $E_F > 12\%$ are valid [56,77]. The measurement results of the alloy AA6181PX show that when a maximum SHT temperature of 300°C is conducted, the mechanical properties are still fulfilling the requirements of

the Volkswagen specification. The determined critical SHT temperature of 300°C by [56] cannot be generalized for all Al-Mg-Si alloys. However, it can be concluded that for Al-Mg-Si alloys the maximum SHT temperatures, which lead to β'' and β' precipitations and the simultaneously high magnitude of dissolved Mg and Si atoms, have a negative effect on the artificial aging performance. To prove this, [56] has conducted material tests of AA6016PX analogically to the test of AA6181PX.

The measurement results of the AA6016PX alloy show a sudden decrease of YS and UTS at a SHT temperature of 250°C. At this temperature range the β'' and β' precipitations are formed of AA6016PX alloys [56]. These precipitations are growing to larger particles in dependency on the SHT temperature and are formed into a stable Mg-Si phase.

The reduced amount of these larger particles shows a decreased performance in hardening when artificial aging is conducted. In addition, the alloying elements Mg and Si, which are dissolved as substitutional atoms, are grouped to smallest MgSi clusters which have a lower ability for hardening [56].

2.7.6 The influence of the storage time on artificial aging of AA6181PX

Former investigations have shown that through diffusive processes at Al-Mg-Si alloys, the dissolved MgSi clusters, caused by the SHT, are recovering over time. This means that they are formed in new cluster groups. This phenomenon leads to a renewed increase in strength [54]. Beside the renewed strengthening of the material, also the result of the artificial aging processes is affected by the renewed formations of the MgSi clusters [54,56].

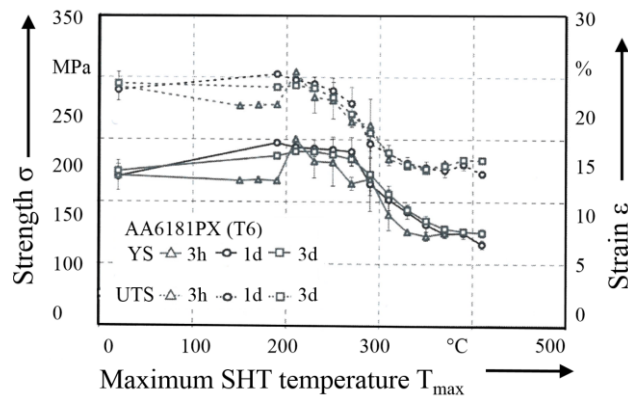


Figure 18 Mechanical properties of AA6181PX in T6 condition depending on SHT temperature and storage time between SHT and artificial aging [56]

Figure 18 shows the hardening characteristic of SHT treated specimen in T6 condition and in dependence on the storage time (T_{st}), between the SHT and the artificial aging process. Storage times of $T_{st} = 3$ hours (3h), $T_{st} = 1$ day (1d) and $T_{st} = 3$ days (3d) were used before the material was tested. The measurement series of 1d and 3d shows a similar strength characteristic and a smoother decrease in strength when SHT temperatures $> 200^\circ\text{C}$ were conducted. Contrary to these results, at the test series of 3h a sudden decrease in strength at a used SHT temperature of circa 300°C appears. It was also noted that test series of 1d and 3d show a higher level of strength compared to the test series 3h. The higher strength and the smoother strength characteristic of the test series 1d and 3d, compared to the test series 3h, is explained by the dissolved Mg and Si atoms, which are partially formed to coherent clusters or rather GPI zones due to the

natural aging. These clusters are growing faster and more homogeneous during the artificial aging process to β'' and β' precipitations, which are more effective in terms of hardening [56].

2.8 SHT integrated in the process chain of car body construction

The entire process chain of the production of car bodies includes several process stages (Table 4) [38,56]. Before the sheet metal is processed in the press plant, the coil is manufactured in the rolling mill, heat treated, and subsequently applied with dry lubricants [78]. In the press plant the coil is cut to the optimal blank outline. Before it arrives at the SHT process, the blank must be cleaned of the applied dry lubricant to avoid thermal decomposition of the lubricant through conducted SHT temperatures [56]. The SHT process should be set in a short time frame to the drawing operation in order to minimize the strengthening of the material's SHT treated zones caused by natural aging. After the drawing operation, the next step is compromised of cleaning and assembling processes of the manufactured parts. In the final manufacturing steps the assembled product undergoes a cleaning and phosphating process and finishes with the KTL process and the following paint baking process.

Table 4 Process chain – car body construction

Manufacturing facility	Process steps
1.) Rolling mill	rolling process → heat treatment → application of dry lubricant
2.) Press plant	cutting → cleaning → SHT → lubrication → drawing
3.) Car body construction	cleaning → assembling and joining
4.) Painting	Cleaning → phosphating → KTL and paint baking

2.8.1 The influence of SHT on dry lubricants

Due to the coils lubrication in the manufacturing step [78] prior to the conducted SHT process, the dry lubricants are consequently affected by the SHT treatment. The characteristic of the influenced dry lubricants through the SHT treatment was analysed by [56]. In this study the Multidraw Drylube E1 and C2 were investigated by using a strip drawing test to determine the coefficient of friction μ (COF) in dependence on the maximum SHT temperature. The SHT process was conducted by a short heating time of 3.5 s through laser heating technology. In Figure 19 the change of the COF through different conducted SHT temperatures of the Multidraw Drylube E1 is shown. It was observed that the lubrication ability at a maximum SHT temperature of 250°C starts to decrease which is justified by the considerable increase of the COF.

Due to the considerable increase of the COF in terms of tool wear and low forming properties when SHT temperatures higher than 250°C are conducted, [56] has concluded that this temperature can be seen as the process boundary for the SHT procedure on dry lubricants.

In addition to the strip drawing test, also DSC measurements on the Multidraw Drylube E1 were conducted by [56]. Through DSC measurements it was discovered that in the temperature range of 200°C and 270°C the enthalpy is decreasing. That is to say that the chemical reaction within the lubricant caused

by the SHT temperatures is exothermic. For this reason [56] has concluded that there is a coherence of the release of energy, and the cracking of the long-chain hydrocarbons of the dry lubricant, which leads to decreased lubrication properties.

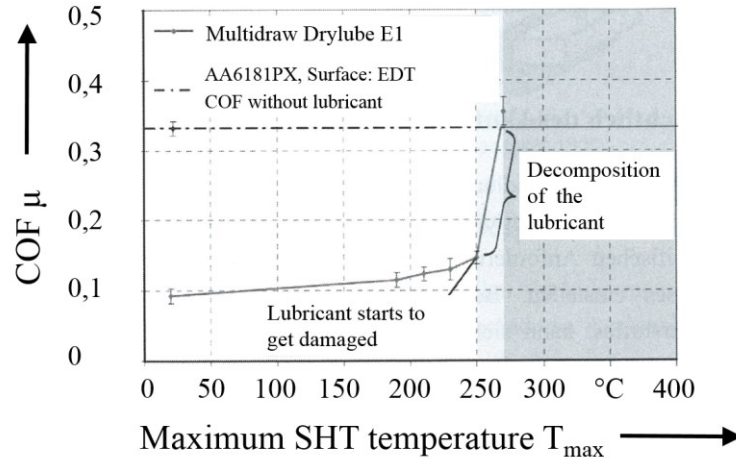


Figure 19 COF μ of the drylube E1 in dependence to the maximum SHT temperature [56]

2.9 Virtual design of sheet metal forming processes

Computer aided process design is absolutely essential in modern production technologies. This is caused by the steady increase in complexity of manufacturing processes and material systems. The use of virtual tools in the process design phase is cost and time-efficient. The aim is to determine the optimal process parameters which are needed to achieve the required part properties, such as strength and sheet thickness, before a prototype is developed and manufactured [79]. For the analyses of complex physical problems, such as sheet metal forming processes, the finite element method (FEM) was established due to the wide range of applicability in the field of process analyses [80]. Therefore, the computer aided development of the part design and their manufacturing processes has become increasingly important in the global competition. Increasing efficiency of the computer technology and numerical simulation methods is the reason for the ability to achieve shorter product development processes, increase part complexity and for it to simultaneously decrease in weight [81]. The process design of sheet metal forming processes through FEM is to be regarded as state-of-the-art. This is justified by the fact that all of today's mass produced sheet metal forming parts consistently undergo a feasibility analysis and an optimization loop through the FEM. Thus, in recent years the development time of sheet metal forming parts was reduced by 50 % due to the support of FEM simulation [82]. Furthermore, the FEM is conducted to generate the tool's acting surfaces on the basis of simulation. For many automobile manufactures it is customary to carry out a feasibility analyses through FEM within the approval process of the material which is considered for mass production [83]. General and special-purpose FEM programs, which are suitable for the modelling of sheet metal forming processes, are listed in Table 5.

In this context, it is absolutely essential that FEM can be conducted successfully for the process design of THTB. Thus, the necessary methods and techniques to fulfil the requirements in regards to the simulation of drawing operations with THTB are shown in the next sections.

Table 5 Suitable finite element software for sheet metal forming processes [84–88]

software	producer	numerical solution method	application
Abaqus	Simulia	implicit/explicit	general purpose software/non-linear
MSC Marc	MSC software corporation	implicit	general purpose software/non-linear
Pam-Stamp	ESI Group	implicit/explicit	special purpose/sheet metal forming
LsDyna	LSTC	implicit/explicit	general purpose software
AutoForm	AutoForm Engineering GmbH	implicit/explicit	special purpose/sheet metal forming

2.9.1 Mathematical definition of the flow curve

The yield strength is defined as stress which causes plastic flow of a material under a homogeneous and uniaxial stress state. Thus, the tensile test is an appropriate method to measure the flow stress as long as the stress is uniaxial and homogeneous in the specimen area of the deformation. These conditions are only valid to the point of the uniform elongation (E_u) when tensile tests are conducted. After the point of E_u , the tensile specimen begins necking and leads to a pronounced multidirectional stress state in the area of the necking zone. Hence, on the basis of the measured change in length, the flow stress can't be calculated precisely [25,89].

However, during deep drawing operations, before material failures occur, the material's deformation in dependence on the stress state can be higher than the value of the E_u obtained from tensile test. For instance, strain levels of $\phi = 0.7$ can be reached at the first forming step of deep drawing operations. Therefore, calculation procedures of sheet metal forming processes require a mathematical description of the strain hardening characteristic to higher strain levels, compared to the value of E_u obtained from the tensile test. These are also relevant for analytical calculations as well as FEM simulations of forming operations. In practice, flow curves are approximated through mathematical flow curve formulations, which show the ability of an extrapolation to higher strain levels than the values of the E_u [25]. An additional reason for the use of mathematical definitions of flow curves, is the requirement of a constant and differentiable function to describe the hardening of the material when the FEM is conducted [25].

There are various mathematical model approaches [90] which are commonly used in the field of forming technologies and particularly for the modelling of sheet metal forming processes. Apart from the approximation to strain and stress values higher than the E_u , the approaches in Table 6 pursue the goal to approximate the actual flow curve, which is required for the simulation as accurately as possible. In general, the flexibility of the model approaches is advancing by the increased number of the parameters in the mathematical function (Table 6). The parameters, which are used for the approaches of Ludwik-Hollomon, Swift, Gosh, Voce and Hockett-Sherby, just partly have a physical meaning. These parameters, which are without any physical background, are relevant for the fine adjustment of the model approach of the measured flow curve. These parameters are also named free parameter [25].

Table 6 Different extrapolation models for flow curves [91–95]

Model approach	Equation	Type of law
Ludwik-Hollomon	$k_f = A\varphi^n$	power
Swift	$k_f = A(B + \varphi)^n$	power
Gosh	$k_f = A(B + \varphi)^n - C$	power
Voce	$k_f = A - (A - B)e^{-l\varphi}$	saturated
Hockett-Sherby	$k_f = A - (A - B)e^{-l\varphi^p}$	saturated

The mathematical models for the definition of the flow curve are categorized into power and saturation laws. The approaches of Ludwik-Hollomon and Swift are similarly constructed and also classified as power functions. A typical behaviour of these mathematical models is the relatively strong hardening. The Ludwik-Hollomon equation shows a good correspondence between model and reality for the modelling of flow curves for various different materials, in particular low alloyed steel materials. However, for a wide range of materials, the degree of the correspondence between model and reality decreases by the increase in strain hardening. This problem occurs primarily at elongation regions higher than the E_u which requires the use of other mathematical functions (Table 6) [96]. Figure 20 clearly show the different hardening characteristics of the Ludwik-Hollomon and Swift function compared to the approximation approaches Gosh, Voce and Hockett-Sherby for strain values higher than the E_u [25].

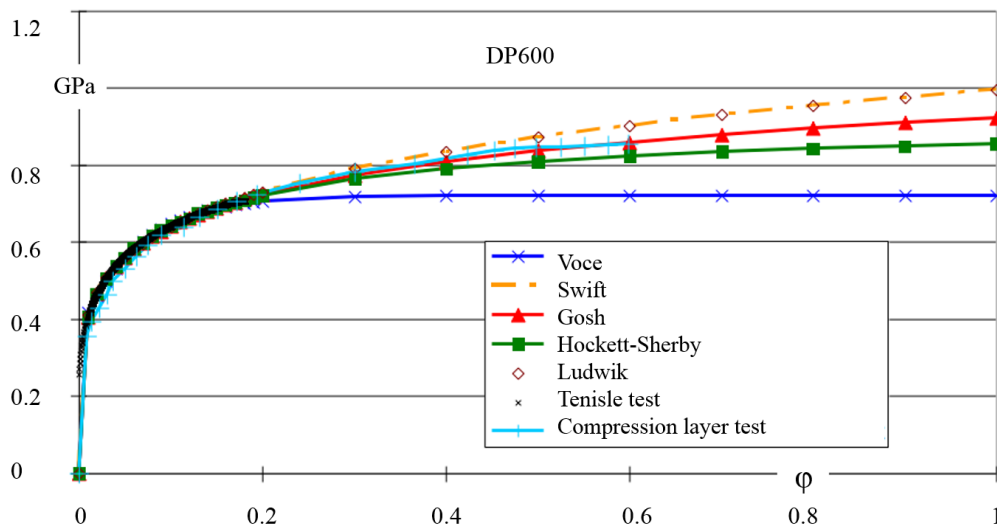


Figure 20 Yield curves – method for extrapolation – material Steel DP600 [97]

Due to the use of a wide variety of materials in the sector of sheet metal forming, the selection of an appropriate approximation law can be difficult. Consequently, the calculated strength and strain distribution of a deep drawn part may show a large deviation to the reality, if the wrong material law is used for the simulation model. For instance, the hardening characteristic of the Ludwik-Hollomon or Swift equation would not sufficiently fit the hardening behaviour accurate of high strength steel grades and aluminum alloys [25].

For the validation of the approximation approach to a corresponding material, the true stress and strain data for larger strain values than E_u can be measured by the bulge test and the compression layer test [98–100]. The characterization of different car body sheets through the bulge test have shown that a high number of materials, which are used for car body constructions, have a lower degree of hardening, compared to the hardening behaviour of the Ludwik-Hollomon and Swift equation. Therefore, the most accurate approximation of the flow curve of a AA6016 material can be achieved by the material law of Hockett-Sherby [52,101–105]. The approach of Hockett-Sherby is categorized as saturation law (Table 6). This equation consists of parameters which have a physical meaning, such as the yield strength B and the saturation flow stress A and, furthermore, the so-called free parameters I and p [25].

2.9.2 Material modelling of the multiaxial stress state

In the vast majority of sheet metal forming processes a multi axial stress state instead of a uniaxial stress state affects the material. It is not sufficient enough to describe the hardening behaviour, caused by a multiaxial stress state, only by the use of a flow curve. Therefore, the yield criterion can be applied to define the beginning of yielding depending on the stress state [25].

For industrial application of sheet metal forming simulations, the yield function proposed of Hill [106] in 1948 is still widely used [107]. This yield function is defined through 3 parameters based on the simplification of a three-dimensional problem into a two-dimensional problem. In sheet metal forming, the two-dimensional yield criterion is absolutely sufficient for the calculation of the material flow. This is justified by the occurrence of significantly larger stresses in the direction of the sheet surface, compared to the amount of stress in the direction of the sheet thickness. Thereby, in this simplified model, the acting stress in sheet thickness direction is neglected ($\sigma_3 = 0$) [25].

This approach allows the modelling of an anisotropic material behaviour through 3 parameters obtained by the uniaxial tensile test. In the model of Hill1948 (equation 3), the principle direction of the stress tensor is defined as being parallel to the rolling direction and ninety degrees to the rolling direction of the material. To be more specific, the principle direction of the stress tensor coincidents with the anisotropic axes, and the component of the shear stress σ_{12} is zero. The Hill 1948 model requires 3 mechanical parameters, the principle stress (σ_1, σ_2) and the Lankford parameters r_0 and r_{90} (equation 3) in order to define the yield stress σ_0 under plane stress conditions. Equation 3, plotted in a two-dimensional diagram, is represented as an ellipse depending on the r_0 and r_{90} coefficients. This ellipse is the so-called yield locus [105].

$$\sigma_1^2 - \frac{2r_0}{1-r_0} \sigma_1 \sigma_2 + \frac{r_0(1+r_{90})}{r_{90}(1+r_0)} \sigma_2^2 = \sigma_0^2 \quad [105] \quad \text{equation 3}$$

In case the material shows normal anisotropy which means that $r_0 = r_{90} = r$, equation 4 is reduced to

$$\sigma_1^2 - \frac{2r}{1+r} \sigma_1 \sigma_2 + \sigma_2^2 = \sigma_0^2 \quad [105] \quad \text{equation 4}$$

Under particular conditions, such as equi-biaxial tension ($\sigma_1 = \sigma_2 = \sigma_b$), the equation 4 is rewritten to equation 5 where σ_b is the equibiaxial yield stress.

$$\sigma_b = \sigma_0 \sqrt{\frac{1+r}{2}} \quad [105] \quad \text{equation 5}$$

It is crucial to point out that at equation 5, if $r < 1$, the equibiaxial yield stress is larger than the uniaxial yield stress ($\sigma_b > \sigma_0$). Contrary to this, when $r > 1$, the equibiaxial yield stress is smaller than the uniaxial yield stress ($\sigma_b < \sigma_0$) [105]. Woodthrope and Pearce [108] have observed that materials such as aluminum alloys, which have usually a r -coefficient lower than 1, are characterized due to a equi-biaxial stress which is larger than the uniaxial stress $\sigma_b > \sigma_0$. When materials show this yielding characteristic, which is also called anomalous behaviour, the Hill 1948 model would not describe the yielding in dependence on the stress state with a high correspondence to the reality. This so-called anomalous behaviour can be defined through non-quadratic yield functions. It should further be noted that there is no universal validity to describe the anisotropic material behaviour by the Lankford parameters obtained through tensile test on the quadratic yield formulation by Hill 1948 [109]. An overview of the non-quadratic yield functions and their input parameter can be found in [110].

2.10 Barlat Yld2000-2d and Hill 48 validated for AA6016T4

To improve the modelling of the equi-biaxial stress through the yield criterion, particularly for aluminum alloys, Barlat has proposed different variations of yield functions [111–113]. In 2003 Barlat and co-workers [114] have generated the most advanced yield criterion of the Barlat series, the so-called plane stress yield function Yld2000-2d. Through this model an accurate prediction of in-plane variations of yield stresses and Lankford coefficients is possible. This non-quadratic plane stress yield function is widely used and is implemented in several commercial codes.

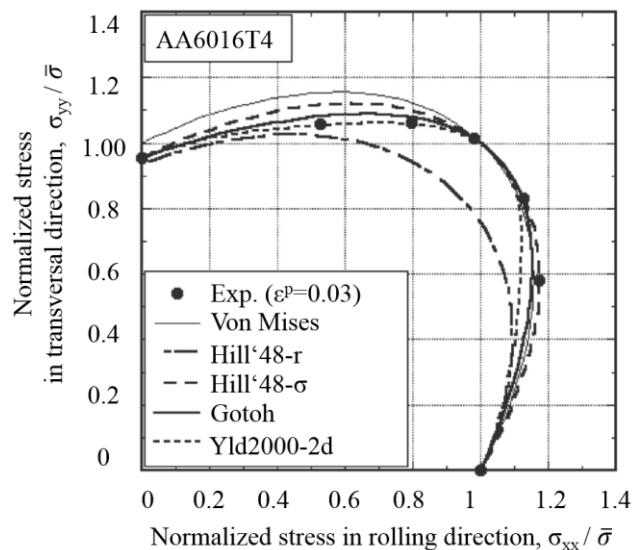


Figure 21 Comparison of normalized equi-plastic work loci with the corresponding predictions by various yield functions for AA6016T4 [115]

The non-quadratic Yld2000-2d yield function (equation 6) is based on a linear transformation of two unconditionally convex functions φ' and φ'' of deviatoric stress tensor. This model requires 8 coefficients (α_{1-8}) to define the yield surface. To determine these coefficients, 8 experimental results are needed, which can be obtained through the measured yield stress and Lankford coefficients corresponding to 0° , 45° and 90° to the rolling direction and the one equi-biaxial stress state (σ_0 , σ_{45} , σ_{90} , σ_b , r_0 , r_{45} , r_{90} , r_b). These 8 coefficients (α_{1-8}) are identified by numerical approaches, such as the Newton-Raphson method [105].

$$\sigma_0 = \left[\frac{1}{2}(\varphi' + \varphi'') \right]^{\frac{1}{m}} \quad [114] \quad \text{equation 6}$$

Figure 21 shows the evaluation of the normalized equi-plastic work locus at 3% plastic strain which is generated through different yield functions. It can be observed that the yield locus calculated through Yld2000-2d function is in a favorable agreement with the experimental results of AA6016T4, compared to the yield function of von Mises and Hill48 [115].

The non-quadratic plane stress yield function Yld2000-2d has been evaluated as an accurate and robust yield criterion, and was successfully validated for AA6016T4 alloys through experimental data by various authors [115–120].

2.10.1 Influence of the SHT on the yield surface

The influence of SHT on the yield surfaces of precipitation hardenable aluminum alloys was analyzed by Lechner [121]. In this study the aluminum alloy AA6016, in natural aged condition T4 and a sheet thickness of 1 mm, was used. For the material characterization, in order to obtain the experimental results which are required to define the yield surface, uniaxial tensile tests and biaxial tension tests were conducted. Hence, the yield surface was determined according to the model of Banabic through the yield strength and Lankford coefficient corresponding to 0°, 45° and 90° to the rolling direction and the equi-biaxial stress state. The SHT time-temperature-profile of a 1.5 s heating time, 0.3 s holding time and different SHT temperatures were achieved by the use of a Nd:YAG laser.

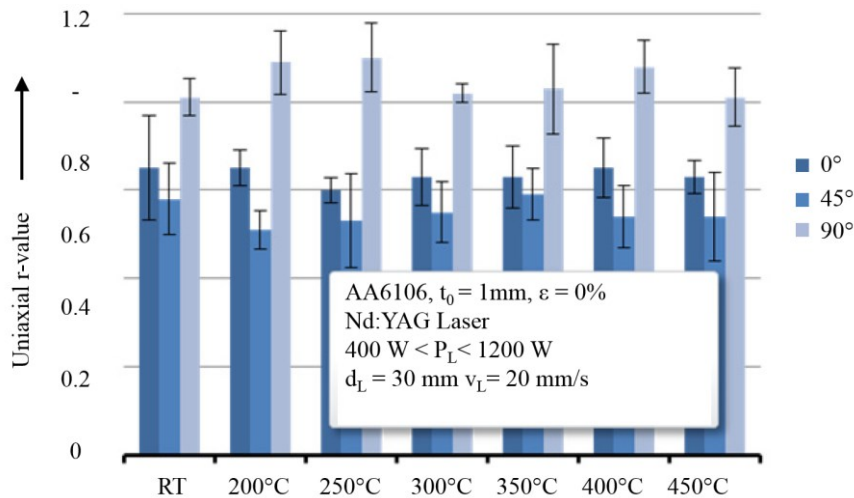


Figure 22 Influence of the SHT on the uniaxial r-value [121]

The conducted investigations in [121] show that the size of the yield surface is decreasing through the SHT procedure due to the softened material. However, the essential information for the evaluation of the yield surface is the shape of the yield locus. In this study, a marginal change of the yield surfaces shape, due to the SHT procedure, was determined (Figure 23). Lechner [121] has explained this phenomenon by the obtained r-values and the ratio of the biaxial and uniaxial yield strength. Figure 22 shows that the determined r-values are negligibly affected by the SHT. This behavior is the result of the anisotropy of a material as it is mainly characterized through the crystallographic orientation which is not influenced by the SHT. Another indicator for the shape of the yield locus is the ratio of the biaxial and uniaxial yield

strength. This study proves that this ratio exhibits minor deviations in dependence on the conducted SHT temperature. On the basis that the r -values corresponding to 0° , 45° and 90° to the rolling direction are crucial for the shape of the yield surface, such as the ratio for the biaxial and uniaxial yield strength, it can be concluded that the shape of the yield surface is not affected by the SHT. Through the obtained knowledge that the SHT has a negligible influence on the anisotropy of the material, the use of a scaled model as an alternative for the intensive material characteristic for every relevant SHT temperature is possible.

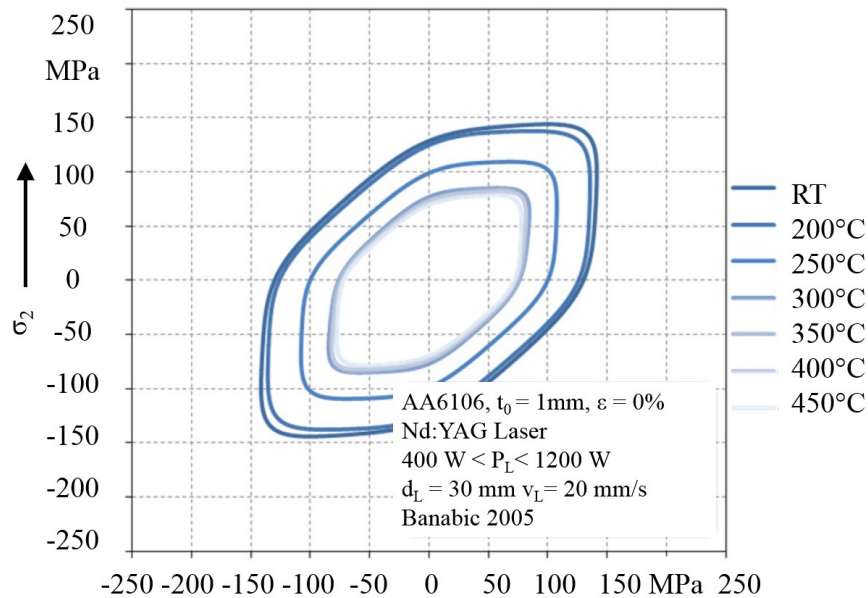


Figure 23 Influence of the SHT on the yield surface [121]

2.11 The evaluation of sheet metal forming processes and simulations by the FLD

For the evaluation of sheet metal forming processes and conducted FEM simulations the forming limit diagram (FLD) is commonly used (Figure 24). At forming processes, locally different load states and stress ratios result in different strain combination on the part's sheet plane. These strain combinations lead to necking and consequently to cracks of the sheet metal material. Such strain combinations can be detected on the formed part, or taken from the simulation result in order to plot the strain values in the FLD (Figure 24). Every particular material has a specific forming limit with regard to necking or cracking of the material, and can be defined by the so-called forming limit curve (FLC). This curve is pictured in the FLD (Figure 24) and predicts material failure if strain values larger than the FLC occur [25]. For the measurement of the part's strain distribution, the flat sheet metal material is marked through line patterns, such as circles or squares, by using various marking methods before the forming process is conducted. The forming process causes a local distortion of these marked dots relying on the stress state [33,122]. After the sheet metal is formed, images of the part are captured, which are analysed by a software to determine the exact location of the circles centre. Due to the obtained measuring points, the major and minor strain can be calculated.

$$\varphi_1 = \ln \frac{l_1}{d_0}$$

equation 7

$$\varphi_2 = \ln \frac{l_2}{d_0}$$

equation 8

The major and minor strains are described through equation 7 and 8. The strain is determined on the basis of the grid raster's initial diameter and the major and minor length of the elliptic axes (Figure 24). The larger logarithmic strain value is defined as major strain, and the smaller logarithmic strain value is named minor strain [123]. Figure 24 shows the deformed grid raster in correspondence to the deformation mode, such as deep drawing, uniaxial tension, plane strain and stretch forming.

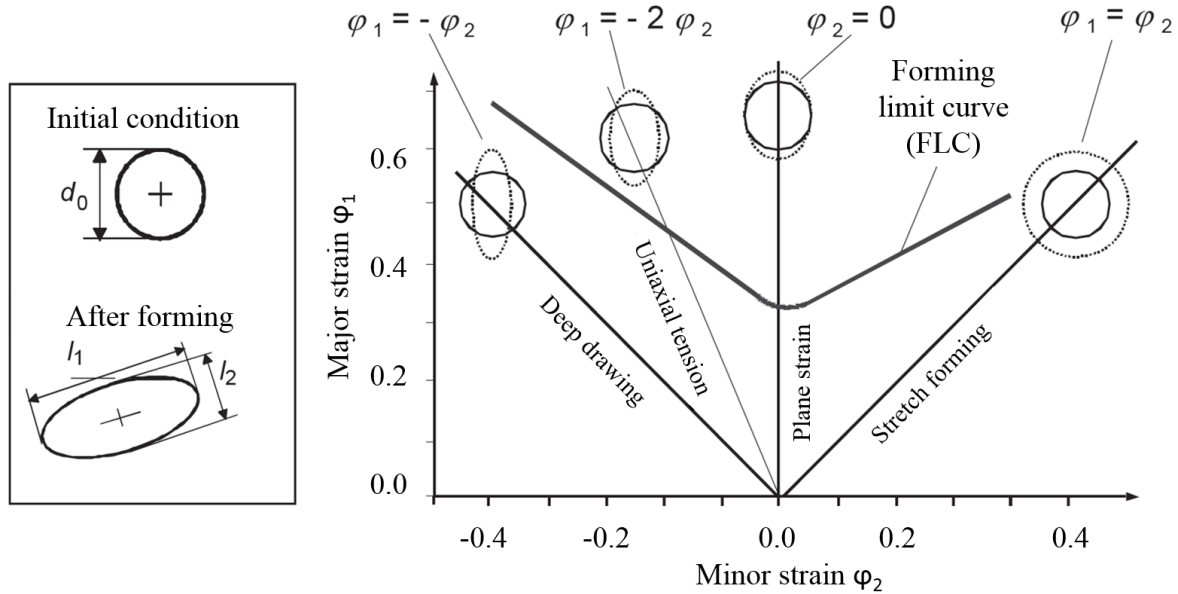


Figure 24 Schematic presentation of the forming limit diagram [29]

2.12 Influence of the SHT on the formability of a AA6016 alloy

In section 2.7.2 the influence of SHT on the uniform elongation of a AA6016 material was investigated by [56]. However, to characterize the formability of drawing operations, the forming limit of the corresponding state of stress is required. Therefore, [124] has conducted Nakajima tests on SHT treated specimen to characterize the FLC's for different SHT temperatures. In this study SHT procedures were carried out at a maximum SHT temperature of 250°C and 350°C. In Figure 25 a comparison between the SHT affected FLC's and the FLC for an untreated material is shown. Figure 25 shows the considerable decrease in formability when the SHT temperature of 350°C was used. This curve characteristic is contrary to the FLC corresponding to an SHT temperature of 250°C, which has a similar curve shape to the untreated material's FLC. Nevertheless, a slight deviation in the area of the uniaxial load state occurs. This behaviour can also be observed at the measurement results of [71], which show a slight decrease of the uniaxial uniform elongation in a SHT temperature range of 200°C to 300°C. In [71] the decreased uniaxial uniform elongation recovers at the SHT temperature range of 300°C to 400°C. This behaviour also agrees with the results of [124] on the FLC corresponding to the SHT temperature of 350°C. In conclusion, [124] found that the FLC of a AA6016 material is decreasing simultaneously by the use of SHT at temperature of 250°C and 350°C. Furthermore, the influence of SHT on the formability is depending on the state of stress.

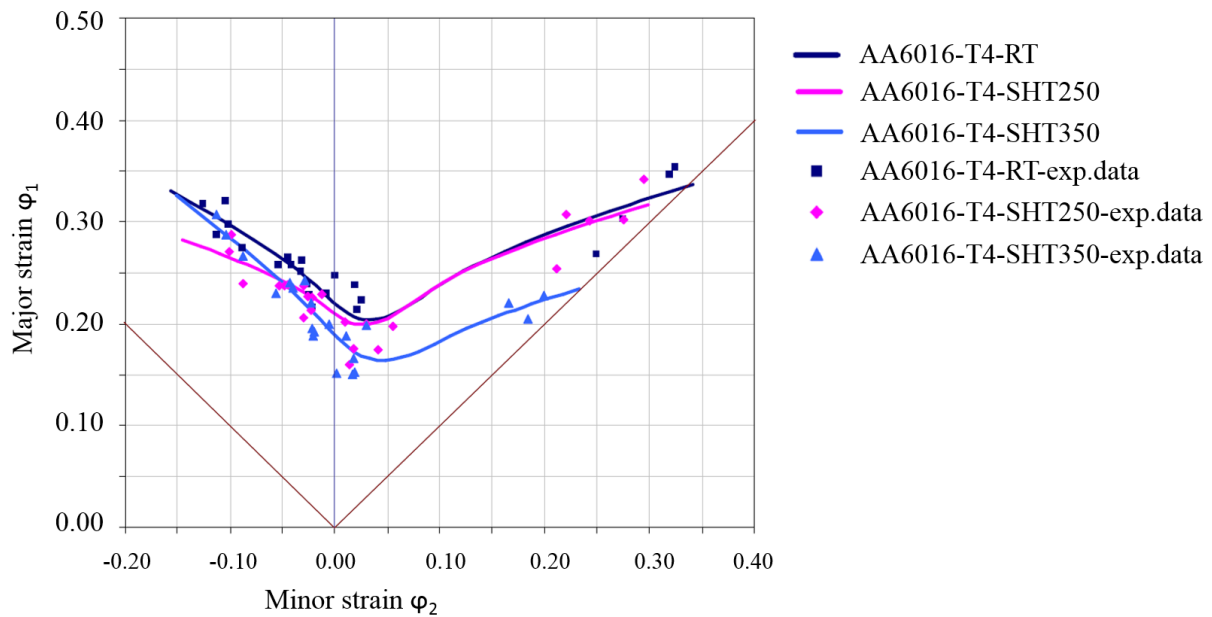


Figure 25 Forming limit curves for AA6016 influenced through the SHT [124]

2.13 FEM simulation of SHT on 6xxx alloys

THTB on AA6016 alloys for the application of a cylindrical cup geometry was described through an analytical approach by the authors [20,71] in 1998 and 2006. The analytical models were validated by comparing experimentally determined punch forces to the simulated tool forces which have shown a good correlation. However, for the design process of complex part geometries, the analytical approach is not efficient. Therefore, the use of commercial FEM simulation programs, for the analysis of the modified stress distribution by different SHT layouts, is absolutely required.

2.13.1 Mechanical approach

The disadvantage of commercial FEM programs can be the limited flexibility with regard to the process modelling of complex problems. This might force FEM software users to strong simplifications of the physical problems which are needed to be solved. In 2006 Hogg [52] simplified the process of THTB of a AA6016 alloy by neglecting the heat treatment process in the simulation model. In this model, the heat treatment, with the objective to change the mechanical properties of the material, was replaced by a blank's separation into an untreated and heat treated zone which shows differently categorized strength properties (Figure 26). It should be noted that this modelling approach does not consider the change of the mechanical properties in the heat transition zone. To prove the accuracy of this approach, Hogg [52] has validated the simulated sheet thickness to the measurement results of the drawn cylindrical cup. The conducted simulation, by the use of the FEM software OPTRIS, showed a good agreement to the experiment. The yield surface was described by Barlat 1991 yield criterion and the flow curves for the T4 state and SHT treated conditions were approximated due to the material law of Hockett-Sherby [52].

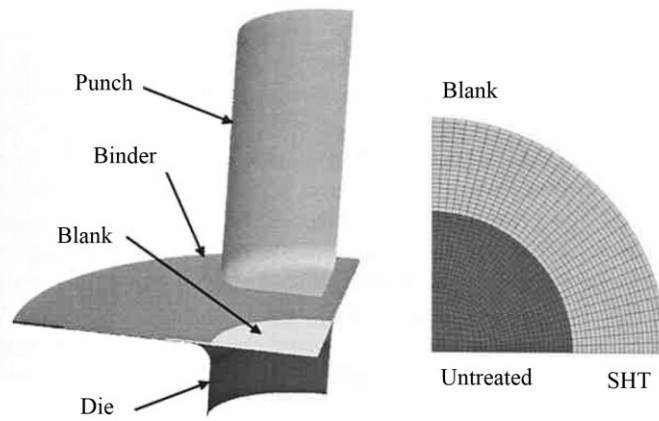


Figure 26 SHT - FEM model of cylindrical cup geometry [52]

2.13.2 Thermo-mechanically coupled approach

In 2007 Kerausch [71] accomplished to model a 3d FEM simulation of a drawing procedure which includes a laser heat treatment simulation before the actual forming simulation. This was achieved through a phenomenological material model and the coupling of the thermal and mechanical problem, by using the simulation software ABAQUS, version 6.3. The coupling was realized via an analysis step between the heat treatment and the mechanical simulation. Thereby, the maximum heat treatment temperature obtained in the heat treatment simulation (Figure 27-1) correlates with the phenomenological material model, with the purpose of adjusting the mechanical properties of the blank. This results in an inhomogeneous strength distribution on the sheet plane, if the calculated temperature is $> T_s$ (Figure 15). Furthermore, the determined strength distribution is used as input for the drawing simulation. In terms of the simulation performance, the drawing simulation showed an enhancement of the drawing properties due to the reduction of the simulated punch force and the reduction of critical stress and strain by the use of THTB.

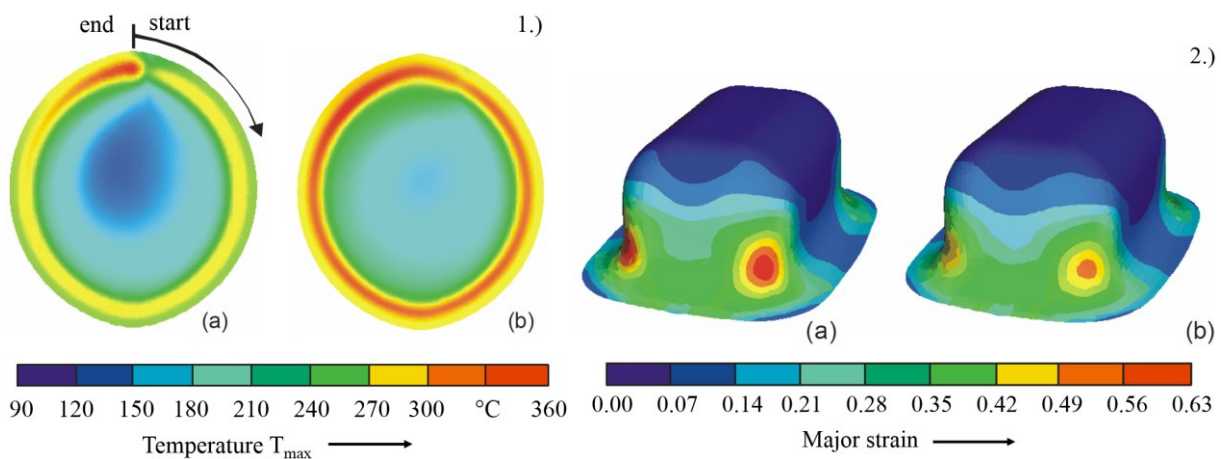


Figure 27 FEM model; left: laser heat treatment; right: forming simulation [71]

The conducted approach in [71] was used for determining the optimal laser heat treatment parameters, such as laser power and laser spot diameter, aiming to achieve a homogenous temperature distribution (Figure 27-b). Thus, a cylindrical cup geometry was successfully formed without the occurrence of material failure through the determined process parameter by simulation.

For the integration of a thermo-mechanically coupled approach in a virtual design process of forming operations, an extensive validation of the simulation model with experimental measurements might be necessary. To achieve a good agreement to forming processes in reality, the use of advanced yield criterions, in particular for the modelling of the anomalous behaviour of aluminum materials, could be crucial.

3 Objective

This thesis investigates the relevant process parameters which are crucial for an efficient and production oriented manufacturing process of tailored heat treated blanks (THTB) and subsequently the forming process and paint baking process of Al-Mg-Si alloys.

Therefore, the development and the manufacturing of heat treatment tools, which are used to generate THTB and which exhibit the ability to work under near-production conditions, is essential. The developed heating facility should provide a flexible temperature control, fast heating rates of the blank, definable holding times and temperature monitoring during the heat treatment. To analyse the crucial heat treatment parameters, a forming tool should be designed to validate the SHT performance. The relevant process parameters such as the SHT temperature, heating rate, holding time, design of the SHT layout and the storage time between SHT and forming process should be analysed. The resulting influence on the forming behaviour due to differently performed SHT process parameters has to be evaluated through the measured strain distribution of the formed test part.

In previous studies [56,71] an intensive material characterization for SHT treated alloys of AA6016T4 and AA6181PX was carried out. However, due to divergences of the alloys composition between different material batch and different material suppliers, a material characterization of the investigated alloy in this thesis is still necessary. These divergences might lead to different softening and paint baking performances. Out of the material characterization, to obtain an efficient paint baking performance as well as a good softening behaviour, the optimal SHT working temperature needs to be determined.

Additionally to the investigation of the SHT process parameters, the influence of SHT and paint baking on the mechanical properties of a drawn part should be determined. Moreover, the effect of SHT on dry lubricants and consequently the effect on the drawing performance shall be evaluated within this thesis. A short scheme of the results to be obtained by this work as well as the investigated process parameters are shown in Figure 28.

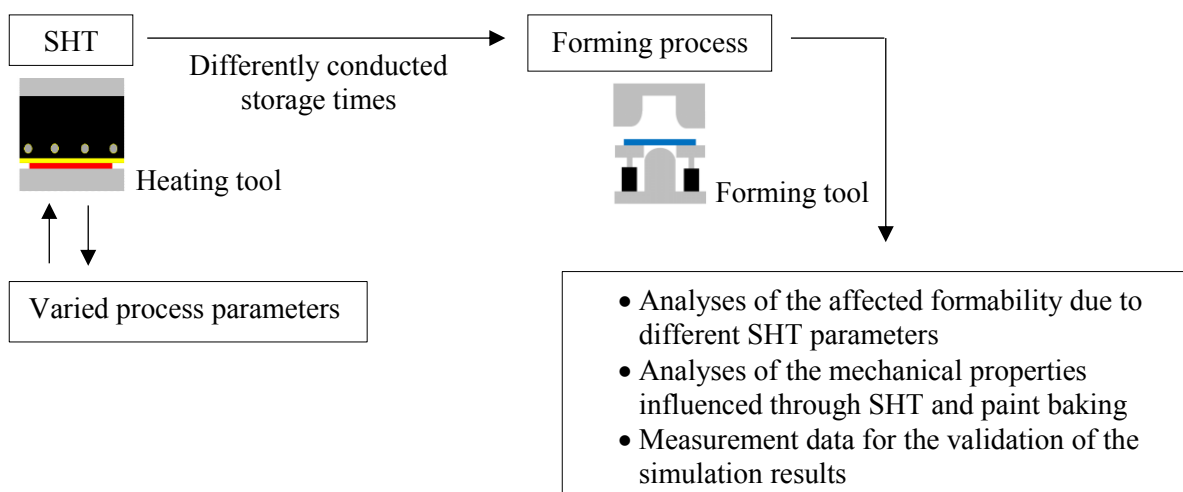


Figure 28 Objective thesis - short scheme

Objective

Another focal point of this work is the modelling of a FEM simulation to describe the SHT and forming process by the use of a commercial FEM software. This simulation model needs to be validated through experimental data (Figure 28) obtained from the heat treatment and forming process. The simulation model should be modelled after a simplified approach which describes the problem by an only mechanical description of the tailored properties. Another model approach should be used, which is based on a thermo-mechanically coupled consideration of the SHT and forming process. In this work it is intended to achieve a high correlation between the simulation results and the experiment. Therefore, the use of advanced material models for the thermo-mechanically coupled model is indispensable. Furthermore, the material parameters, which are required to describe the plastic behaviour of the material in the FEM simulation model, should be determined.

The scientific findings from this thesis should provide knowledge to support the implementation of the SHT in an industrial manufacturing process.

4 Material and conducted methods

4.1 Investigated material

Within this work the Al-Mg-Si alloy AA6016 with the trade name Superlite 220 ST was used. This alloy type belongs to the uni-alloy-concept of the aluminum producer Aleris. Furthermore, it focuses on the implementation of a standardized alloying group 6016 in considering the advantages of lower costs and environmental benefits. The use of the same alloying family for different applications facilitates the recycling process within the production and leads to sustainable benefits for the scrapping of vehicles. Therefore, the recovered scrap can be produced without the necessity of a separation process into new aluminum blanks. Only a small proportion of primary aluminum has to be added to optimize the final chemical composition [125]. The chemical composition of the used material in this research study is shown in Table 7. To be precise, this material was coated by a Fuchs PL39SX dry film lubricant through the supplier in the quantity of 1,3g/m².

Table 7 Chemical composition [%] of the used AA6016 material

Alloy type	Si	Mg	Mn	Cu	Fe	Cr	Zn	Ti
AA6016	1.12	0.45	0.14	0.07	0.28	0.02	0.01	0.02

The majority of the superlite products are used for outer panels of car bodies due to the good combination of formability, surface quality and a high value of strength after the paint baking process. Table 8 shows an overview of the Aleris uni-alloy products and their performance in strength, hemming, roping and formability. The superlite 220 ST material, which is analysed in this thesis, has, on one hand, the advantage of good properties in strength but, on the other hand, a low performance in forming.

Table 8 EN 6016 Monosheet Uni-alloy portfolio - Aleris [125]

Product	Strength	Hemming	Roping	Formability
Superlite 160 ST	+	+++	++	+++
Superlite 200 ST	++	++	++	++
Superlite 200 RF	++	++	++++	++
Superlite 200 IH	++	+++	++	++
Superlite 200 IF	++	++	++	+++
Superlite 220 ST	+++	++	++	+

Based on the car manufacturers' requirements, with regard to a high yield strength and ultimate tensile strength, the superlite 220 ST material is most suitable. Moreover, the aluminum manufacturer Aleris guarantees a yield strength in the range of 220 to 240 MPa at pre-strained conditions of 2% and after paint

baking at 185°C and 20 minutes. The guaranteed yield strength after paint baking of the superlite 220 ST material compared to the materials which show better performance in formability is shown in Figure 29. To overcome the lower properties in forming, a locally conducted SHT before forming could be crucial for deep drawing parts that possess complex geometry.

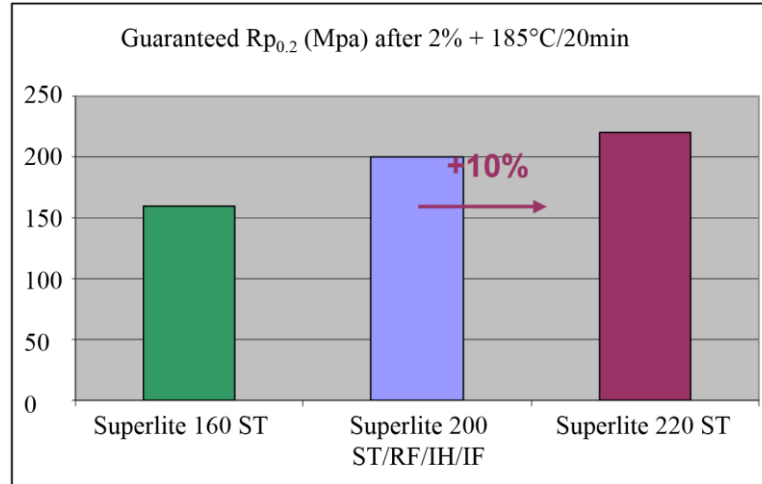


Figure 29 Guaranteed yield strength after 2% + 185°C/20min paint baking of superlite's materials [125]

4.2 Test facilities for material characterisation

4.2.1 Tensile tests

For the determination of the mechanical properties which are relevant for material modelling, the uniaxial tensile test according to DIN 1002 was conducted [126]. For these experiments a flat uniaxial tensile specimen (Figure 30, TS) according to DIN 50125 was used. In addition to formability testing, it is a common method to measure the width of the specimen during the tensile test [127]. In fact, this method is also carried out in the present study for the determination of the anisotropy coefficients (r-values) by using a width extensometer. Most of the rolled products, such as sheet metal forming materials, exhibit anisotropic behaviour due to the formed texture during the manufacturing procedure. For rolled sheets, a pronounced texture is formed in the direction of rolling which lead to different mechanical properties in rolling and transverse directions. Therefore, the tensile specimen is cut in 0°, 45° and 90° to the rolling direction.

4.2.2 In-plane tensile test

When conventional uniaxial tensile tests are conducted, the minor or width strain is negative. This test does not measure other strain combinations (state), such as the plane strain state (Figure 24) which show minor strain values of zero [128]. However, the conventional uniaxial tensile test can be adapted by the use of a notched tensile specimen (Figure 30, EU01, EU04,). The plane stress state or strain combination between uniaxial tension and plane strain (Figure 24) are generated in dependence on the shape of the notch [128].

4.2.3 Planar simple shear test

Apart from uniaxial tension and in-plane tensile tests, the shear stress can also be measured through a universal tensile testing machine by using a slotted shear specimen according to the American Society for Testing and Materials standards ASTM B831 [129]. In fact, the ASTM standard for single shear testing was in particular designed to describe the behaviour of thin aluminum products under shear load that appears in a single shear zone. This is accomplished by a simple geometry (Figure 30, SZ00) and can be conducted in a universal testing machine, where the shear stress is calculated from the uniaxial tensile force [130]. It should be noted that a fixture device is needed to reduce the rotation of the specimen by a very stiff clamping mechanism [130].

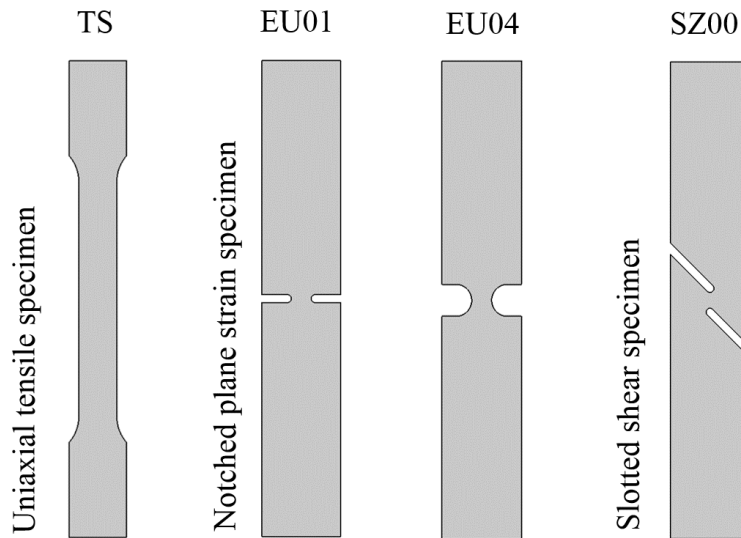


Figure 30 Conducted type of tensile specimen

4.2.4 Bulge test

In this thesis the bulge test is used to obtain flow curves to higher strain level than the E_f in particular to describe the plastic behaviour in the FEM simulation model. The standard bulge test is conducted by clamping a circular blank between die and blank holder (Figure 31-left). Characteristic of the die is a circular shape with no closed bottom. In the measurement process, the circular blank is formed into a nearly spherical shape due to an applied pressure by the use of a liquid medium. At a limited drawing depth, dependent on the material, the circular blank starts locally necking, consequently causing the formation of cracks if the process continues [25].

For the determination of stress and strain, the pressure of the liquid medium needs to be measured permanently when the bulge test is conducted. Simultaneously, a measurement system (Figure 31-left) is recording the change of the bulge shape by the radius of curvature as well as the strain situation in the section of the pole. The strain is obtained by measuring the coated stochastical patterns on the top of the blank surface. Through the dimensional modification of these patterns, and by the deformation of the material, the strain φ_1 and φ_2 can be calculated. Furthermore, by assuming that the materials volume remains constant, the sheet thickness of the corresponding liquid pressure and the radius of curvature can be calculated. The measuring point for the determination of the parameters φ_1 , φ_2 and σ_b , which are

defining the flow curve, is located in the area where the highest thinning and the maximum deformation occurs [132].

Besides, the calculation of the yield strength σ_b (equation 9) corresponding to a momentary equivalent strain φ_V (equation 10) is carried out through the Kesselformel:

$$\sigma_b = \frac{pR}{2t} \quad [25] \quad \text{equation 9}$$

where p is the hydraulic pressure, R the curvature radius at the pole and t the actual thickness of the sheet at the pole.

$$\varphi_V = \sqrt{\frac{4}{3}(\varphi_1^2 + \varphi_1\varphi_2 + \varphi_2^2)} \quad [25] \quad \text{equation 10}$$

Due to the differently generated stress state (biaxial) by the bulge test, compared to the tensile test, the material failure occurs at significantly higher strain values. Hence, flow curves to higher strain levels are determinable. Out of this it may occur that the flow curves determined by the bulge test and tensile test do not agree with each other identically (Figure 31-right). For instance, usually the flow curve of steel with lower strength, determined by the bulge test, is located above the obtained flow curve identified through the tensile test (Figure 31-right). Contrary to this, flow curves of high strength steel are usually located below when bulge tests are executed. This can be explained through differently generated stress and strain states due to the bulge test and tensile test. To be more specific, the conducted material at the tensile test is yielding, due to a uniaxial stress state, primarily, in a longitudinal direction, whereby the material measured through the bulge test is plastically deformed by a biaxial stress state, primarily, in the direction of the sheet thickness [25].

Hence, attempts are made to mathematically couple the flow curve obtained from bulge test with the flow curve determined by tensile test [25].

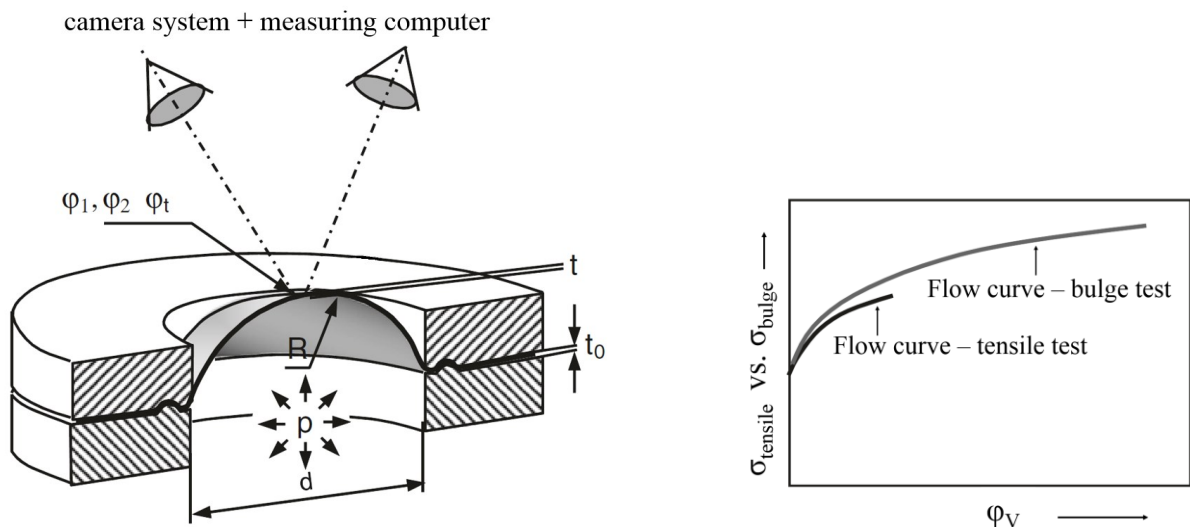


Figure 31 left: scheme of bulge test; right: flow curve obtained from bulge test and tensile test [25,132]

4.2.5 Nakajima test

For the determination of the forming limit curve (FLC) various methods, such as the Nakajima test and the Marciniak test, are used. Currently the Nakajima test, according to ISO 12004 [133], is presumably more common in practice. Due to the Nakajima test, the FLC can be obtained through a justifiable amount of effort and a good agreement to real formed parts [25].

As previously shown in section 2.11 the formability of sheet metal materials depends on the type of the stress state. Therefore, the Nakajima test uses differently shaped sheet samples to generate different states of stress, with the objective to obtain strain data which cause material failure corresponding to the state of stress. To achieve this, specimens which have a shape such as shown in Figure 32 are formed on a polished and hemispherically formed punch. In order to ensure a local necking in the middle area of the specimen, it is essential that a defined layer of lubricant is applied to the specimen. The top surface of the sheet samples is coated through stochastical patterns to measure the major and minor strain evolution, using a camera system, when the specimen is formed. Out of this, the corresponding major and minor strain value of the necking and cracking zone in the middle of the sheet sample is measured and can be illustrated in the forming limit diagram. For example, Figure 32 shows the determined major and minor strain values, which describe the forming limit of the used sheet samples for various strain combinations, generated due to different states of stress.

It should be noted that the shape and location of the FLC is influenced by the following factors:

- Sheet thickness
- Friction between blank and tool
- Strain rate and strain path
- Temperature (in particular for stainless steel and aluminum)

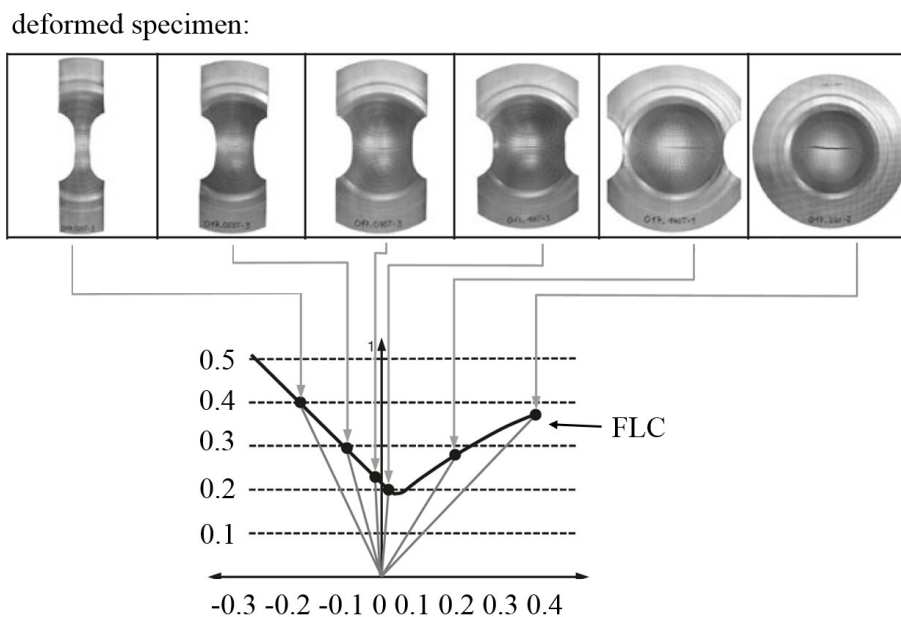


Figure 32 Determination of the FLC due to Nakajima test [25]

4.2.6 Quenching- and deformation dilatometer

In this thesis the quenching dilatometer DIL805T (Figure 33) from the producer TA instruments was used. The measuring system has the capability of using an adapter in order to carry out tensile tests on mini-flat samples (Figure 33), which, consequently, allows the measurement of the true stress and strain. In the quenching mode, the specimen is inductively heated to the required temperature and is then cooled at a user-defined cooling rate [134].

In this study, this measuring equipment was not only used to apply a controlled SHT on the specimen but also to achieve different cooling rates. Furthermore, the pre-straining, the heat treatment for the paint baking process and the final tensile tests were carried out using the quenching dilatometer.

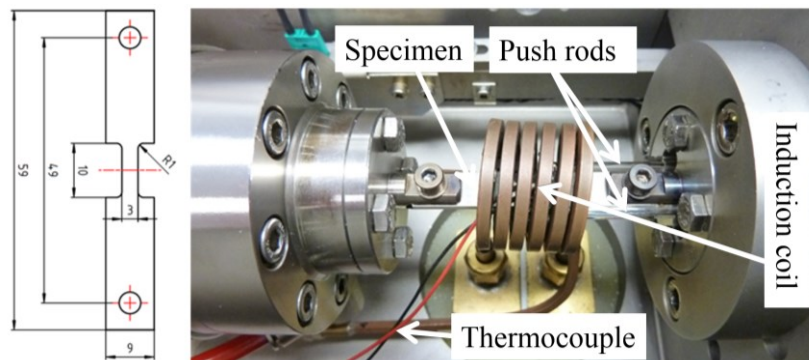


Figure 33 left: Geometry of mini-flat tensile specimen; right: Measuring device

4.3 SHT facility for tensile, bulge and Nakajima test samples

The specimens, which are tested by tensile test, bulge test and Nakajima test (section 4.2.1 to 4.2.5), are heat treated through a one-sided heating tool shown in Figure 34. This facility consists of an upper unit, which includes a steel plate equipped with a heating coil (heat plate), and an insulating plate to reduce the heat flow into the press. To be precise, the press where the heating tool is implemented executes the movement of the upper unit and provides the necessary contact pressure in order to increase the heat transfer from heat plate to specimen. Furthermore, by using this facility, the SHT is conducted in a time period of 5 s to achieve a target temperature of 270°C. The heat treated specimens are positioned on an insulation plate on the lower unit of the facility.

In brief, the obtained data from the material tests described in section 4.2.1 to 4.2.5 are mainly relevant for the simulation model which is set up in this thesis. Therefore, an exact temperature setting for the SHT target temperature should be possible. To achieve this, preliminary SHT tests using samples equipped with thermocouples, are essential for the SHT process validation. By adjusting the input temperature of the temperature control to the measured SHT temperature from the preliminary tests, the optimal temperature setting can be found.

This heating strategy was preferred over heating with laser technology, mainly because of the homogeneously achievable temperature distribution and the same heating characteristic compared to the heating facility used on the deep drawn blanks.

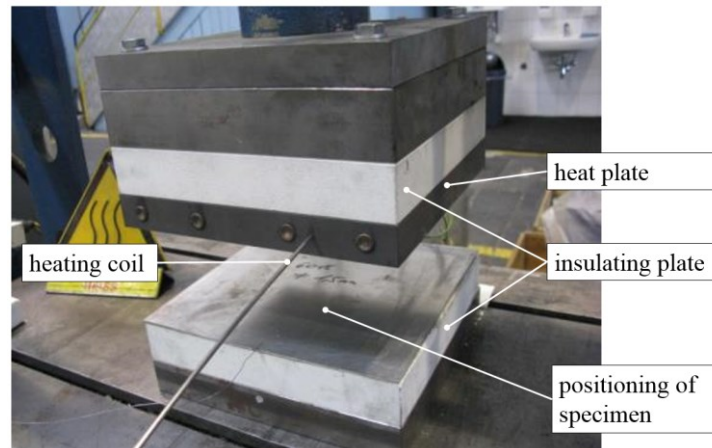


Figure 34 One-side heating tool

4.4 SHT facility for partial heat treatment of tensile specimens

A two-side contact heating tool is used for an SHT conducted in a small region of a scaled tensile specimen. In fact, the partial modified tensile specimen is deformed and evaluated by the measuring system Aramis (4.5.2). The obtained data from this material test is used to validate the simulation model, in particular in the area of the heat transition zone, which occurs between the untreated and the SHT treated area.

To achieve this, the heat treatment facility shown in Figure 35 is used. This test rig consists of two heat plates which are equipped with a heating coil. To be specific, the upper heat plate is moved by hydraulic cylinders while the scaled tensile specimen is positioned on spring loaded plates to ensure a contactless situation between specimen and heat plate, before the actual SHT is conducted. To measure the surface temperature of the specimen during the SHT, thermocouples are applied in a through hole in the heat plate and are fixed by preloaded springs. For the adjustment of the temperature input data, preliminary tests with samples equipped with thermocouples are conducted.

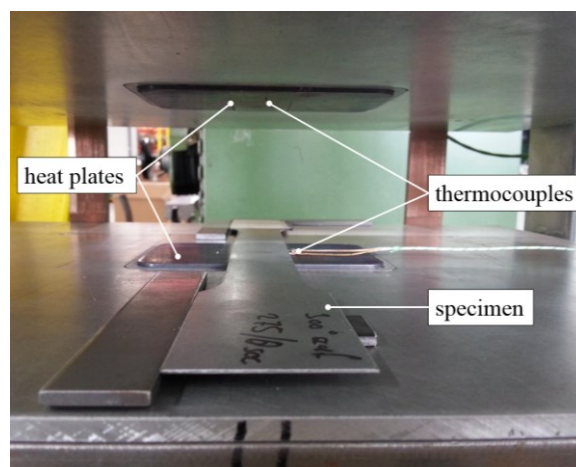


Figure 35 Two-side heating tool

4.5 Experimental methods for strain measurements

4.5.1 ARGUS

The measurement system Argus is used to measure the major and minor strain distribution as well as the sheet thickness in a specific area on the formed test geometry (Figure 36). For this, the flat blank needs to be applied by regular point patterns (Figure 36). These patterns are generated through an electrolytic method, in order to ensure for an adequate resistance to abrasion. After the forming process of the measuring object, a camera records the measuring points in several different images with various views.

Indeed, the Argus software uses photogrammetric methods for the 3D computation of the measuring points. Therefore, coded points (Figure 36) are positioned close to or on the measuring objective for the automatic spatial orientation of the individual images. Due to the photogrammetry, it is possible to calculate the 3D coordinates of the point patterns and the coded points, subsequently compiling these point rays into a 3D model. These measuring points describe the actual geometry of the formed part. By comparing the initial coordinates of the point patterns to the coordinates of the points on the formed part the major and minor strain, as well as the sheet thickness distribution, are determined.

Hence, for the evaluation of the forming results, the calculated major and minor strain values are pictured in the forming limit diagram. Furthermore, the measuring results can be validated with the FEM simulation model to show the deviation of the calculated results to the forming results in reality.

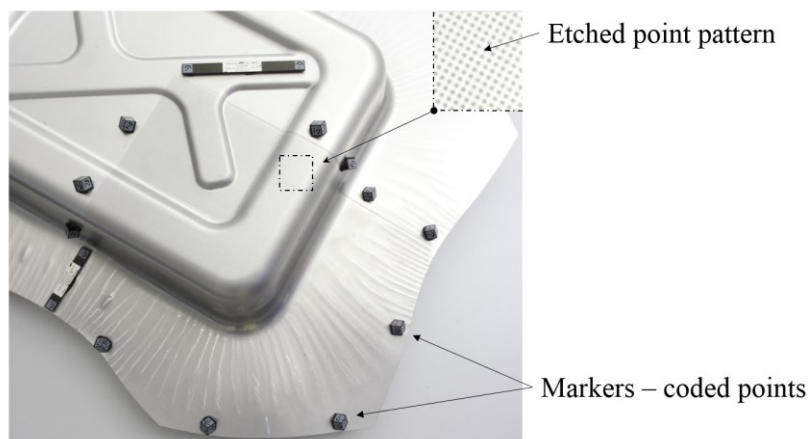


Figure 36 Prepared sample to measure major and minor strain

4.5.2 ARAMIS

Aramis is a non-contact optical 3D deformation measuring system similar to the measuring system of Argus. However, the advantage of this system compared to Argus is that the material deformation is calculated and analysed during loading. To be more specific, Aramis provides a graphical representation of the entire forming process with regard to the evolution of strain and sheet thickness.

The Aramis operates for 2D and 3D problems and uses a series of sequential digitally recorded pictures for the calculation of strain and sheet thickness. Before forming or material tests are conducted, the surface of the test sample requires markings which can be captured by the camera system. Therefore, stochastic patterns are created by spray painting colour on the top surface of the sample. The recorded pictures, which have information about the movement of the pattern, are compared and analysed by the Aramis software. Thus, strain and sheet thickness are calculated.

4.6 Determination of the heat transfer coefficient (HTC)

To model the heat treatment simulation, the heat transfer coefficient (HTC) is crucial to describing the heat flow from the heat plate into the blank. The HTC corresponding to the blank and heating plates were determined by the test rig developed by Weiß and et al [135]. This test rig consists of the following components:

- A hydraulic press to apply the contact force
- An upper and lower punch
- A muffle furnace for heating the blank
- A placement unit to position the specimen between the upper and lower punch
- A data capturing system for the recording of force, temperature and the closing-stat

Figure 37 shows the set-up of the used thermocouples incorporated in the punch and specimen. These thermocouples are needed to measure the temperature development of the punch and the specimen during the experiment, at different contact pressures. Moreover, the gathered temperature data is used for the determination of the HTC. This is achieved by a reconstruction of the conducted experiment due to a FEM simulation model built from solid elements in LsDyna, under consideration of the parametric input of the HTC. Besides, this simulation model is implemented into the optimization software LS-Opt, aiming to optimize the parametric input parameter according to the minimization of the mean square error between the measured and simulated temperature [135].

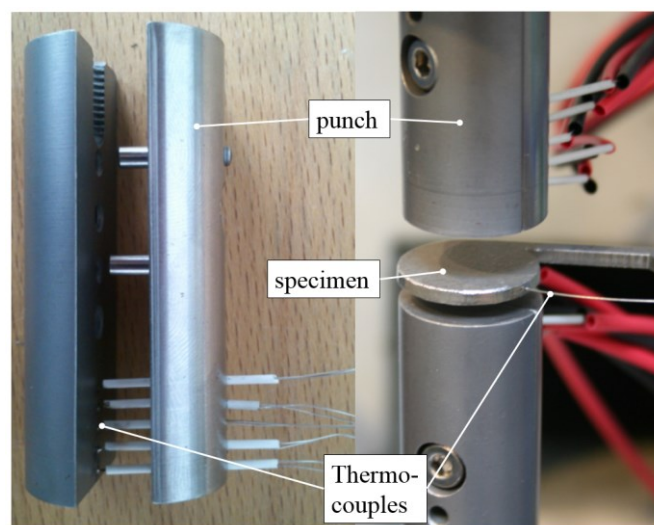


Figure 37 left: cut tool with implemented thermocouples; right: test configuration of upper and lower punch

4.7 Forming facility and part geometries

For the execution of the forming experiments a drawing geometry, adapted from spare wheel recess parts which have already been produced in industry, is used in this thesis (Figure 38). To be precise, this part is manufactured in two forming steps. The geometry out of the first forming step has a rectangular shape and is rounded through various radii (Figure 40-left). To increase the part's complexity an additional stamping structure on the bottom side is designed. The final geometry shows a bulge in the side area of the geometry and various radii in a range of 13 mm to 38 mm and a maximum drawing depth of 120 mm.

In brief, the design development of the geometry was aided by a feasibility analyses through the use of the FEM software AutoForm, in order to guarantee for crack formations without an applied SHT on the initial blank. The material data of AA6016 T4 for the conducted simulation was taken from the AutoForm material library.

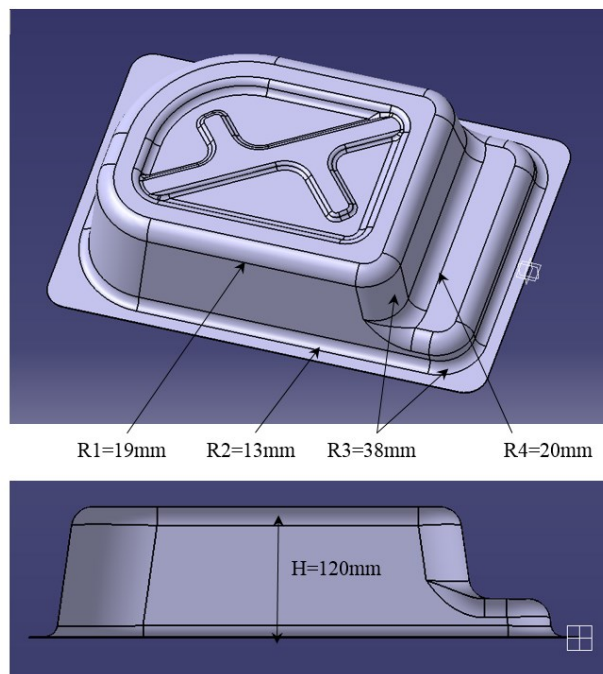


Figure 38 Deep drawing geometry

4.7.1 Deep drawing tools

Within this thesis the forming tools for the multi-step forming process are designed and manufactured. The assembly of these tools is shown in Figure 39, illustrated by a sectional view of the upper unit. First, the forming tool-1, which is used in the first forming step (Figure 39-left), has an additional function, namely to increase the maximum drawing depth. This is achieved by the capability to use an adapter plate which can be fixed on the die.

Second, the forming tool-2, which is subsequently conducted in the forming process, is equipped with a die insert which is controlled by gas pressure springs (Figure 39-right). Therefore, the stamping structure located in the bottom area, manufactured in the first process step, can be clamped by the die insert before

the actual drawing has started. This is essential when avoiding premature deformations of the stamping structure during the drawing process through occurring stresses.

The tool-1 intended for the first forming step is not only conducted to fulfil the multi-step forming operation in this thesis. It is also used to evaluate the influence of variously performed SHT parameters on the drawing performance. This is achieved by the determination of the major and minor strain distribution in the critical area of the drawn part, using the measurement system ARGUS (4.5.1). Furthermore, the formed part drawn by tool-1 is used to validate the drawing simulation, by comparing the measurement data to the simulation results, such as the sheet thickness and the major and minor strain distribution.

For analysing the influence of SHT and paint baking on the final part's properties, the test part (Figure 38, Figure 40-right) manufactured using the multi-step process is evaluated. The mechanical properties are measured by conducted tensile tests on cut out samples of the drawn part.

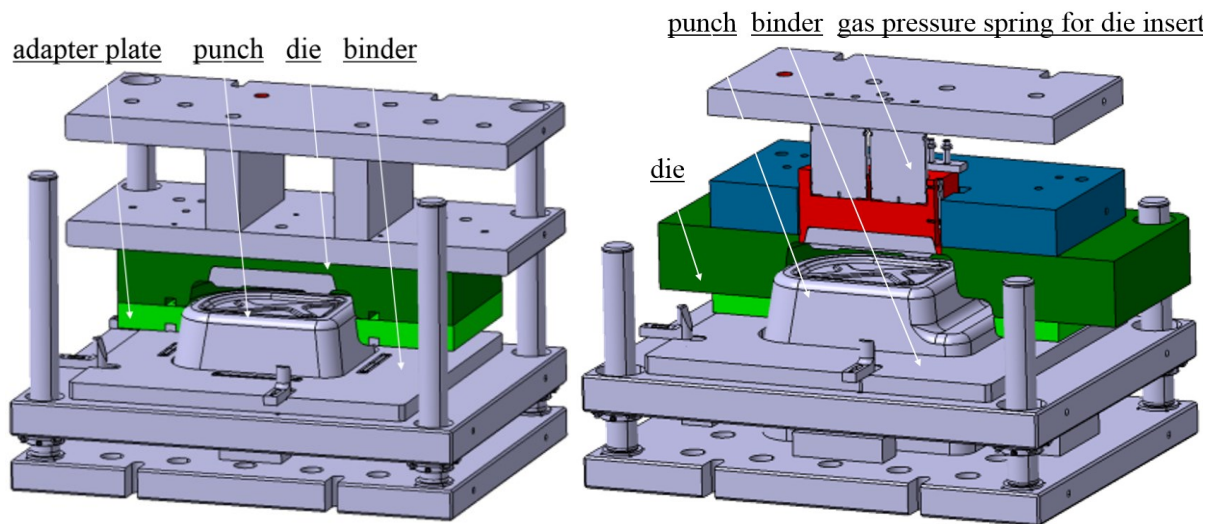


Figure 39 Forming tools: left: tool-1; right: tool-2

4.7.2 Forming behaviour of the defined geometries

For the determination of the conducted SHT layouts, a sound knowledge of the forming behaviour and the characteristic of failure are crucial. Therefore, a rough simulation was used in order to show the critical zones, by evaluating the sheet thickness distribution of the conducted part geometries (Figure 40).

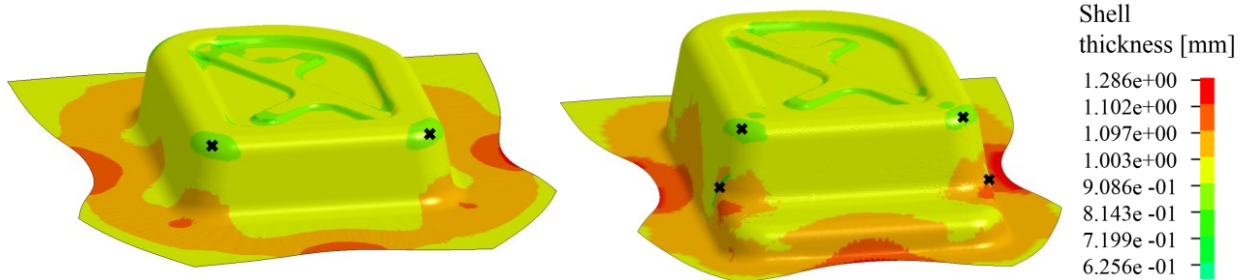


Figure 40 Pre-simulation: left: forming step 1; right forming step 2

The critical zone at geometry-1 (Figure 40-left), which shows a high possibility to failure, is located in the radius area between the bottom and wall section. This area is identified by a large thinning characteristic and the exceedance of the calculated major strain over the FLC. In addition, the critical areas are marked with a black cross in Figure 40. For the visualization of the occurring strain state in the critical areas, the strain path is plotted in Figure 41. In the case of geometry-1, the major and minor strain evolution during the forming process is constantly described through the state of the plane strain (Figure 41-left).

At geometry-2 (Figure 40-right) an additional critical area manifests in the wall section near the beginning of the bulge zone. Due to the geometry change in the second forming operation, the strain path also changes in this zone (Figure 41-right). Out of the simulation results, it can be seen that in the first forming step, shear stress occurs in the critical area of geometry-2 and continues with the state of biaxial stress in the second forming step.

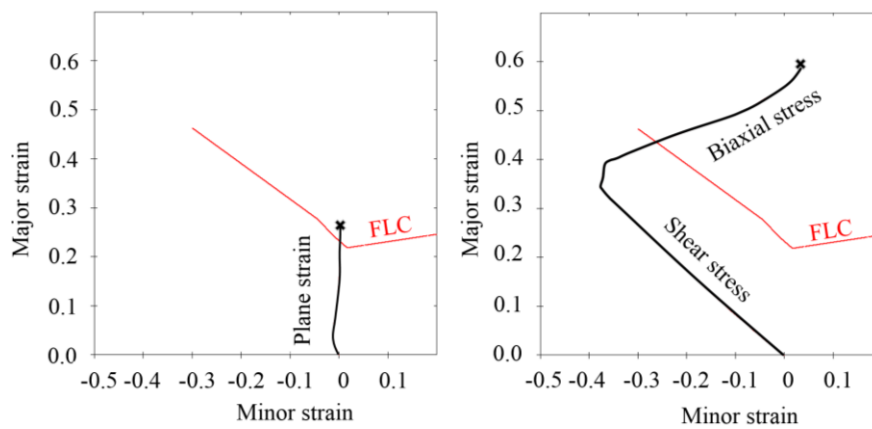


Figure 41 Strain path - critical areas: left: 2. forming step; right: 1. forming step

4.8 SHT facility for the production of THTB

4.8.1 Design of the SHT layouts

For the determination of the SHT layout corresponding to the part geometry shown in section 4.7, the first and the second active principles observed by [56] were used as guidance. Therefore, the first active principle is applied to the reduction of the critical major strain in the radius area of geometry-1 (Figure 40-left). Thus, the SHT is conducted in the area of the flange and leads to a decrease in the occurring reaction forces performing along the load path from the bottom's region to the flange's region. Consequently, the lowered reaction forces result in reduced stresses in the critical area. Furthermore, to enhance the material flow to the critical area, small SHT spots are applied near to the critical zone. This subsequently decreases the thinning behaviour and reduces stress in the critical area by sacrificing larger thinning in the region of the SHT spots. This mechanism is based on the second active principle (Figure 42-left).

During the first forming process the critical zone of geometry-2 (Figure 42-left) is also affected by the SHT layout. This is due to the reduced work of deformation (SHT in flange region) and the modified material flow by SHT spots located in the wall section (Figure 42-left). In the second forming process,

the mechanism of the lowered work of deformation due to the first active principle remains, which decreases the stress in the critical zone of geometry-2. Additionally, the flange's SHT area moves into the area of the wall, which enables an enhanced material flow in the wall zone and lowers the biaxial stress in the critical area (Figure 42-right). Moreover, the SHT spots located in the wall section serve as a sacrificing zone in order to improve the material flow to the critical area (Figure 42-right).

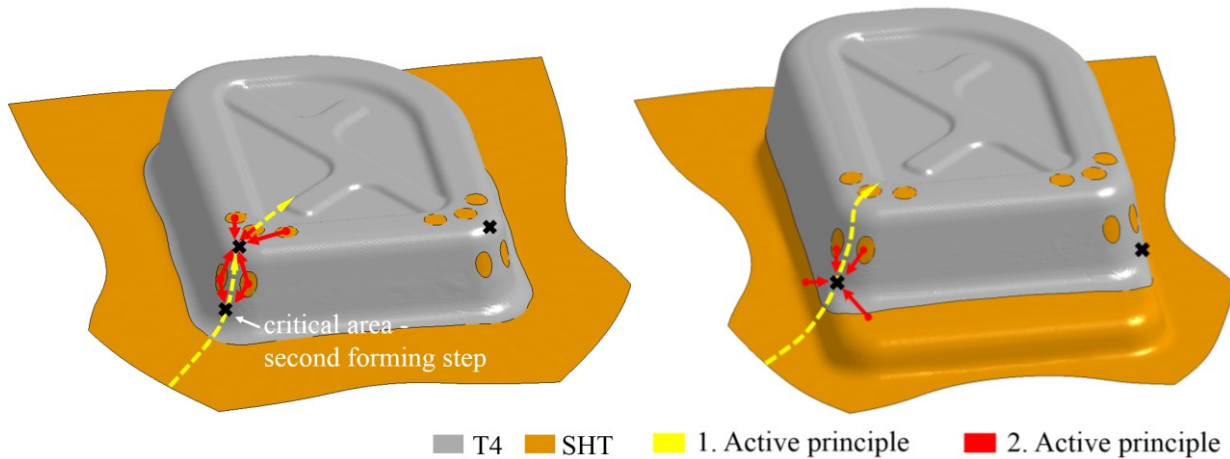


Figure 42 SHT layout and active principles of THTB; left: geometry-1; right geometry-2

4.8.2 Construction of the SHT facility

Within this thesis the SHT layout shown in section 4.8.1 is heat treated through conduction heating. The developed heating tool which was used to execute the SHT procedure on the sheet metal samples is shown in Figure 43. This heating tool is separated into an upper unit and bottom unit. That is, the upper unit is lifted by a crane and consists of several components. The component to cause the heat flow into the sheet metal is a steel plate in the shape of the flange's area, consisting of evenly distributed heating cartridges. This heat plate is fixed on a base plate. To be more specific, the base plate is guided by columns to remain centred and provides additional weight to ensure a high level of contact pressure during the heat treatment. It is noted that the HTC is pressure dependent, and consequently a high level of contact pressure is beneficial for the heat transfer. To enable a temperature regulation of the heat plate, several thermocouples are used to measure the temperature near the contact surface. In order to adjust the SHT target temperature, the thermocouples are connected with a control unit. To gather data of the blank's temperature various number of thermocouples are used. For a sufficient heat transfer, these thermocouples are guided by a through hole at the heat plate (Figure 44) and are fixed due to preloaded springs in the base plate to provide enough contact pressure between the thermocouples surface and blank. Additionally to the heat plate the upper unit also consists of 10 heating cylinders to heat up the SHT spots which are shown in Figure 44. These cylinders are also equipped with heating cartridges and controlled by the temperature control unit. To guarantee an adequate contact pressure between cylinder surface and blank, the heating cylinders are preloaded through compression springs.

The bottom unit, where the sheet metal is placed, is not applied with a heat source. Therefore, the sheet metal is positioned on an insulation multilayer textile (ThermTex 1100SVG) which is cut out in the shape of the heat-treatment layout (Figure 46-right). This insulating textile is essential for minimizing the heat loss from the heated blank to the bottom unit. Furthermore, this textile is high temperature-resistant and

possesses better insulating properties, with a coefficient of thermal conductivity of $\lambda = 0.066 \text{ W/m K}$, than solid insulating materials. The textile also compensates the non-uniform presser distribution due to the occurrence of wrinkling in the material, caused by thermal distortion during heating.

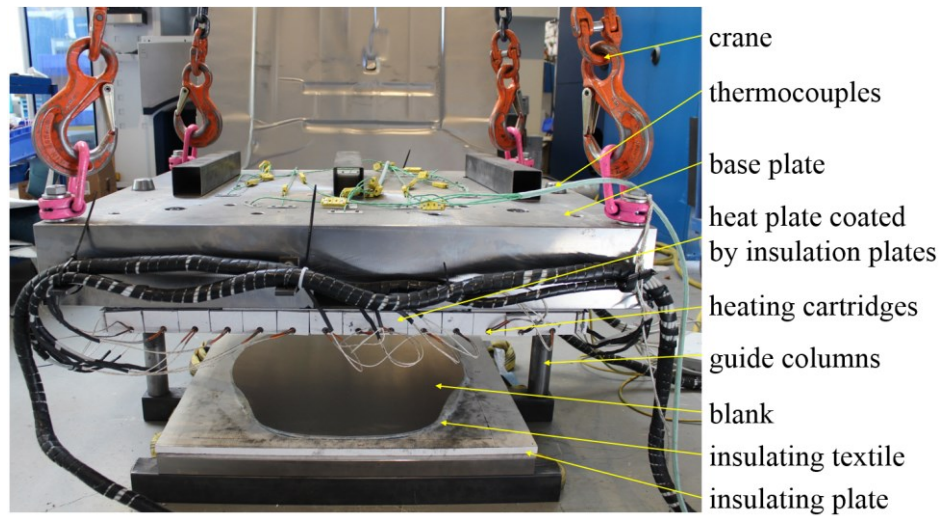


Figure 43 Test rig heating tool

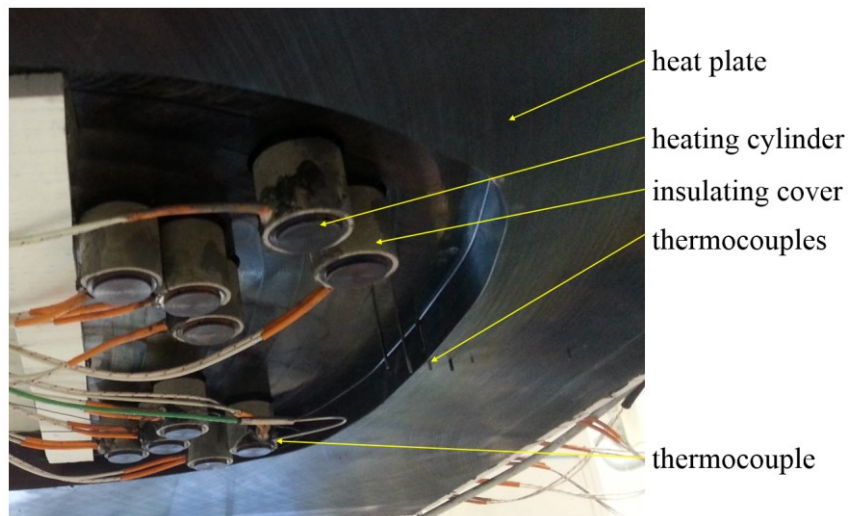


Figure 44 left: bottom side heat plate; right: Measurement set-up of preliminary SHT test

4.8.3 Evaluation of the temperature distribution

To guarantee a precise temperature setting, the conducted temperatures are monitored during the SHT. This is achieved by the thermocouples guided through the heat plate (Figure 44). In Figure 45 the position of the thermocouples measuring points on the SHT layout is shown and labelled through numbers. The SHT layout is illustrated using a temperature plot obtained from the FEM simulation (10.3). To be more specific, the surface temperature is primarily measured in the flange section of the sheet metal due to the thermocouples 1 to 6. The measuring points 7 and 8 are located outside of the SHT target area in a distance of 7.5mm and 15 mm to the SHT boundary, whereby the thermocouple numbered by 6 is placed exactly

on the SHT boundary. It should be noted that the surface temperatures in the area of the SHT spots were not validated due to the measured surface temperature. Therefore, temperature measuring inside the material, through sheet samples equipped by thermocouples (Figure 46-left and right), was executed.

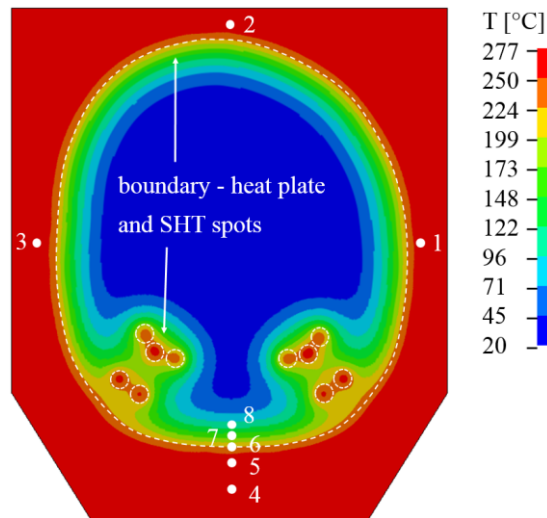


Figure 45 Thermal plot of the SHT layout and measuring points of surface temperature

Additionally to the measured surface temperatures in the section of the flange, also the temperature inside the material was measured. For these measurements the sheet samples equipped through thermocouples were positioned in different sections within the flange's heat treatment area. In Figure 46-left the measured temperature evolution, with an adjusted SHT temperature of 270°C, is shown. These results show that the measured surface temperature lies in the same temperature range as the temperatures inside the material. This is explained by the material's sheet thickness of 1 mm, which allows a very fast heat transfer through the material expedited, due to the high thermal conductivity of aluminum (section 2.5.3).

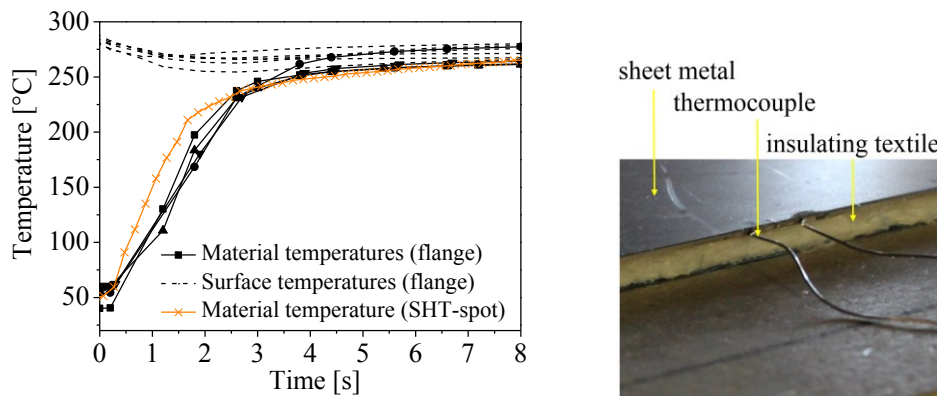


Figure 46 left: evaluation of surface temperature and temperature within the material; right: set-up of thermocouples to measure the temperature within the material

In Figure 47-left, the measured surface temperatures are plotted in a temperature range of 240 °C to 290°C. It can be observed that at the beginning of the heating process the measured temperature is elevated due to the heat plate's temperature level. When it comes to a contact between thermocouple and blank surface, the temperature decreases and shows a renewed increase after approximately 2 seconds. In this

presentation the deviation of the differently located measurement points in a temperature range of $\pm 8\text{ }^{\circ}\text{C}$ can be observed. The inhomogeneous temperature distribution is caused by the non-heated section between the heating cartridges and the non-symmetrical shape of the heat plate.

Figure 47-right shows the plotted temperature curves measured in the heat transition zone in a temperature range of 80°C to 200°C . These results show a maximum SHT temperature lower than $200\text{ }^{\circ}\text{C}$, indicating no material modification through SHT (section 2.7.2 and 2.7.3) at a distance higher than 7.5 mm to the heat plate's boundary occur.

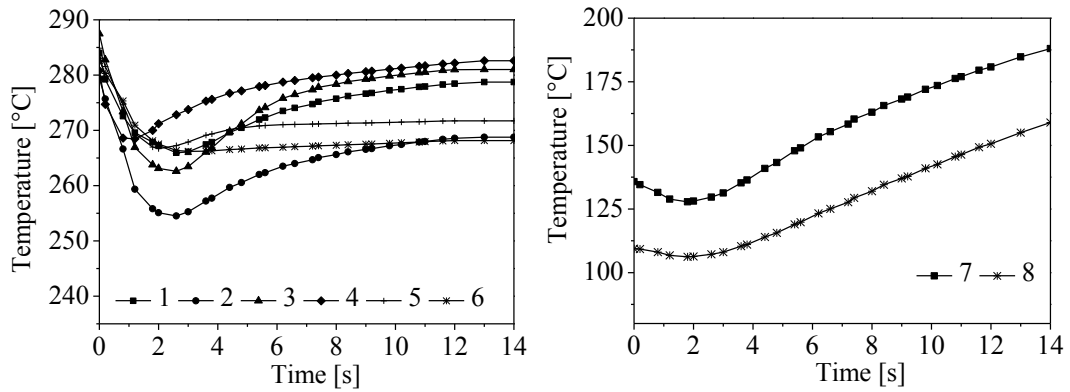


Figure 47 left: Surface temperature distribution within the SHT area; right: surface temperature outside of the SHT area

5 Material characterisation - SHT temperature and paint baking

In the following chapter results for the AA6016 (Superlite 220 ST) material's heat treatment and its characterization through the facility described in 4.2.6. are presented. The aim of the material investigation is the determination of the mechanical properties of a large range of various applied SHT temperatures. Furthermore, the influence of the paint baking process on the material, at initial and pre-strained conditions, on the corresponding SHT temperature is evaluated. This analysis is essential to finding an optimal SHT temperature to fulfil the car manufactures requirements with regard to the material strength of produced car body parts.

For the implementation of the SHT in an industrial process, the storage time plays an important role. Research findings conducted from [56], described in 2.7.6, show that the storage times in a period of 1 to 3 days only marginally influences the paint baking performance, with regard to the material strength. For further investigations, the affect of the storage time considered in a larger time frame on the AA6016 (Superlite 220 ST) material is analysed in this chapter.

5.1 Characterisation of the optimal SHT temperature

5.1.1 Process control of conducted heat treatment and material tests

An intensive material characterization was performed using differently conducted SHT temperatures in a range of 170 °C to 400 °C. In fact, this was achieved by the execution of tensile tests on mini-flat tensile specimen (Figure 33-left) which are heat treated in the quenching dilatometer. The conducted process steps and the corresponding process parameters are shown in Figure 48-left. Thereby, the SHT is performed in 5 seconds heating time and approximately 1 to 1.5 s holding time. After heating, the specimen is quenched at room temperature (slow cooling) as well as under the use of gaseous nitrogen (fast cooling rate of 20 K/s), in order to measure the influence of fast and slow cooling on the mechanical properties. After the conducted heat treatment and quenching, the mini-flat specimen is measured by tensile tests with a strain rate of 0.1 s⁻¹.

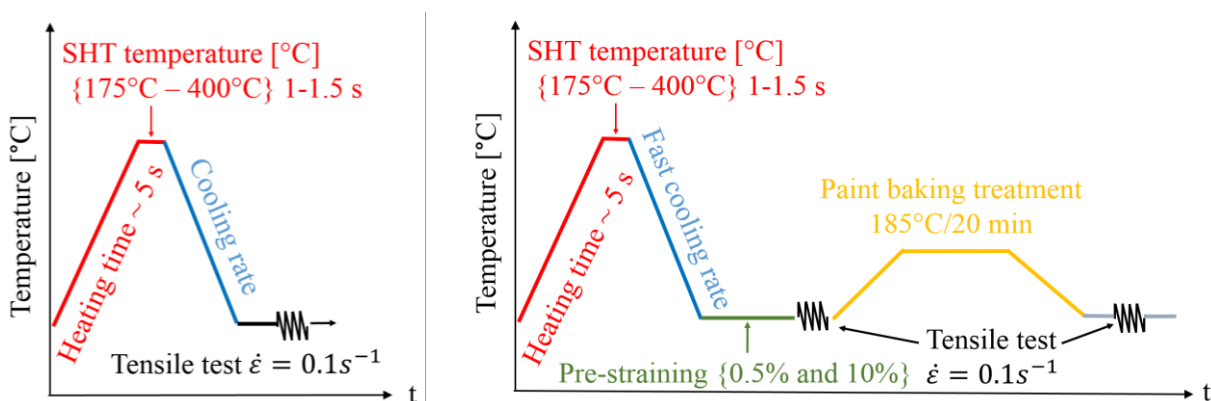


Figure 48 process control: left: only SHT; right: SHT + pre-straining + paint baking

In the second test procedure, pre-straining and the subsequent paint baking process is conducted additionally before the actual tensile test (Figure 48-right). The pre-straining is executed for strain values

of 0 %, 0.5 % and 10 %. For the artificial aging procedure, the paint baking process parameters, such as 185 °C temperature in a time frame of 20 minutes, are used.

5.1.2 Measurement results - mechanical properties

In Figure 49-left the measured yield strength (YS), ultimate tensile strength (UTS) and the elongation at fracture (E_f), in dependence on the conducted SHT temperature and for slow and fast cooling rates of the AA6016 (Superlite 220 ST), is presented. In this analysis a minor reduction of YS is observed at a SHT temperature of 175 °C. The reduction of the YS continues quasi-linearly to a SHT temperature of 300 °C. Subsequently, this behaviour is caused by a partial or complete dissolution of the coherently distributed MgSi-cluster in the microstructure [55,56,69,75]. Moreover, in the SHT temperature range of 300 °C to 370 °C a slight increase in strength is measured. This phenomenon can be explained by the simultaneously occurring effect of the dissolution of MgSi-clusters (softening) and the formation of β'' and β' precipitations (increase in strength) [56].

Beside the reduction in strength, also the reduction of the E_f is measured at an SHT temperature of 175 °C. In the SHT temperature range of 175 °C and 400 °C the E_f corresponding to the slow cooled material is increasing almost linearly, apart from two peaks, which show an abrupt decrease of the E_f . More specifically, this sudden decrease is detected at the conducted SHT temperature of 280 °C and 350 °C. An explanation for this behaviour might be given by the findings of [56]. These investigations show that a maximum amount of β'' precipitations occur for an AA6181PX material heat treated at a SHT temperature of 300 °C (Figure 16). Furthermore, β' precipitations were found in particular when SHT temperatures of 350 °C have been conducted (Figure 16). For the AA6016PX alloy the beginning of the formation of β'' precipitation is detected at SHT temperatures of 225 °C and for β' precipitation at an SHT temperature of 250 °C. This not only semi-coherent but also incoherent precipitation leads to high levels of lattice deformation and consequently to a reduction of ductility. The loss in ductility due to these precipitations, which are associated with the conducted SHT temperature, might be the indicator for the unsteady development of E_f . The renewed increase of ductility at elevated SHT temperatures is explained through the partial or complete dissolution of the MgSi-cluster, and a more homogenous microstructure, which has more Si- and Mg atoms in solution [56].

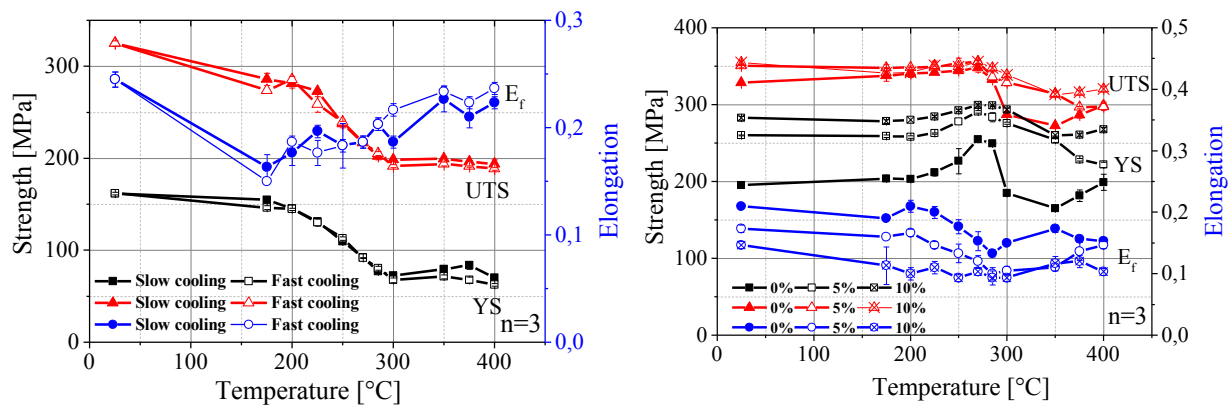


Figure 49 left: mechanical properties in dependence of the SHT temperature and cooling rate; right: mechanical properties in dependence of SHT temperature, pre-straining and paint baking

As shown above in Figure 49-left, the measurement results conducted by slow and fast cooling rates show a good correlation of the measurement data, corresponding to the YS at the SHT temperature range of < 300 °C. In the SHT temperature range of 300 °C to 400 °C a minor deviation for YS is observed. Therefore, it can be assumed that the evolution of the β'' and β' precipitation is affected by the level of the executed cooling rate, which is responsible for the renewed increase of strength in the SHT temperature range of 300 °C to 370 °C. This might also be an explanation for the deviation of the measured E_f at slow and fast cooling conditions.

Furthermore, in Figure 49-right the measured yield strength (YS), ultimate tensile strength (UTS) and the elongation at fracture (E_f) in dependence on the conducted SHT temperature, and the subsequently pre-straining and paint baking of the AA6016 (Superlite 220 ST), is presented. The measured YS of a 0 % pre-strained specimen show the maximum increase of strength through artificial aging at the corresponding SHT temperatures of 270 °C. Between the conducted SHT temperatures of 290 °C and 300 °C an abrupt decrease of strength is determined. Indeed, this behaviour might be connected to the formation of β'' precipitations in the SHT temperature range of 290 °C to 300 °C. Previous research argues that the β'' and β' precipitations, which are generated before artificial aging, grow to larger particles and precipitate into a stable Mg_5Si -phase during artificial aging. These larger particles show a significantly lower ability for strengthening, compared to a smaller and a larger number of β'' and β' precipitations [56].

The development of the pre-strained material's YS in Figure 49-right shows that the effect of artificial aging, with regard to strengthening, is less pronounced, compared to the undeformed material. The higher strengthening performance of the undeformed material could be explained by the precipitates forming homogeneously during artificial aging [136]. Furthermore, the main type of precipitations are expected to be homogeneously distributed β'' , which have the highest ability to strengthening (Figure 12). However, pre-strained materials show mainly post- β'' precipitations, which are formed heterogeneously on dislocations [136]. The pivotal factor for such conditions is the dislocation density. An increased amount of dislocations lead to an increased number of nucleation sites for precipitates. Therefore, faster dislocation-assisted diffusion leads to a faster coarsening of the precipitation phase. The effect of a coarser size, combined with a heterogeneous distribution of post- β'' precipitations, results into a less pronounced strengthening of pre-strained materials when artificial aging is conducted [136].

Contrary to the YS, the measurement data of E_f shows a decrease between SHT temperatures of 200 °C and 290 °C. In the SHT temperature range of 290 °C and 350 °C the E_f exhibit a renewed increase, which stands in opposition to the development of the YS. This behaviour indicates a modification of the precipitations in the material's microstructure due to SHT, and the subsequent paint baking process.

5.2 Investigation of the effect of natural aging on the paint baking response

5.2.1 Process control of conducted heat treatment and material tests

In this section the effect of the storage time on the mechanical properties of the AA6016 alloy for SHT and artificial aged conditions, is investigated. Moreover, the conducted process control shown in Figure 50-right is used in the following analysis. Thereby the SHT temperatures of 250 °C, 270 °C and 300 °C are executed in the first process step. These temperatures are analysed because they have differently influenced the performance of paint baking at the conducted experiments in 5.1.2 (Figure 49-right). The

same heating time as in 5.1.1, with the amount of 5 s and a holding time in a range of 1 to 1.5 s, is performed at the SHT procedure. After the SHT, the material is quenched under using gaseous nitrogen, with a cooling rate of 20 K/s. The paint baking process is conducted immediately after the SHT procedure (0w) as well as after 1 week (1w), 2 weeks (2w) and 4 weeks (4w) storage times at 185 °C and in a time frame of 20 minutes. The material characterisation is achieved by tensile test with a strain rate of 0.1 s⁻¹. Parallel to this experimental procedure, additional tests are executed on specimens, which are not artificially aged (Figure 50-left), in order to evaluate the effect of paint baking.

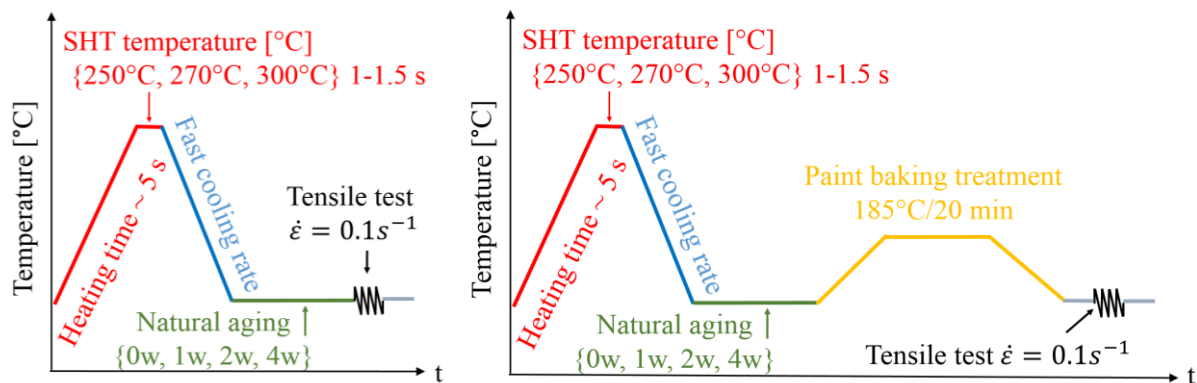


Figure 50 process control: left: SHT + natural aging; right: SHT + natural aging + pre-straining + paint baking

5.2.2 Measurement results - mechanical properties

Figure 51-left and Figure 52-left show the determined yield strength and ultimate tensile strength for the SHT treated AA6016 (Superlite 220 ST) material, with temperatures of 20 °C, 250 °C, 270°C and 300 °C, and also for different, conducted, storage times between the SHT and the material tests. These results are illustrating the material's decrease in strength caused by SHT, and the renewed increase in strength due to natural aging for all tested samples. Thereby, a linear increase of strength is observed for the SHT treated material, with a temperature of 250 °C, in a range of 4 weeks storage time. For SHT temperatures of 270 °C and 300 °C, a larger increase in strength is observed after the material is stored for one week before it is tested. This behaviour indicates the influence of the SHT temperature level on the evolution of the precipitation morphology during natural aging, and the consequently effect on the artificial aging (Figure 51-right). This investigation also demonstrates that the SHT conducted through a temperature of 250 °C leads to a slower hardening behaviour during natural aging, in a time range of 4 weeks, compared to conducted SHT temperatures of 270 °C and 300 °C.

In addition, Figure 51-right and Figure 52-right show the determined yield strength and ultimate tensile strength after SHT, different storage times and the subsequent paint baking process. In Figure 51-right, it can be observed that the best hardening performance is obtained for an SHT temperature of 270 °C, if the material is artificially aged, and shortly after the SHT procedure. Furthermore, a different trend of hardening, depending on the storage time for the conducted SHT temperatures of 250 °C, 270 °C and 300 °C, can be observed when paint baking is performed (Figure 51-right). This might be explained by the renewed formations of the MgSi clusters during natural aging, which lead to a different hardening behaviour, depending on the storage time. No hardening, or rather softening, is obtained through paint baking for the heat treated material with a SHT temperature of 300 °C (Figure 51-right).

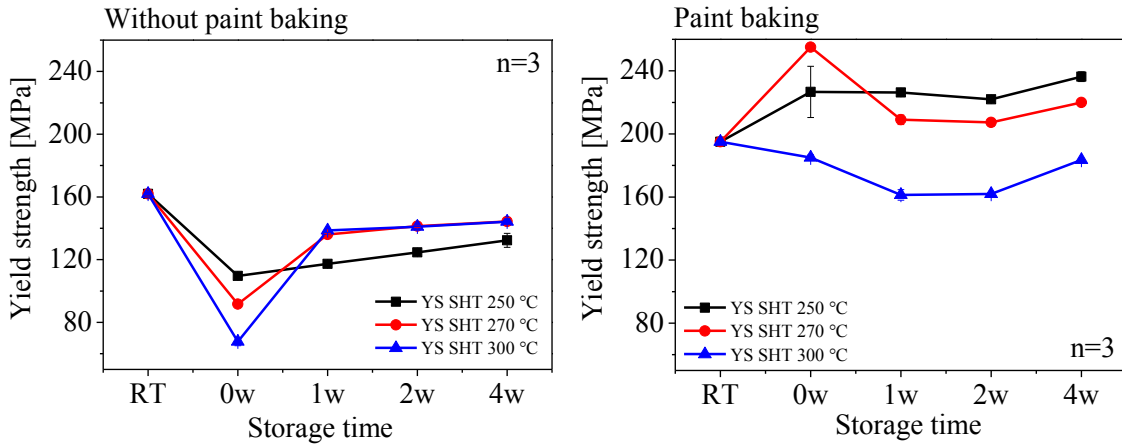


Figure 51 Yield strength depending on storage time and SHT temperature: left: no paint baking applied; right: paint baking is conducted after SHT

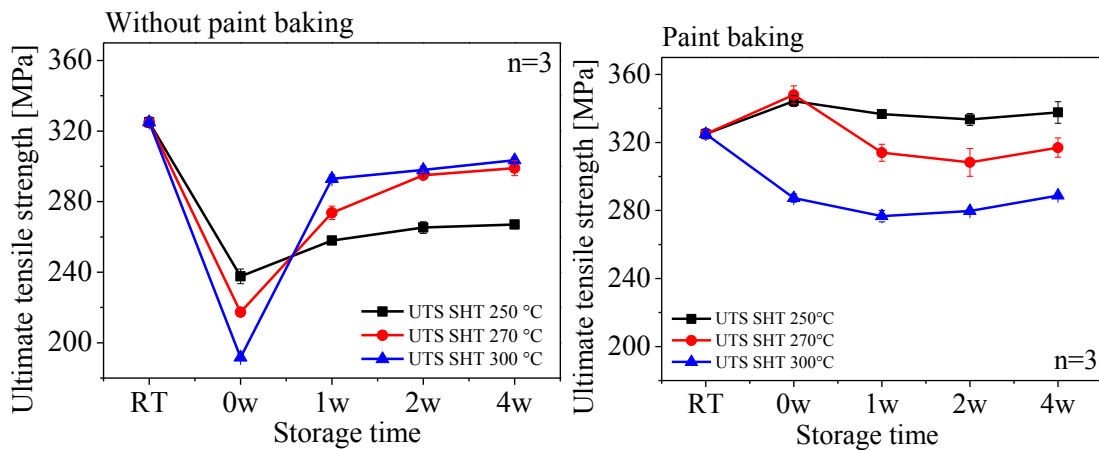


Figure 52 Ultimate strength depending on storage time and SHT temperature: left: no paint baking applied; right: paint baking is conducted after SHT

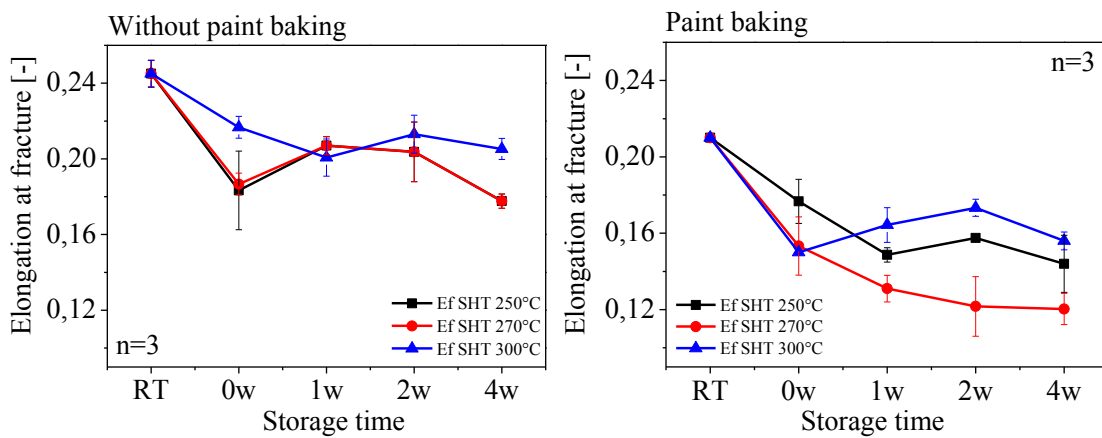


Figure 53 Elongation and fracture depending on storage time and SHT temperature: left: no paint baking applied; right: paint baking is conducted after SHT

In brief, the trend of hardening through natural aging is similar to that of the AA6016 material heat treated through SHT temperatures of 270 °C and 300 °C (Figure 51-left). Contrary to these findings, the characteristic of E_f for different natural aging conditions, exhibits a different trend at a SHT temperature of 300 °C compared to the temperature of 270 °C and 250 °C. This behaviour additionally proves that a conducted SHT temperature of 300 °C might lead to the formation of β'' precipitations, which are influencing the natural and artificial hardening behaviour of the AA6016 (Superlite 220 ST) material (Figure 53-left and right).

5.3 Summarizing evaluation of the analysed SHT process parameters

On the whole, out of the findings in 5.1.2, the optimal SHT temperature for the AA6016 (Superlite 220 ST) material aiming to achieve efficient softening, due to SHT, and to ensure for the best artificial aging performance, is determined. In the first place, the material property strength is used as an evaluation criterion in order to define the optimal SHT temperature and to meet the requirements of the car manufactures. Therefore, the SHT temperature of 270 °C leads to the best paint baking response and consequently to the highest level of the material strength. It is noted that in [56], the optimal paint baking response was determined for the alloy type AA6016PX (AC140) and AA6181PX at a conducted SHT temperature of approximately 210 °C. This substantial difference of 60 °C SHT temperature between the investigated material in this thesis and the AC140 material analysed in [56] might be explained by differences in the alloys composition, or different heat treatment procedures during the manufacturing process of the material. For the evaluation of the performance in softening, which is essential for the enhancement of formability, it is important to note that an executed SHT temperature of 270 °C does not reach the full potential. However, the mechanical material properties show a good compromise between strength and ductility, which means that 76 % of the maximum attainable reduction of strength (SHT temperature of 400 °C) can be achieved by a simultaneous loss of 24 % E_f .

Out of the findings in 5.2.2, it is observed that the storage time which occurs in the production process between the SHT procedure and the paint baking process influences the mechanical properties of the AA6016 (Superlite 220 ST) material. At a conducted SHT temperature of 270 °C the maximum strengthening and the lowest loss of the material's ductility is achieved when the paint baking process is executed shortly after the SHT. It is also observed that during natural aging the material recovers much faster in the first week of storing evaluated in a period of 1 month.

6 Material characterisation - FEM simulation

In chapter 6, results are presented for the AA6016 (Superlite 220 ST) material's heat treatment through the facility described in 4.3 and characterized through the tensile test (4.2.1), bulge test (4.2.4) and Nakajima test (4.2.5). The purpose of this material characterisation is the determination of the relevant parameters which are required for the FEM model (10.1) to describe the material's plastic behaviour and the forming limit.

Furthermore, the heat transfer coefficient between blank and heat plate (Figure 43), which is essential for an accurate heat simulation, is determined. To achieve this, the test rig described in 4.6 and the FEM optimization software LsOpt are used to determine the HTC in dependence on the contact pressure.

6.1 Mechanical parameters and flow curves

For the material modelling, especially to describe the plastic behaviour in dependence on the uniaxial stress state, flow curves corresponding to various SHT temperature are determined (Figure 54). For the SHT temperatures of 170 °C, 200 °C, 230 °C, 255 °C and 270 °C as well as for the material's T4 state, tensile tests are carried out (Figure 54). To also ensure an efficient description for the higher degree of deformation, bulge tests are performed for the AA6016 material in T4 state and at a heat treated condition for an SHT temperature of 270 °C. It is noted, that the tensile tests and bulge tests are executed shortly after the SHT.

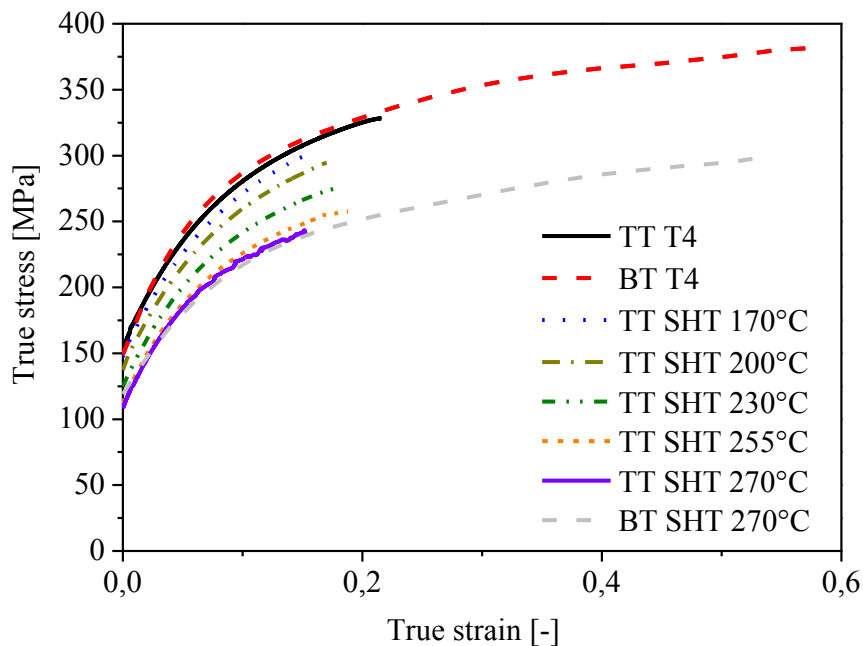


Figure 54 Measured flow curves through tensile test (TT) and bulge test (BT) – AA6016 in T4 state and for various conducted SHT temperatures

For the modelling of the material's plastic behaviour, influenced by the multi axial stress state, the material parameters shown in Table 9 are determined through tensile test. The parameters σ_0 , σ_{45} , σ_{90} are the yield

points measured through specimens which are cut out of the blank in 0°, 45° and 90° to the rolling direction. These parameters show a minor deviation in dependence on the rolling direction for the AA6016 (Superlite 220 ST) material, in particular for the T4 state (Table 9). The larger deviation of σ_0 , σ_{45} and σ_{90} for the SHT treated material can be explained by minimal thermal variances at the heat treatment. For the modelling of the anisotropic behaviour of the material, the r-values are obtained for the T4 state and SHT treated material, with a temperature of 270 °C. These parameters are also determined for the corresponding rolling direction of 0°, 45° and 90° of the investigated material (Table 9).

Table 9 Mechanical parameters – AA6016 in T4 state and for SHT (temperature of 270 °C)

Mechanical parameters	σ_0 [MPa]	σ_{45} [MPa]	σ_{90} [MPa]	r_{00}	r_{45}	r_{90}
AA6016 T4	152	150	150	0.69	0.43	0.98
AA6016 SHT 270 °C	108	113	109	0.70	0.46	0.95

6.2 Forming limit curve (FLC)

For the evaluation of the forming experiments in chapter 8 and the built FEM simulation model in 10.3.1 the FLC is determined using the Nakajima test for the material’s T4 state and SHT condition of 270 °C temperature (Figure 55). Out of these tests, it can be observed that the SHT conducted at a temperature of 270 °C leads to a reduction of the forming limit in a nearly constant manner to the corresponding load state. However, the forming limit curves determined in [124], for the SHT temperatures of 250 °C and 350 °C show a different characteristic. Especially for the state of biaxial tension and plane strain, the FLC at an SHT temperature of 270 °C has a significantly lower critical strain level than the FLC in [124] for the corresponding SHT temperature of 250 °C (Figure 25).

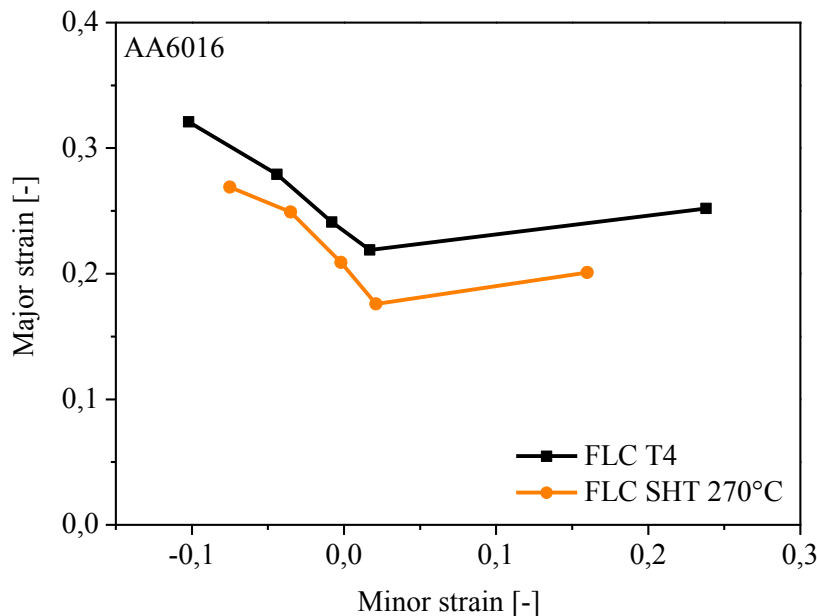


Figure 55 Forming limit curves - AA6016 in T4 state and for SHT 270 °C

6.3 Heat transfer coefficient (HTC)

Figure 56 shows the determined HTC in dependence on the contact pressure for the specific material combination (steel/aluminum) of C45U (tool) and AA6016T4 (blank). By comparing this HTC to the determined HTC in [135], regarding the material combination (steel to steel) of CR7V-L (tool) and 22MnB5 (blank), the HTC of the corresponding combination steel/aluminum shows a lower level of W/m^2k (Figure 56). It can be observed that the HTC (steel/aluminum) reaches its maximum at a conducted pressure of 10 MPa in a contact pressure range of 0 MPa to 20 MPa. Contrary to this result, the HTC (steel/steel) shows a steady increase over the contact pressure in a range of 0 MPa to 40 MPa. This characteristic might be based on the lower property of strength for aluminum materials compared to steel materials, since a softer material enables a larger deformation of the blanks asperities compared to a material which exhibit higher strength. Consequently the limit of the maximum obtainable contact surface is reached at a lower level of contact pressure.

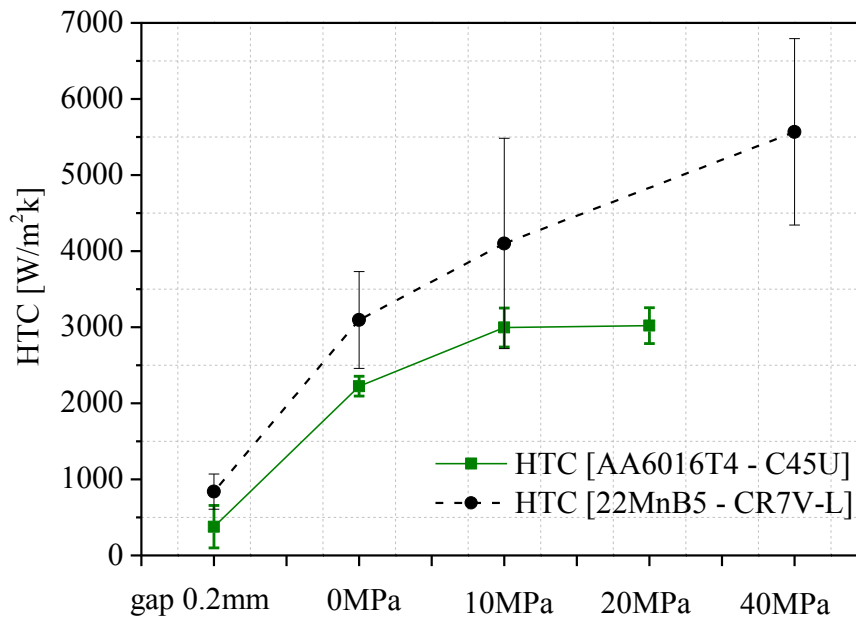


Figure 56 HTC – material combination C45U / AA6016T4 and 22MnB5 / CR7V-L [135]

7 The influence of the SHT on the dry lube and its consequences on the drawing performance

In this chapter, the influence of the SHT on the drawability of dry lube coated blanks will be analysed. The AA6016 material is applied through the dry lubricant Fuchs PL39SX (1.3 g/m²) and heat treated due to the facility described in 4.8.2. Moreover, the blank is heat treated in the area of the flange (Figure 58) and subsequently formed in a Schuler press (400 tons) according to the forming tool shown in Figure 39-left. For the evaluation of the forming performance, two different experimental procedures are used for manufacturing the test parts. These procedures are described in 7.1. The drawn test parts are validated by the sheet thickness distribution in dependence on the conducted SHT temperature in 7.2.

7.1 Process control experiment

Figure 57 shows the process scheme of the two conducted experimental procedures. In procedure A the dry lubricant from the aluminum sheets is removed before the SHT process is executed. Also, the softening of the flange area was carried out with SHT temperatures of 240 °C, 270 °C and 300 °C. After the heat treatment the blank's surface is applied through the oil-based lubricant WISURA ZU 3107/180. When the blank reaches room temperature, after the heat treatment, the forming processes are carried out. Thereby, the blank is drawn by applying a blank holder force of 200 kN. In the final step, the sheet thickness of the formed parts is measured through an ultrasonic thickness gage along a path shown in Figure 58. The path starts in the area of the flange and passes through the wall section to the part's bottom zone. The critical area, which exhibits the maximum thinning, is located in the radius zone, between bottom side and wall section.

In experimental procedure B, the dry lubricant remains on the blank's surface and undergoes the SHT process. Beside the different lubrication condition, the procedure B is conducted equally such as the experimental procedure A. Both test series are repeated 5 times to ensure reproducibility.

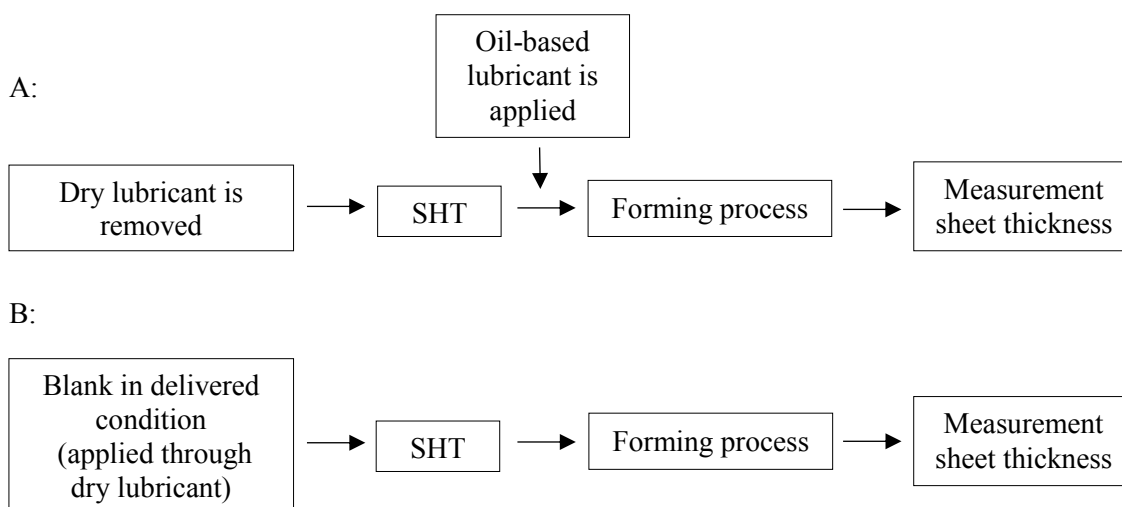


Figure 57 process scheme: A: experimental procedure 1; B: experimental procedure 2

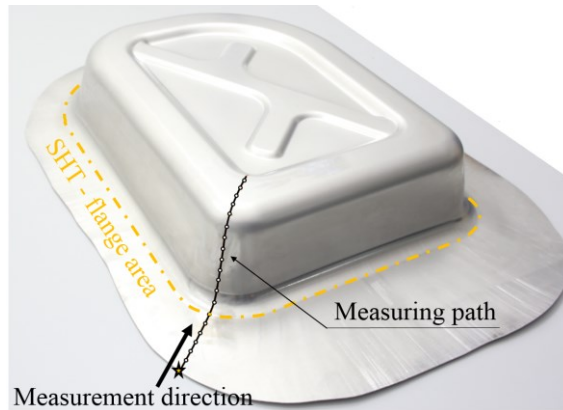


Figure 58 Test part - marked measurement path and SHT zone

7.2 Measurement results

Figure 59 shows the measurement results of the formed test parts produced through experimental procedure A. As shown, the maximum thinning in the critical radius area of the test part is observed when no SHT is performed before the forming process (T4). If SHT is conducted through a temperature of 240 °C, 270 °C or 300 °C, a reduction of thinning, in particular at the wall section (60 mm – 110 mm), the critical radius area (110 mm – 150 mm) and in the bottom zone (150 mm – 180 mm) of the drawn part can be measured. The reduction of thinning is explained by the softened material in the area of the flange and consequently a lowered work of plastic deformation. Thus, lowered stress occurs along the path marked in Figure 58 and lead to less thinning. The lowest sheet thickness reduction along the measurement path occurs when SHT with the temperature of 270 °C and 300 °C is conducted, due to the largest reduction of the yield strength (Figure 49-left). In the wall section (80 mm – 105 mm) an arbitrary increase and decrease of sheet thickness is observed because of the increase of wrinkling.

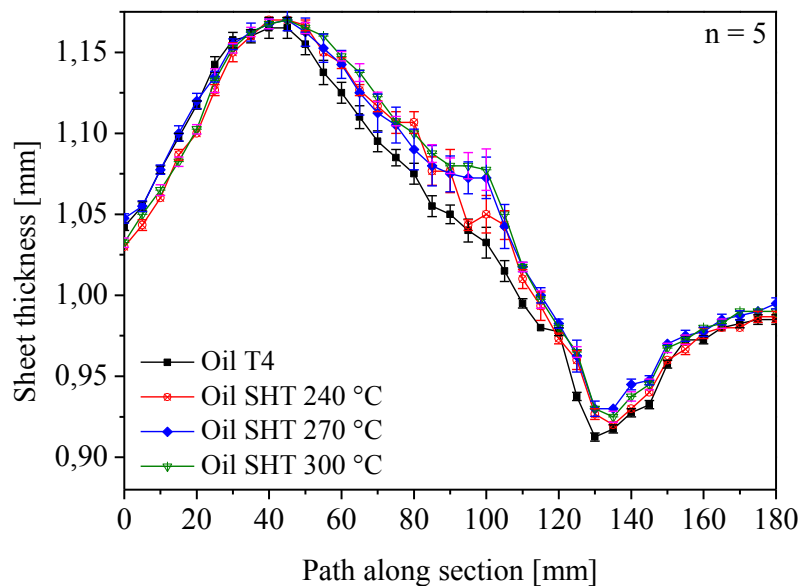


Figure 59 Sheet thickness along path at different SHT temperatures – no lubrication during SHT

Figure 60 shows the measurement results of the formed test parts produced through experimental procedure B. As it is shown, an increase of thinning by increasing the SHT temperature is measured in the flange section (0 mm – 50 mm) of the part. This behaviour indicates an increase of friction in dependence on the level of the heat-treatment temperature. This assumption is explained by the knowledge that a constant blanker holder force, and a simultaneous increase of the coefficient of friction, leads to lower thickness distribution on the forming part [57]. Also, a reduction of wrinkles is observed, which indicates an increased retention force in the area of the flange due to a higher COF. In the critical radius area, the maximum thinning is measured at heat-treatment temperatures of 270 °C and 300 °C. Essentially, an improvement of thinning in the critical radius can be achieved when an SHT temperature of 240 °C is conducted during the heat-treatment.

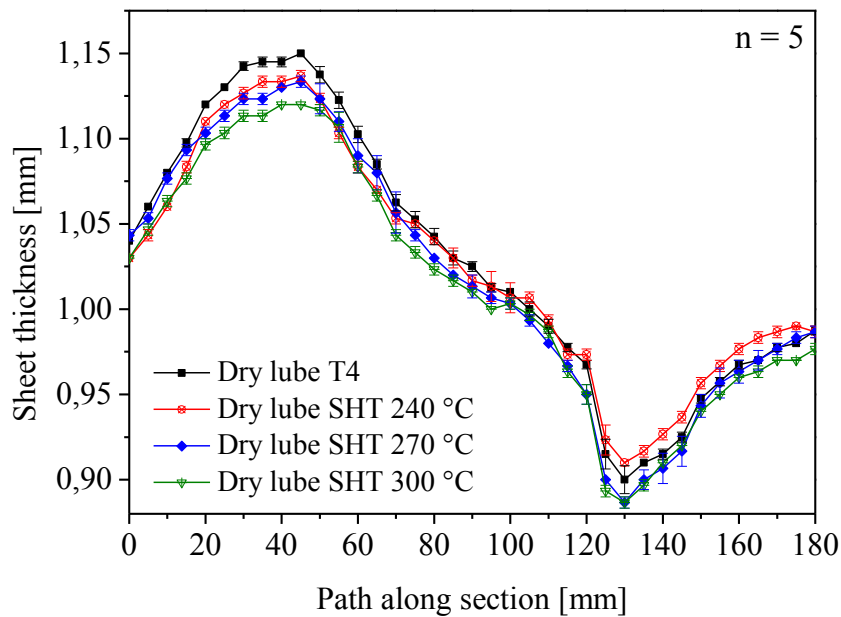


Figure 60 Sheet thickness along path at different SHT temperatures – dry lube lubrication

7.3 Conclusion

In brief, from the results in 7.2 it can be concluded that the SHT executed according to the experimental procedure A leads to an enhancement of the drawing performance. When the experimental procedure B is conducted, the SHT exhibited a negative effect on the drawability of performed SHT temperatures higher than 240 °C. This can be explained by the increase of the COF, due to the SHT, if blanks are lubricated through the dry lube Fuchs PL39SX. These findings are in correlation with the investigations in [56], which deals with the effect of SHT on the COF for a multidraw drylube E1 coated AA6xxx material. Moreover, in this research, laser technology was used for the SHT. The forming tests in the following chapters are conducted through experimental procedure A to study the effect of various SHT process parameters as well as for the validation the FEM simulation model.

8 Analyses of the influence of SHT process parameters on the drawing performance

Apart from the conducted material tests in chapter 5 and 6, the influence of various applied SHT process parameters and storage times on the drawing performance is validated and its outcome is presented in the following chapter. The objective of this investigation is to gather knowledge on the SHT process and to determine the process boundary under industrial-related conditions. Thereby, the influence of the storage time on the formability, in a time frame of 1 week, is investigated. To achieve fast cycle times during production, fast heating times are crucial. Therefore, SHT heating times in a range of 1.5 s to 14 s are analysed. Furthermore, different SHT layouts are conducted and analysed in their drawing performance. Also, for evaluating the potential of the determined optimal SHT temperature (270 °C in chapter 5), different SHT temperatures are conducted and analysed. To achieve this, the heating facility shown in 4.8.2 is used for the SHT procedure. Subsequently, the heat treated blank is formed through the drawing tool described in 4.7.1 (Figure 39-left). For the analysis on the effect of different SHT parameters on the formability, the major and minor strain distribution is measured through the measurement system Argus (4.5.1). This measurement data is plotted in the forming limit diagram in order to evaluate its effect on the forming performance of the formed parts. The detailed experimental procedure is explained in 8.1.

8.1 Experimental procedure SHT and forming

Figure 61 (below) shows the process sequence and the conducted SHT process parameters for analysing their influence on the formability of the AA6016 material. In the course of this experimental procedure, the SHT temperature of 225 °C, 270 °C and 360 °C are executed during the heat treatment. Also, the temperature profile for each temperature configuration is shown in Figure 64. For all further SHT process settings the optimal SHT temperature of 270 °C is used. In regards to the test series which evaluates different SHT layouts, these investigated SHT layouts are shown in Figure 62 through a thermal FEM simulation of the SHT process which is set up in (10.3).

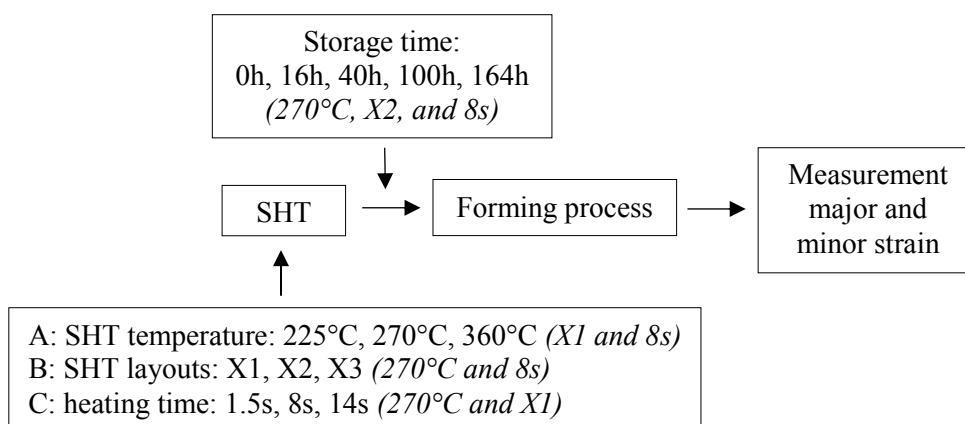


Figure 61 Process sequence SHT and forming

Analyses of the influence of SHT process parameters on the drawing performance

For a demonstrative and visual representation of the conducted SHT layouts the calculated temperatures, which are shown in Figure 62, are mapped on the formed geometry, determined through FEM simulation (Figure 63). In this presentation, only the temperature levels which cause modifications of the material, due to SHT, are visible (180°C to 270 °C). Thereby, it can be observed that SHT layout X1 changes the mechanical properties only in the flange section. This layout is conducted for analysing the relevant heating times and the different SHT temperature levels on their influence on the material's drawability. The SHT layout X2 has its areas which are affected by SHT in the flange section and the SHT spots, near to the critical zone. Additionally, also a pronounced heat transition zone between flange section and SHT spots located in the wall zone influences the material properties due to SHT. Layout X2 is executed for investigating the influence of the conducted storage time on the formability of the AA6016 material.

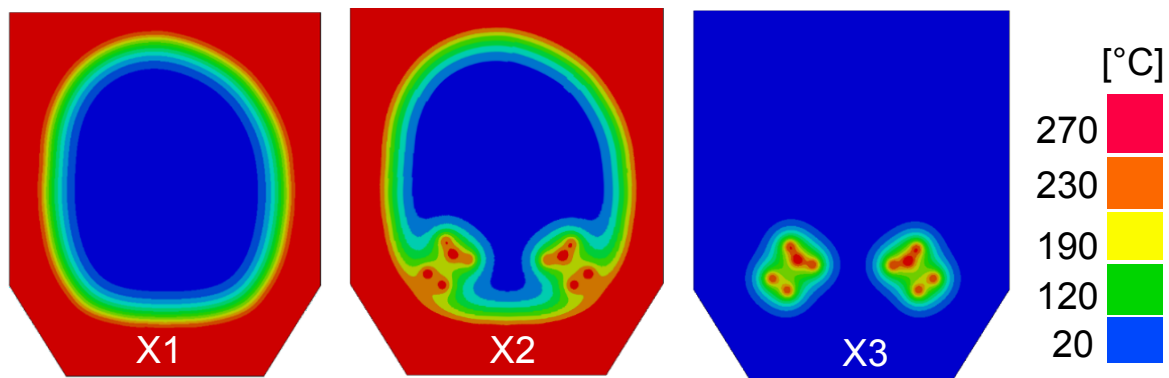


Figure 62 Conducted SHT layouts X1, X2 and X3 (temperature range: 20 °C to 270°)

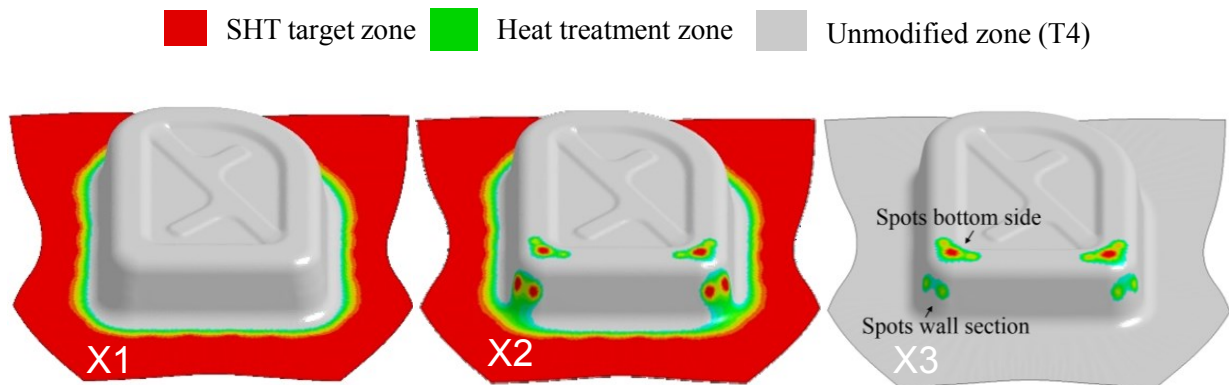


Figure 63 Plotted SHT temperature of 270 °C on the formed part (temperature range: 180 °C to 270 °C)

To achieve a heating time in a time frame of 1.5 s, for a SHT temperature of 270 °C, the heating procedure is carried out for the corresponding target SHT temperature of 360 °C. Due to the more extensive level of the heat plate temperature, the heating rate increases, and enables a fast heating time of 1.5 s. Figure 64 shows that different holding times occur for different heating times. By heating in 1.5 s, no holding time is conducted, whereby at a heating time of 8 s a holding time of 4 s, and for 14 s heating time a holding time of 10 s, is executed.

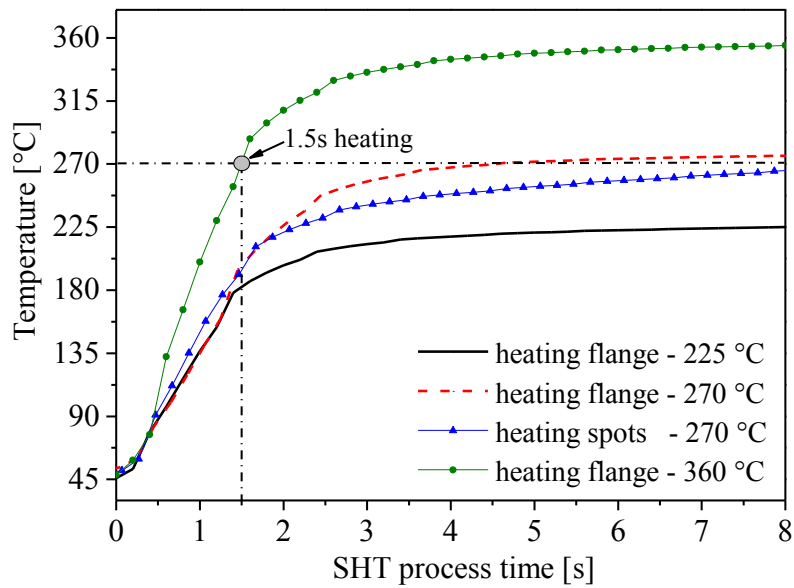


Figure 64 Profiles of the temperature over time measured in the blank for different heating configurations

The forming procedure is conducted immediately after quenching the heat treated blank at room temperature, except for the test sequence which analyses different storage times. With reference to the investigations in 7.2, the applied dry lubricant by the supplier was completely removed before SHT processes. Thus, to minimize the COF, adhesive wear, galling, and abrasion of the tool, an oil-based lubricant (WISURA ZO 3107/180) was applied on both surfaces of the blank, after the SHT process. The die and blank holder is controlled by distance plates with a thickness of 1.5 mm, and a blank holder force of 200 kN. In order to assess the deep drawing results, the major and minor strain distribution on each test part was measured in the area shown in Figure 65. Also, to present the improvement and potential of the SHT on deep drawing processes, the FLC's determined in 6.2 are used.

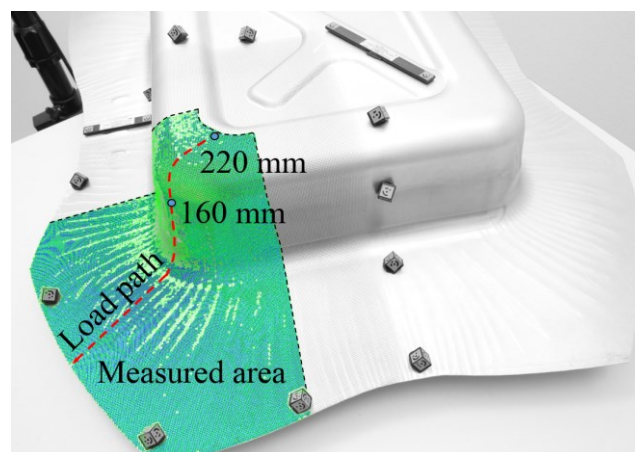


Figure 65 Area of measured major and minor strain distribution

8.2 Investigation of different SHT temperature levels

Figure 66 clearly shows the influence of SHT before the forming process in regard to the material failure. In a manufacturing process, without SHT, the material cracks at a drawing depth of 73 mm (Figure 66-right). A drawing depth of 85 mm could be produced, without crack deformations, by including SHT in the process chain with temperatures of 225 °C, 270 °C, 360 °C and an SHT process time of 8 s (Figure 66-left).

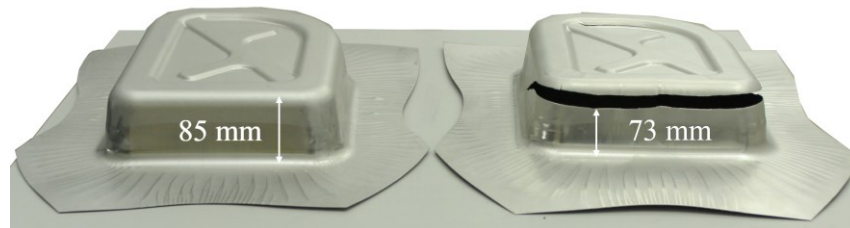


Figure 66 left: formed part through SHT; right: formed part without SHT in the process

To show the degree of the improvement in regard to the drawability of the AA6016 alloy, the forming limit diagrams for the area described in Figure 65, corresponding to each conducted SHT temperature is presented in Figure 67 and Figure 68. To be precise, Figure 67-left shows the FLD of the formed part by SHT with a temperature of 225 °C. This measurement result proves that the strain situation in the critical zone (Figure 40-left) reaches the minimum of resistance to necking at the deformation mode plane strain tension (Figure 24). Due to the increase of the SHT temperature from 225 °C to 270 °C, the strain distribution in the critical zone was lowered ($\Delta\epsilon$) to the FLC's safety margin of 20 % (Figure 67-right). Moreover, a further increase of the SHT temperature from 270 °C to 360 °C, leads to the highest decrease of major strain in the critical zone (Figure 68). This behaviour is explained by the increase of the reduction of strength in the flange's area, by the increased SHT temperature level (Figure 49-left and Figure 54). Thereby, it is important to mention that the SHT temperature of 360 °C also leads to an extended heat transition zone. The measuring point 8 (Figure 45), which is located in a distance of 15 mm to the flange's area, measures a temperature of circa 200 °C during SHT. This means that the SHT area grows by 15 mm compared to SHT with 270 °C temperature (Figure 47-right). The larger SHT zone explains the high increase of $\Delta\epsilon$ by considering the minor reduction of strength by using 360 °C compared to 270 °C SHT temperature (Figure 49-left).

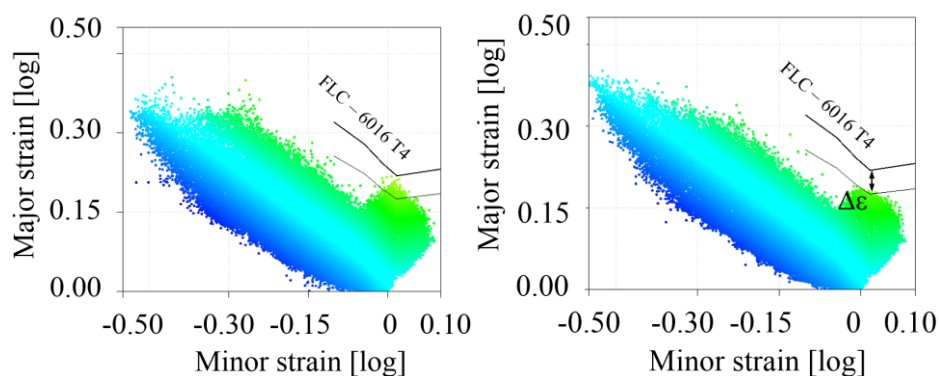


Figure 67 Forming limit diagram; left: SHT 225 °C; right SHT 270 °C

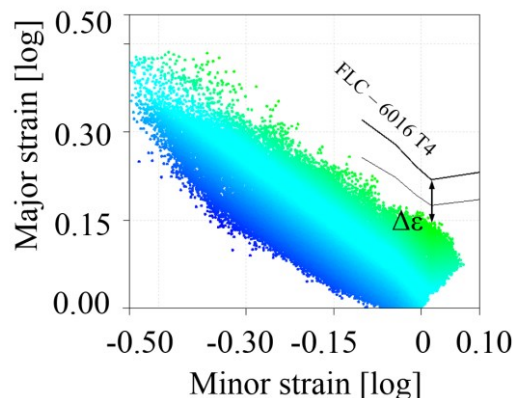


Figure 68 Forming limit diagram: SHT 360°C

8.3 Evaluation of different SHT layouts

Figure 67-right and Figure 69 show the modification of the forming limit diagrams caused by SHT layout X1, X2 and X3. Here, the SHT process is performed with a SHT temperature of 270°C and a SHT process time of 8s. Thereby, deep drawing without material failure was achieved by SHT layout X1 and X2. Figure 69-left illustrates the enhanced drawability, due to SHT layout X2, by increasing $\Delta\epsilon$ compared to the formed parts through using SHT layout X1 (Figure 67-right). Also an increase of strain is measured in the section of the wall through the execution of SHT in this area.

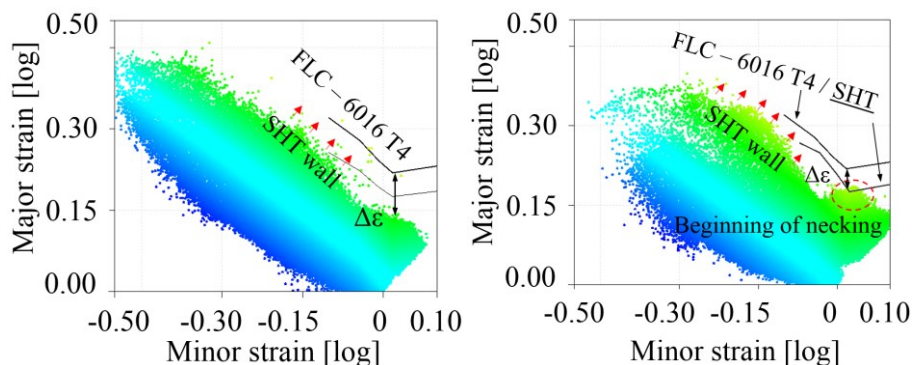


Figure 69 Forming limit diagram; left: SHT layout X2; right: SHT layout X3

The forming results when using SHT layout X3 show two parts, at a number of three tests, with material failure and different oriented crack formations, compared to manufacturing processes without SHT (Figure 71-right). The enhanced formability, due to SHT layout X3, is based only on active principle two (2.5.4), which means that the drawing force is not lowered through the SHT. Consequently, stresses in the SHT spots nearby the critical zone are increased, compared to SHT layout X2, and lead to larger thinning. To be more specific, Figure 70 shows the measured strain margin $\Delta\epsilon$ to the FLC (T4 - state) along the path marked in Figure 65. Besides, the use of SHT layout X3 proves that the determined strain margin $\Delta\epsilon$ is distinctly smaller within the part's bottom SHT area, than when using SHT layout X1 or X2 (Figure 70). The smaller $\Delta\epsilon$ is related to the reduced flow stress through SHT and a simultaneous larger stress situation, due to the non-heat treated flange area. This characteristic is also observed in Figure 69-

right, where larger strain is measured in the SHT wall zone, compared to when SHT layout X2 is used. Furthermore, the lower resistance to necking determined in 6.2, for the SHT treated AA6016 alloy, through a temperature of 270 °C, is also an indicator for the different orientated crack deformation (Figure 69-right and Figure 70). Accordingly, the crack formation starts on the part's bottom SHT area and can also be visually recognized by the beginning of local necking, at the only test part conducted with SHT layout X3, without material failure. Even though cracks occurred in the SHT area of SHT layout X3, also a reduction of the major strain in the critical radius could be measured, as shown in Figure 69-right and Figure 70.

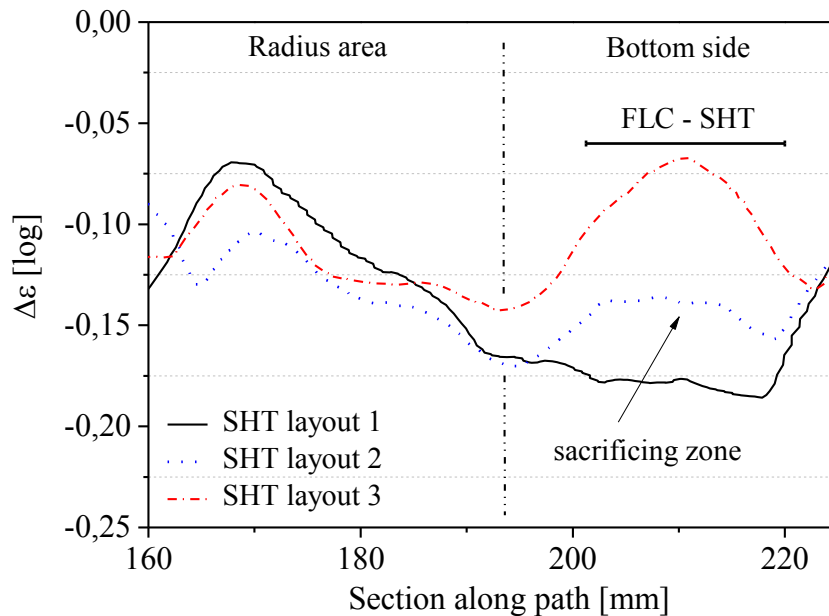


Figure 70 $\Delta\varepsilon$ along path SHT layout X1, X2 and X3



Figure 71 left: crack formation T4 state; right: crack formation SHT layout X3

8.4 Investigation of different holding times

In the following section, the influence of SHT holding times on deep drawing processes is analyzed. The material used in this study was heated up with SHT layout X1, at a temperature of 270°C and SHT process times of 1.5 s, 8 s and 14 s. The outcome of the measured forming limit diagrams in Figure 67-right and Figure 72 show a marginal deviation of the strain distribution to the corresponding holding time.

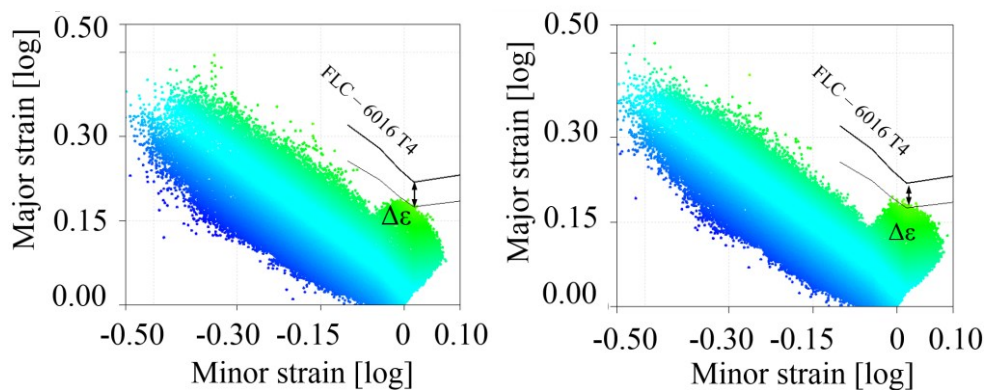
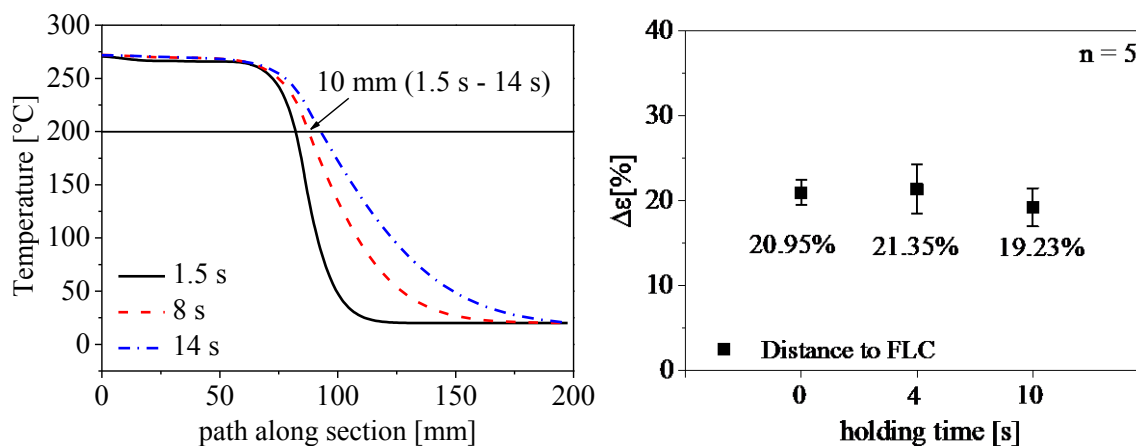


Figure 72 Forming limit diagram; left: 0 s holding time; right: 10 s holding

Figure 73-right illustrates the strain margin $\Delta\epsilon$ to the FLC, depending on the particular SHT holding time applied. In this diagram a small reduction of $\Delta\epsilon$, for a conducted holding time of 10 s, compared to 0 s and 4 s, can be observed. Thereby, it should also be considered that a larger holding time leads to a larger SHT zone. Therefore, Figure 73-left shows the temperature distribution determined by FEM simulation (10.3) along the path marked in Figure 65. When setting the SHT temperature level of 200 °C as the boundary of the SHT zone, the SHT zone to the corresponding holding time of 10 s grows about 5 mm compared to 4 s holding time (Figure 73-left). Thus, it can be assumed that the slightly larger SHT zone affects the drawability slightly positive. Hence, it can be concluded that SHT conducted through 10 s holding time shows lower drawing properties, compared to executed holding times of 0 s or 4 s. Due to the findings in [71], an influence of different heating rates, in a range of 93 K/s – 489 K/s, for the different conducted heating profiles in this investigation can be neglected.


 Figure 73 left: FEM temperature calculation along path; right: $\Delta\epsilon$ of different conducted SHT holding times

8.5 Investigation of different storage times

To investigate the effect of natural aging on the formability of AA6016, the blank was heat treated with SHT layout X2, 270°C SHT temperature and 8 s SHT process time. The effect of the storage times on the formability is illustrated through the forming limit diagram in Figure 74, Figure 75 and Figure 76.

Thereby, Figure 74-right shows an increase of 5.5 % plane strain at a storage time of 16 h compared to a manufacturing process with 0 h storage time (Figure 74-left). Due to 40 h and 100 h storage time a continuous increase of the major strain occurs (Figure 75). Additionally, when a storage time of 164 hours is applied (Figure 76) the FLD does not show a recognisable increase of major strain compared to 100 h storage time (Figure 75-right). For a better evaluation of these strain measurements, the distance between the maximum plane strain and the FLC ($\Delta\epsilon$) of the analyzed storage times is presented in Figure 77. This diagram shows a linear decrease of $\Delta\epsilon$ over the storage time until 100 h. Between 100 h and 164 h a constant strain characteristic occurs.

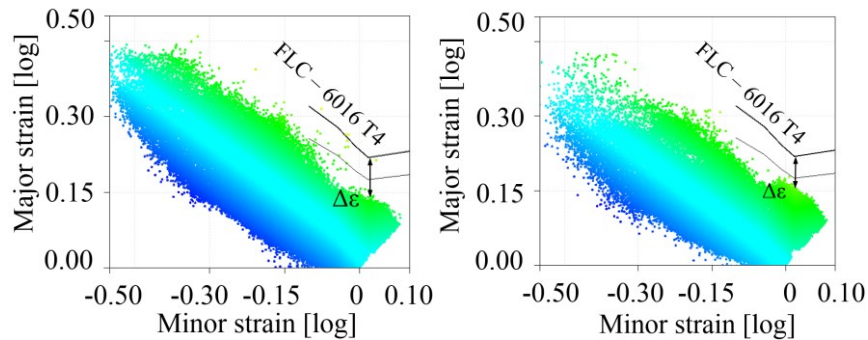


Figure 74 Forming limit diagram; left: 0 h storage time; right: 16 h storage time

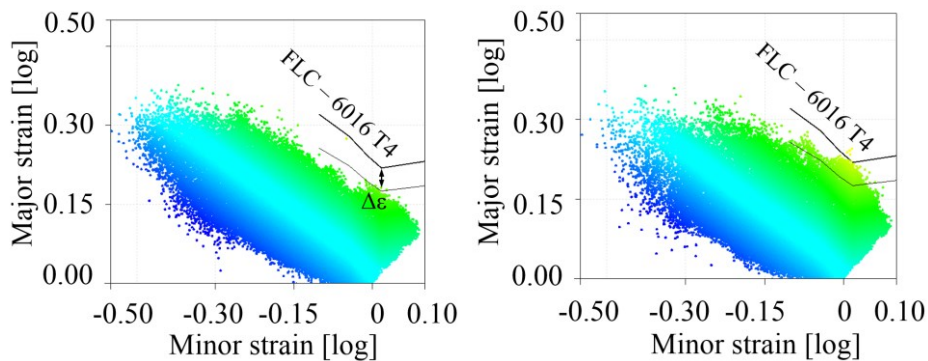


Figure 75 Forming limit diagram; left: 40 h storage time; right: 100 h storage time

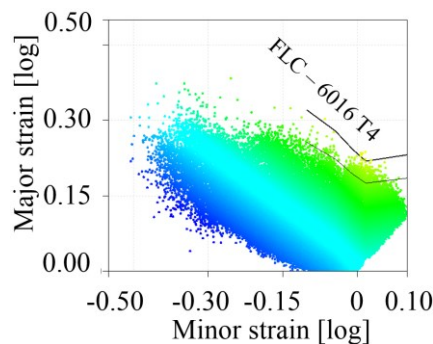


Figure 76 Forming limit diagram: 164 h storage time

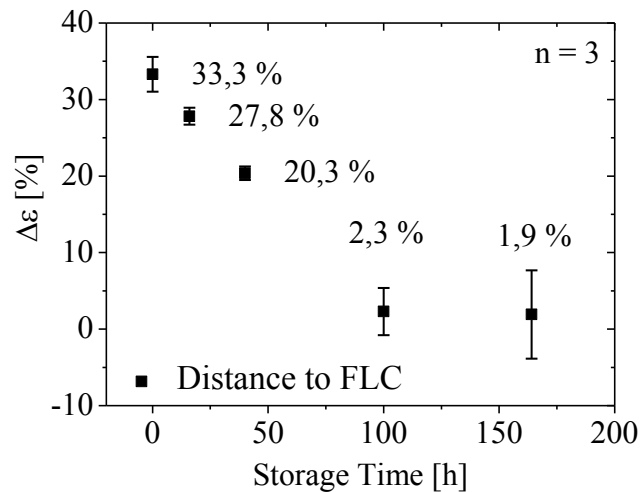


Figure 77 $\Delta\epsilon$ of different conducted storage times

8.6 Determination of the maximum drawing depth

A drawing depth of 115 mm could be achieved due to the execution of SHT and by using the optimal SHT process parameters. These parameters are as follows: the SHT layout X2, SHT temperature of 270 °C and the SHT process time of 8 s. During the manufacturing process without SHT, cracks occurred at a drawing depth of 63mm (Figure 78).



Figure 78 left: formed part due to optimal SHT process parameter; right: formed part without SHT

8.7 Conclusion

In brief, the SHT with the objective of modifying the formability of an AA6016 alloy is successfully performed through a one side conduction heating. A large improvement of the drawability is measured when an SHT is conducted through the optimal SHT temperature of 270 °C (determined in chapter 5). By applying additional SHT spots near the critical zone, the critical major strain is reduced considerably, compared to blanks which are only heat treated in the flange section. However, the design of the SHT layout plays an essential role in terms of a robust forming process. It is noted that the lowered FLC, due to the optimal SHT temperature of 270 °C, influences the robustness of the forming process when additional SHT areas are applied to the SHT area in the flange section. Therefore, the findings obtained in this study suggest a combination of SHT in flange sections and small spots near to the critical zone.

Analyses of the influence of SHT process parameters on the drawing performance

Furthermore, varied SHT holding times of 0 s and 4 s have shown insignificant deviations in the FLD. A conducted holding time of 10 s lead to a slight reduction of formability compared to 0 s and 4 s holding time. The storage time between heat treatment and forming process has a significant impact on the deep drawing result. In fact, storage times higher than 16 hours showed considerable changes in the forming limit diagram. However, natural aging in the time period of 100 hours to 164 hours have not shown considerable influence on the drawing performance.

9 Analyses of the influence of SHT and paint baking on the final part properties

In chapter 9, the mechanical properties of a formed part, manufactured through a multi-stage forming process, are investigated. The aim of this analysis is to evaluate the influence of SHT and paint baking on the parts properties. This is achieved by using the heating facilities described in 4.8.2 in order to produce tailored properties on the AA6016 (Superlite 220 ST) material. For the subsequent drawing process the forming tools shown in 4.7.1 are used. For measuring the mechanical properties tensile specimen according to DIN 50125 are cut out from the part and are tested according to DIN 1002. The artificial aging process is conducted in a conventional furnace. The experimental procedure is discussed in 9.1.

9.1 Process control and used process parameters

Figure 79 shows the process sequence of the conducted heating and forming processes. Before the SHT is conducted, in a time frame of 8 s and through 270 °C temperature, the dry lubricant applied by the supplier is removed from the blank surface. After the SHT procedure the blank is quenched at room temperature and formed after a conducted storage time of < 1 hour. To ensure a proper drawing performance, an oil-based lubricant (WISURA ZO 3107/180) is applied. Subsequently, the drawing process is performed in two forming steps. This multi-stage forming process leads to a different critical zone, which is shown in Figure 40-right. By using SHT layout X2 in this process, crack formations located in the area of the SHT spots (wall zone) have occurred at drawing stage two. Therefore, SHT layout X1 is used for the conducted SHT process. To produce a part which exhibits a proper surface quality, the shape of the blank boundary is optimized to minimize wrinkling and to avoid crack formations. Moreover, the forming process is executed by a set blankholder force of 240 kN in both forming stages. Finally, in the last process step, the artificial aging process is executed through the temperature of 185 °C and the time frame of 20 minutes. To evaluate the influence of the paint baking process on strength and ductility, specimens which are not artificially aged are characterized as well.

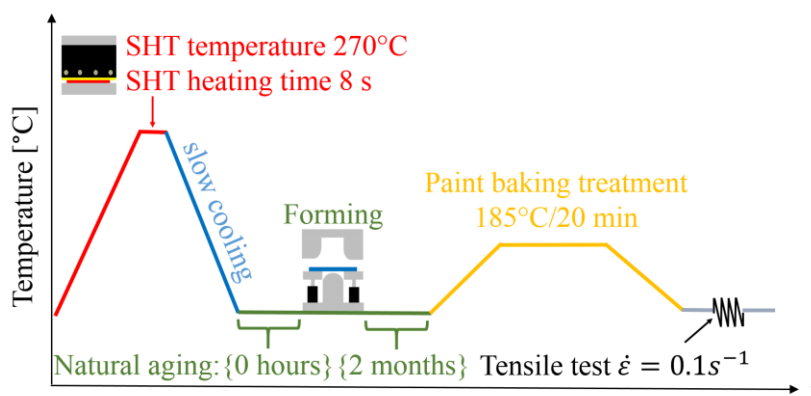


Figure 79 Process control SHT, Forming process and paint baking

9.2 Forming result multi-stage process

Figure 80-right shows the manufactured part which underwent a conventional forming process. More specifically, this means that no heat treatment is applied. Crack formations in the first forming stage are avoided through optimizing the blank shape. In the second step the material cracks in the critical zone marked in Figure 40-right. By applying SHT on the flat blank, the part is formed in the second forming stage without having material failure (Figure 80-left).



Figure 80 Multi-stage forming process: left: formed part through SHT; right: formed part without SHT in the process

9.3 Mechanical properties of the drawn part

To analyse the properties of strength and ductility, a number of 13 specimens of each test part is cut out in the bottom area, the wall zone and at the bulge zone of the part (Figure 81). Figure 81 also shows the affected area through the SHT, such as the flange area, and the beginning of the wall and the bulge zone.

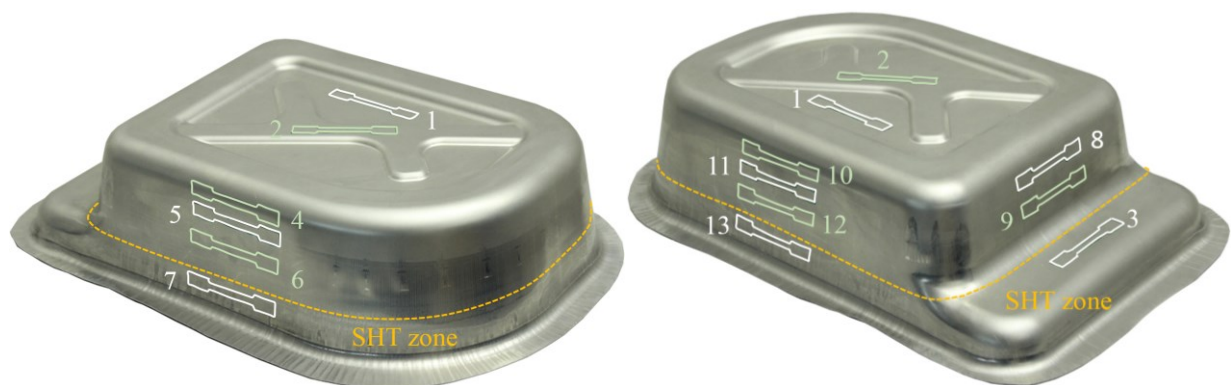


Figure 81 Marked areas of cut out specimen

Figure 82 shows the measured yield strength and uniform elongation of the marked specimens. In these diagrams, Figure 82-left shows the yield strength to the corresponding specimen. Thereby it is measured that the specimen cut out in the SHT area shows a larger paint baking response, compared to specimen cut out in the T4 zone. For evaluating the strength distribution, it should be noted that the plastic strain on the formed test parts is not homogeneously distributed. Moreover, different load states do occur at different

areas of the part which affects the beginning of yielding. Owing to these influences the specimens which are located in the wall zone (12 and 13), which show similar levels of plastic strain and the same load state can be used for a more precise validation of the interaction between SHT and paint baking in terms of strengthening. By comparing the determined strength of these specimen, it can be observed that the level of strength of the specimen located in the SHT area (13) is larger than the obtained strength level of the cut out specimen in the T4 zone (12), when paint baking is conducted. The analysed specimens, taken from the bulge zone (3), exhibit a low level strength of circa 150 MPa when no paint baking is executed. This can be associated with insufficient strengthening of the material during forming. However, by conducting paint baking on the specimen, the material achieves the same level of strength as the largest measured strength in the area which is not modified through SHT before forming (specimen 6 and 12).

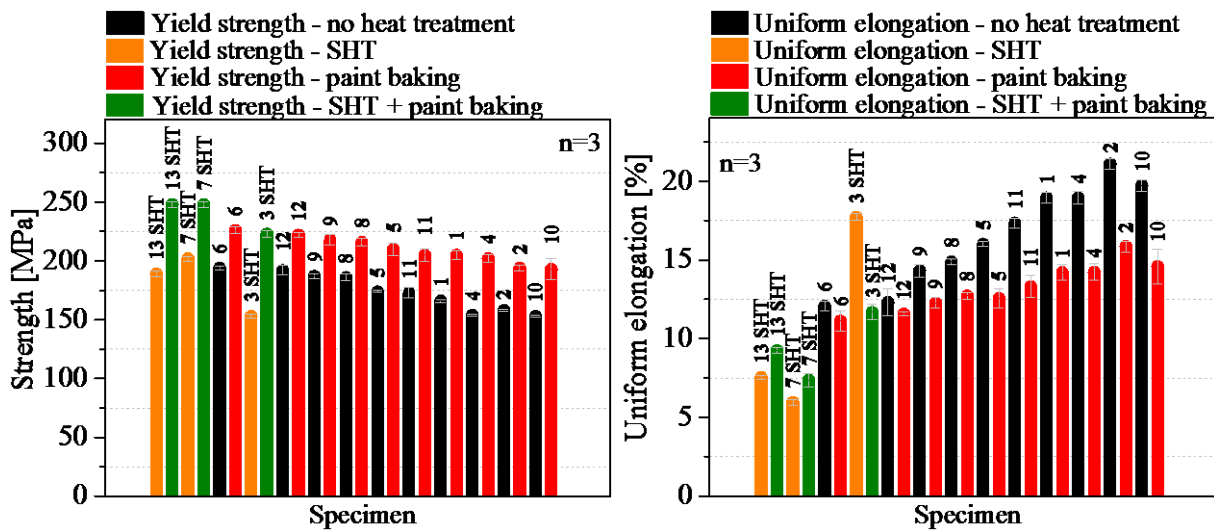


Figure 82 Mechanical properties of formed part: left: yield strength [MPa]; right: uniform elongation [%]

Figure 82-right illustrates the measured uniform elongation of the cut out specimens shown in Figure 81. These results show, especially for the analysed specimen in the T4 zone and bulge zone (3), an obvious trend regarding the loss of ductility when paint baking is used. Contrary to this, the specimens located in the wall zone and SHT area (7 and 13) have shown better performance regarding ductility when paint baking is executed. In [136] and [137] it was found that pre-straining has a substantial effect on the subsequent precipitation process during paint baking. Based on these results, the reason for enhanced ductility properties might be caused by the varying occurrence of pre-straining conditions, for instance, by the Bauschinger effect, which occurs when the material is formed in the radius area or by the change of the strain path when the spot of the specimen shifts from flange to wall. In addition, Figure 83-left illustrates the change of the location of the specimen 7 and 13 in the first and second forming stage. During forming, the spot of the cut out specimen starts in the flange area, passes the radius area and finally ends in the wall zone. A further reason for enhanced ductility after paint baking could be that the material in the direction of the cut out specimen is primarily formed through a large degree of compression instead of tension, due to the occurrence of shear stress in the flange area.

In [138], authors and co-workers have found out that tensile specimen, which are pre-strained (uniaxial stress state) with 15 %, show an improved ductility when paint baking is conducted. It is assumed that the

improvement in ductility might be caused by an active recovery process during paint baking of the pre-strained material. To illustrate, Figure 83-right shows the history of the effective plastic strain during forming, determined through FEM simulation, at the location of the analysed specimen. It can be clearly seen that the specimen number 7 and 13 are much more pre-strained during forming than other specimen. The higher degree of deformation of these two specimens compared to the remaining specimens might be also a reason for enhanced ductility by using paint baking.

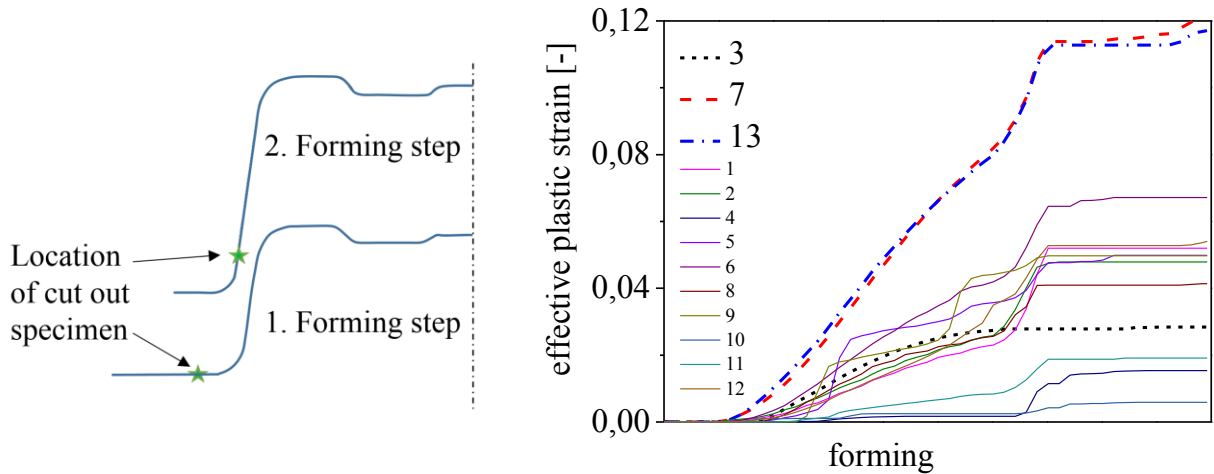


Figure 83 left: position of specimen in first and second forming stage; right: effective plastic strain history of specimen during drawing process (FEM simulation)

9.4 Conclusion

On the whole, a multi stage forming process has been successfully conducted using SHT before forming. It is observed that SHT layout X2, which has shown the best drawing performance in the first forming stage, has led to material failure in the multi stage forming process. Moreover, this underlines the importance of the SHT layout design and the necessity of virtual development. Besides, applying paint baking on the formed part, lead to a strengthening of the material on the entire component. The AA6016 material in T4 condition has shown an almost evenly increase of strength due to paint baking by comparing different zones of the part, which have consequently undergone different load states during forming. Differences in strengthening are clearly observed for SHT affected zones. The use of the optimal SHT temperature of 270 °C, determined in chapter 5, has shown much higher hardening through paint baking, in particular for zones which are insufficient strengthened due to work hardening. Simultaneously, the loss of ductility occurs in most zones of the part when paint baking is performed. To investigate the enhancement of ductility in the SHT zone, which exhibit different pre-straining conditions during forming, the use of a DSC analysis of the specimen cut out after the first forming step (flange) and the second forming step (wall) would be crucial.

10 FEM simulation model

In the following chapter the SHT process and subsequently the forming process which are executed in chapter 8, are modelled in the FEM software LsDyna and validated through experimental data. Two different model approaches are used to describe these processes virtually. These are based on both an only mechanical, and on a thermo-mechanical coupled description of the manufacturing process. More specifically, the two approaches differ in terms of modelling effort and the amount of the required material data. The performances of these approaches are evaluated regarding accuracy, by comparing simulation results with measurement data from the formed part. To achieve this, the built simulation models are validated with the measured major and minor strain distribution in the marked area in Figure 65. Also, the accuracy of the simulated sheet thickness compared to the sheet thickness of the formed part is an important validation criterion. Therefore, the measured sheet thickness along the path, marked in Figure 65, is compared to the simulation result. Out of this validation, the capability for the virtual process design for industrial application is determined.

10.1 Material modelling

For modelling the plastic material behaviour during forming, the determined material data in chapter 6.1 are taken to approximate flow curves of the AA6016. Hence, flow curves for the T4 state and for softened conditions, caused by different conducted SHT temperatures, are obtained by using the hardening law of Hockett-Sherby [95]. To model the beginning of yielding in dependence on the multi axial stress state, the yield criterion Barlat1989 [139] and the more advanced Barlat-Yld2000-2d [114] are used. It needs to be noted that the Barlat-Yld2000-2d model requires more input parameters, compared to the Barlat1989 model. To analyse the benefit of the Barlat-Yld2000-2d model, which consequently exhibits higher effort in material characterization toward the Barlat1989, the performance of both models is validated through the in-plane tensile test and planar simple shear test. Apart from the evaluated tensile tests, also the measured sheet thickness and strain distribution of the formed test part is compared, with the simulation results obtained by using both yield criterions.

10.1.1 Mechanical approach

Blanks which are partial heat treated due to a SHT procedure, exhibit an inhomogeneous strength distribution. Thereby, the inhomogeneous strength properties depend on the generated blanks' temperature distribution caused by the SHT. In 5.1.2 it is shown that negligible deviations occur by comparing the material in T4 state and at softened condition through an SHT temperature of < 200 °C (Figure 49-left). Based on this, the blank can be characterized in a T4 and a SHT zone, if the heat transition zone is neglected. The heat transition zone occurs circa between 200 °C SHT temperature and the maximum reached temperature at the heat treatment process. For instance, a pronounced heat transition zone has been observed at SHT layout X2 (Figure 63) in particular between two separated SHT zones. The impact of neglecting the heat transition zone on the simulation result is also validated in chapter 10.

The concept of the mechanical approach is shown in Figure 84. In order to explain the concept, a tensile specimen is partially SHT treated in the middle area of the specimen, through the optimal SHT temperature of 270 °C. To model the inhomogeneous material characteristic of this specimen, two

different flow curves are assigned to the specimen. In this example, the flow curves determined in chapter 6.1 for the AA6016 alloy in T4 state and after SHT with a temperature of 270 °C are used. In conclusion, instead of modelling the heat treatment simulation which generates the ability of THTB, the sheet metal is described only through the material properties of the T4 state and the material properties obtained through the SHT at temperatures of 270 °C (Figure 84).

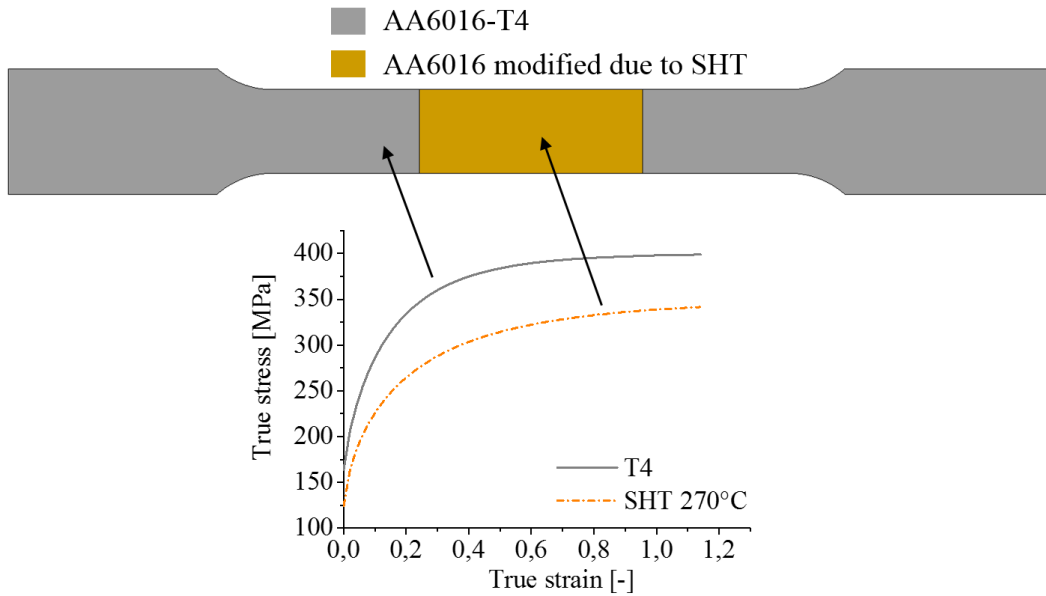


Figure 84 Scheme of mechanical approach applied on a partial SHT treated tensile specimen

10.1.2 Thermo-mechanical coupled approach

Contrary to the mechanical approach, the thermo-mechanical coupled approach also considers the modification of the material caused by temperatures lower than the maximum SHT temperature. This means that also the temperature characteristic in the heat transition zone is described properly. To model this, the simulation software LsDyna provides an additional function for the material models Barlat1989 and Barlat-Yld2000-2d. This function enables the possibility of simulating a manufacturing process involving preforming, springback, heat treatment and postforming. In each step, the required history for the subsequent process step, such as strain, strength or temperature, is transferred to the next. For the process conducted in this thesis, to model the entire manufacturing process, only the heat treatment on the flat blank and the postforming process are required. Figure 85 shows the tensile specimen from section 10.1.1 which is heat treated in the middle zone through the SHT. Moreover, this heat treatment simulation is performed thermo-mechanically coupled. The coupling between the thermal and mechanical problem is implemented by storing the maximum calculated temperature (T_{max}), which is distributed on the specimen, in the used material model. To generate an inhomogeneous strength distribution in the final postforming step (Figure 85) the yield strength is reduced through the Hockett-Sherby approach shown in equation 11.

$$\Delta\sigma = b - (b - a)\exp\left(-c[\varepsilon_p - \varepsilon_p^0]^d\right) \quad \text{equation 11}$$

Where a, b, c and d are parameters depending on T_{max} and ε_p^0 (pre-strain) of the blank.

For the relevant manufacturing process in this thesis the equation 11 can be rewritten to equation 12, due to the blank is formed in non pre-strained condition.

$$\Delta\sigma = b - (b - a)e^{-c[\varepsilon_p]^d} \quad \text{equation 12}$$

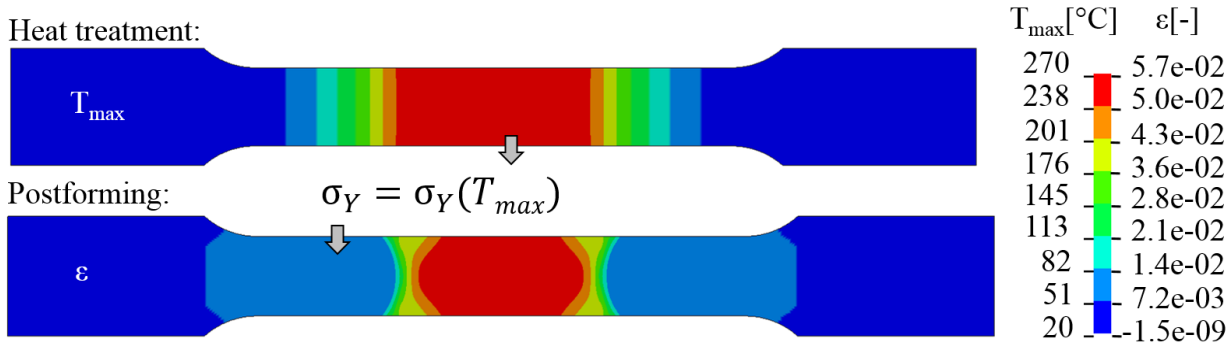


Figure 85 Scheme of thermo-mechanically coupled approach applied on a partial SHT treated tensile specimen

The parameters a , b , c and d in dependence on the SHT temperature, shown here in Figure 86, are determined as follows: In the first place the flow curves for the AA6016 material in T4 and SHT (SHT temperature of 270 °C) condition are approximated through the Hockett-Sherby hardening law, by using the obtained tensile and bulge test data from 6.1. The coupling between true stress and strain data of bulge and tensile test did not require additional mathematical methods because of a good correlation of both curves (Figure 54). Due to the obtained bulge test data, which provides information on larger strain levels, for the state of T4 and for softened condition (SHT temperature of 270 °C) the so-called free parameters C and N as well as the saturation stress value A can be determined accurately. These parameters are needed to define the flow curve mathematically to larger strain levels by using equation 13.

$$\sigma_Y = A - (A - B)e^{-C[\varepsilon_p]^N} \quad \text{equation 13}$$

For reduced strength conditions caused by conducted SHT temperatures of 200 °C, 230 °C and 255 °C, only tensile tests are performed. Consequently an accurate determination of the parameters A , C and N is not given. This is, however, explained by the limitation of the conventional uniaxial tensile test which provides valid data for the approximation only until values of the uniform elongation (2.9.1). For that reason, a linear interpolation through equations 14, 15 and 16 is used between the obtained parameters, by bulge test at T4 state and at softened condition with an SHT temperature of 270 °C.

$$A = T * (-1.4) + 730 \quad \text{equation 14}$$

$$C = T * (-95.45) + 618 \quad \text{equation 15}$$

$$N = T * (-954.54) + 943 \quad \text{equation 16}$$

Through these linear functions the values for A , C and N are determined and used to approximate the flow curves shown in Figure 87-left, for the AA6016 material, heat treated through temperatures of 200 °C, 230 °C and 255 °C. Table 10 illustrates the obtained Hockett-Scherby parameters which are required to approximate the flow curves shown in Figure 87-left.

FEM simulation model

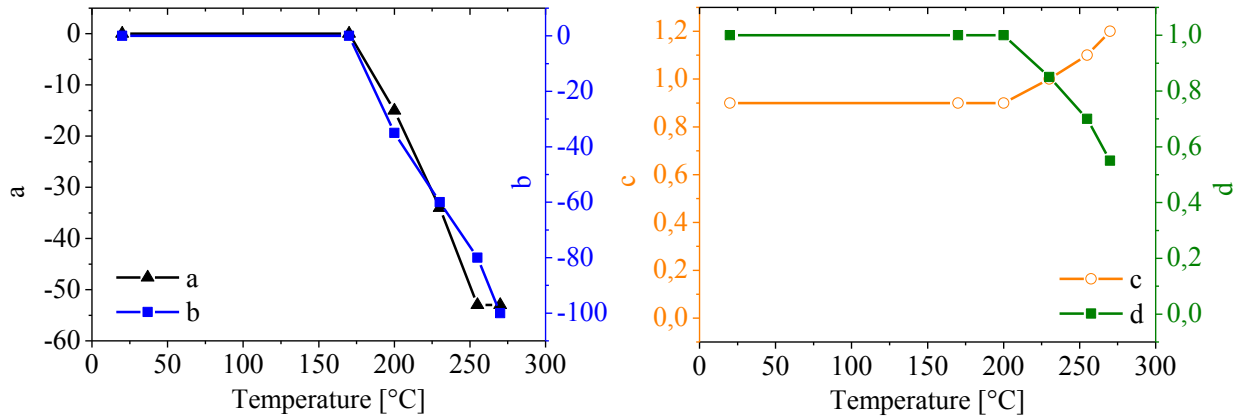


Figure 86 Hocket-Scherby parameters: $a = a(T_{max})$ $b = b(T_{max})$ $c = c(T_{max})$ $d = d(T_{max})$

Before the Hocket-Scherby parameter a , b , c and d can be obtained, the flow curves, which exhibit a reduced strength characteristic through SHT are subtracted of the material's flow curve in the T4 state (Figure 87-right). Hence, the $\Delta\sigma$ for 200 °C, 230 °C, 255 °C and 270 °C SHT temperatures depending on the degree of deformation are determined. For instance, Figure 87-right shows the $\Delta\sigma$ over strain which characterises the amount of the reduced stress due to a conducted SHT procedure with 255 °C. The obtained characteristic of $\Delta\sigma$ is used to fit the true stress and strain data calculated through equation 12 by adjusting the parameters a , b , c and d in excel. These parameters are illustrated in Table 11, depending on the conducted SHT temperature.

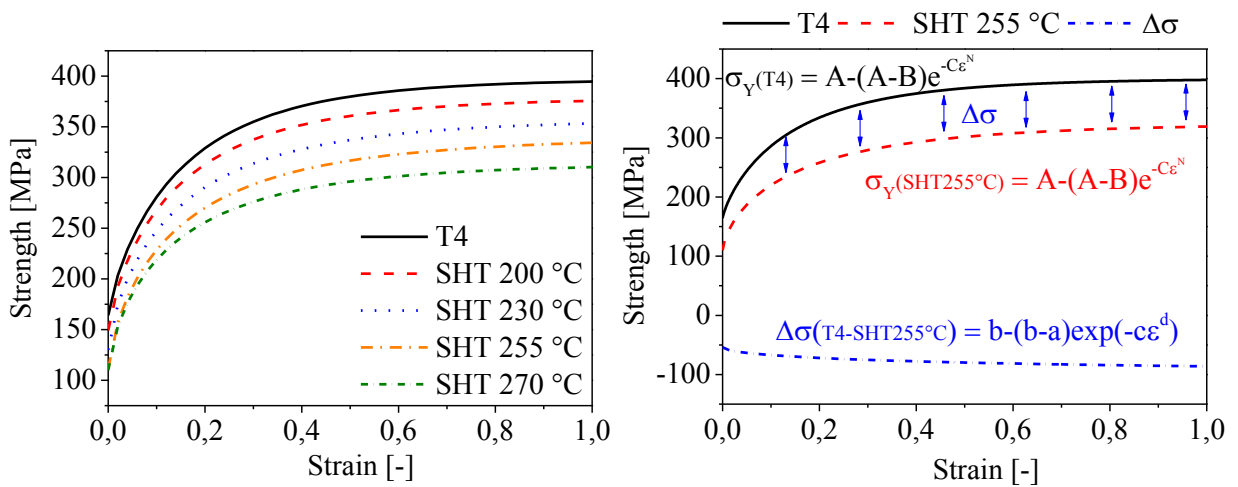


Figure 87 left: approximated flow curves through Hocket-Scherby law; right: Explanation of $\Delta\sigma$

Figure 86 shows that through increasing SHT temperatures, the parameters a , b and d are decreasing almost linearly, except the parameter c . The increasing characteristic of parameter c means, that at higher strain levels, the gradient of flow curve is decreasing when the SHT temperature increases.

Table 10 Determined Hocket-Scherby parameters A, B, C and D [σ_Y]

AA6016 - state	A	B	C	N
T4	400	164	4.700	0.810
SHT 200 °C	379	149	4.385	0.778
SHT 230 °C	357	130	4.070	0.747
SHT 255 °C	339	111	3.809	0.720
SHT 270 °C	325	110	3.600	0.700

Table 11 Determined Hocket-Scherby parameters a, b, c and d [$\Delta\sigma$]

AA6016 - state	a	b	c	d
T4	0	0	0.9	1
SHT 170 °C	0	0	0.9	1
SHT 200 °C	-15	-35	0.9	1.00
SHT 230 °C	-34	-60	1.0	0.85
SHT 255 °C	-53	-80	1.1	0.70
SHT 270 °C	-53	-100	1.2	0.55

10.1.3 Modelling of the yield locus through Barlat1989 and Barlat-Yld2000-2d

In the following section the eight coefficients which are needed to define the yield locus by the yield criterion Barlat-Yld2000-2d are determined. In order to identify these coefficients the software FORM-CERT is used [140]. In fact, FORM-CERT is a commercial code which is developed by Jurco and Banabic [141]. In this code the yield criterion BBC 2003 [142] is implemented. However, Barlat [143] found that the BBC 2003 criterion is the same as the Barlat-Yld2000-2d criterion. Thereby it should be noted that the development procedure by the two authors was different. To be more specific, the BBC 2003 model is developed by adding coefficients to Hershey's formulation, while Barlat has used two linear transformations for the Yld2000-2d model. Based on these findings, the software FORM-CERT has been used to determine the eight anisotropy coefficients of the BarlatYld2000-2d (α_{1-8} : Table 12). The Barlat-Yld2000-2d criterion requires eight coefficients (α_{1-8}) which are determined through eight mechanical material parameters (2.10). Six of these eight parameters are determined in chapter 6.1, such as the σ_0 , σ_{45} , σ_{90} , r_{00} , r_{45} , r_{90} for the AA6016 in T4 state (Table 9). The biaxial yield stress (σ_b) is set to the same value as the yield strength in rolling direction (σ_0). This is justified by the good agreement between tensile test data and bulge test data. The biaxial anisotropy coefficient (r_b) is assumed to be one for the determination procedure of α_{1-8} . This assumption is based on the results of the research activities in [115–120], which have modelled the AA6016 T4 material in a good agreement with experimental data, by using a biaxial anisotropy coefficient of one. A further parameter which is needed to define the shape of the yield locus, is the material parameter m , which is usually defined as the value of eight for faced-centred cubic materials (FCC), such as aluminum and a value of two for body-centred cubic materials (BCC), such as steel [139]. The determined parameters for the yield criterions Barlat1989 and Barlat-Yld2000-2d are shown in Table 12 and Table 13.

Table 12 Parameter for the Barlat-YLD2000-2d model

α_1	α_2	α_3	α_4	α_5	α_6	α_7	α_8	m
0.67	0.96	0.98	0.98	1.07	1.02	1.08	0.98	8

Table 13 Parameter for the Barlat1989 model

r_{00}	r_{45}	r_{90}	m
0.69	0.43	0.98	8

In Figure 88 the used yield criterions are validated through measurement data obtained from tensile tests by using differently shaped tensile specimens which are described in 4.2.2 and 4.2.3. To evaluate the accuracy of these yield criterions, the tensile test is modelled through the simulation software LsDyna, by using the yield criterion Barlat1989 and Barlat-Yld2000-2d. For validation, the simulated force displacement curves are compared to the force displacement results obtained from the material tests. In Figure 88-left it can be observed that the simulation results generated though the yield criterion Barlat1989 show deviations, in particular for the simulated EU01 and EU04 specimen. This means that the beginning of yielding, caused by the load state of plane strain and the state between uniaxial strain, and plane strain is not accurately described though the yield criterion Baralt1989. Contrary to the simulation results obtained by the yield criterion Barlat1989, the simulation results using the criterion Barlat-Yld2000-2d exhibit an excellent agreement for all conducted specimen with the experimental determined data. The impact of using the model Barlat1989, which requires less effort in material characterisation, instead of Barlat-Yld2000-2d for drawing simulations is analysed in 10.3.1.

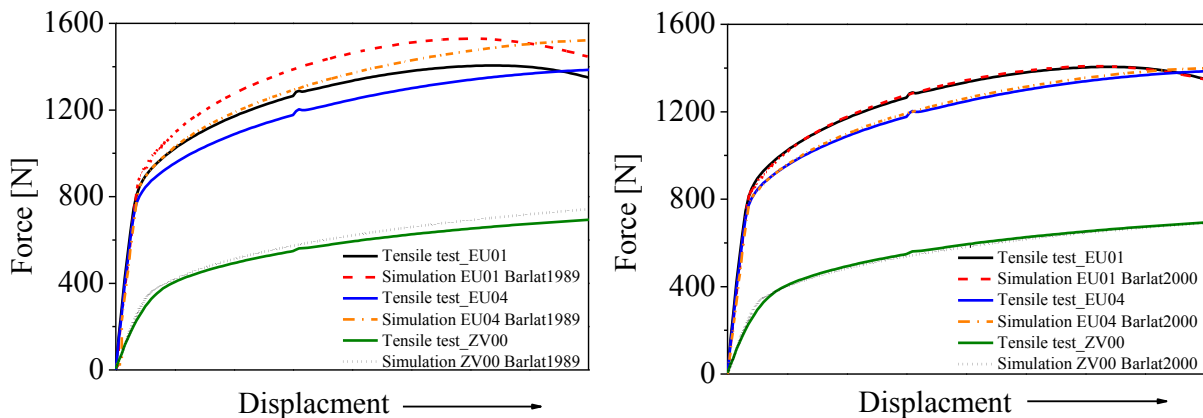


Figure 88 Validation of tensile test (AA6016 T4) and simulation through differently shaped specimen (EU01, EU04, ZV00) left: Barlat1989; right: Barlat-Yld2000-2d

Based on findings of [121] the change of the yield locus shape due to SHT is neglected in the simulation model (2.10.1). Also the determined r-values in 6.1, for AA6016 alloy in T4 state and in SHT conditions, have not shown considerable changes, which can be seen as an indicator of the yield locus shape.

10.2 SHT simulation of a partial heat treated tensile specimen

To validate the influence of neglecting the heat transition zone in the FEM model, by using the mechanical approach, the SHT facility described in 4.4 and the tested tensile specimen is modelled in LsDyna. Thereby the simulated major strain distribution along a path located in the middle of the specimen is compared to the measured major strain distribution of the tensile specimen. The major strain of the tensile specimen is measured through the measuring system ARMIS (4.5.2). Furthermore, the simulated material behaviour in the heat transition zone, by using the thermo-mechanical approach, is also validated by comparing the calculated and measured major strain. Within this validation procedure, the determined HTC in 6.3 is evaluated by comparing the measured temperature inside the specimen, when the SHT is conducted, to the calculated temperature through the FEM model.

10.2.1 FEM Simulation model – input parameter

The tensile specimen is modelled through 4 node quadrilateral elements and a Belytschko-Tsay element type with 2 through-thickness integration points. Thereby it is important to mention that an element size of 0.25 mm in the area of the heat transition zone, and 1 mm element size for the remaining specimen, is used. The small element size in the heat transition zone is necessary to avoid numerical errors when high temperature gradients of the heat flow along the specimen occur. The tools are modelled through tetrahedral volume elements, with an element edge length of 2 mm and a fully integrated characteristic (Figure 89-left). Both, specimen and tools are defined as rigid in the conducted FEM model, which means that the thermal expansion of the specimen is neglected. The heat loss from specimen to the ambient is modelled by using a convection boundary condition with a HTC of 5 W/m²K. The heat transfer between blank surface and tool is described through an HTC of 3000 W/m²K for a corresponding contact pressure of 10 MPa (6.3). Initial conditions are applied on the specimen by setting the measured temperature of 50 °C, which is determined at the experiment shortly before contact between tool and sheet has started as well as an initial tool temperature of 270°C. In order to model the heat transfer from the heating coil into the heating plates, a simplified approach is used. Therefore, a constant temperature of 270°C is applied on the surface of the milled recess where the heating coil is located (Figure 89-left). The thermal behaviour of tools and specimen is modelled through thermal isotropic material model. For the AA6016 T4 aluminum material a heat capacity of 900 J/kgK and a thermal conductivity of 190 W/mK is applied [144]. A thermal heat capacity of 460 J/kgK and a thermal conductivity of 50 W/mK is assigned to the tool material (C45U – 1.1730) [145]. Moreover, in order to speed up the simulation model, a thermal speed up factor of 100 is used.

10.2.2 Validation and discussion of the simulation results

For evaluating the determined HTC in 6.3, the temperature profiles illustrated in Figure 89-right are compared. Hence, the performance of the SHT simulation shows a good agreement to the measured temperature of the specimen.

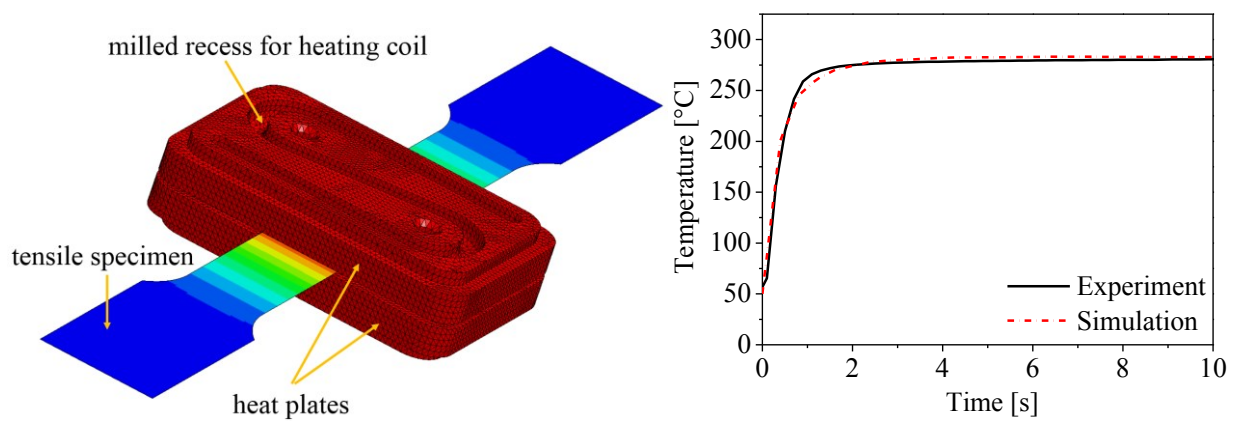


Figure 89 left: modelled SHT facility (heat plates and specimen); right: measured temperature inside the blank versus simulated temperature

For validating the impact of neglecting the modelling of the heat transition zone in the simulation model, the calculated major strain along a path on the tensile specimen is compared to the measured major strain data (Figure 90). Figure 90-left shows the simulated and measured major strain distribution on the tensile specimen after 12 mm straining. It can be noticed that the simulation results obtained through the mechanical approach exhibit a sudden change of major strain in the transition zone between SHT and T4. This behaviour is also illustrated in Figure 90-right, where the major strain along a path shows an abrupt increase of strain at the boundary of the SHT zone, compared to the results obtained by the tensile test. Contrary to these results, the simulated major strain obtained through the thermo-mechanical coupled approach shows a smooth transition and a clearly recognisable transition zone in Figure 90-left. The results acquired through the thermo-mechanical coupled model shows a good correlation to the measurement data except in the area where temperature near to 200°C occur. This can be observed at a position of 50 mm and 150 mm along the path marked in Figure 90-left where deviations occur between data obtained from simulation and the experiment. This behaviour might be explained through the significantly lower heating rate in the transition zone, especially compared to the heating rates in the SHT zone (Figure 91).

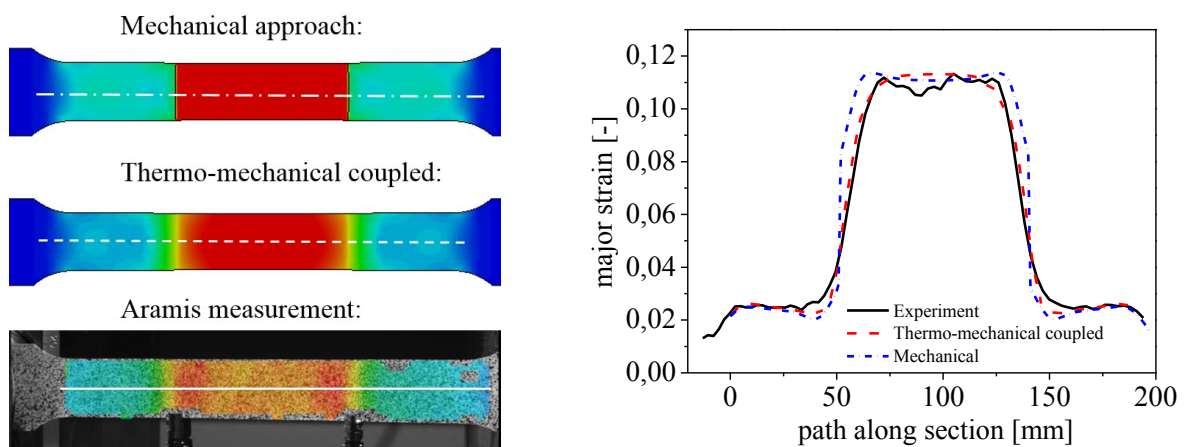


Figure 90 left: simulation results of major strain (mechanical and thermal-mechanical coupled approach) and Aramis measurement; right: simulation results versus measured data along path

The simulation results show a heating rate of 30 K/s and lower in the area of the heat transition zone (number 1-4) which might be an indicator for a different softening behaviour compared to the faster heating rates performed in the middle of the SHT zone (number 5). The heating profiles with the numbers 1 to 4 compared to the profile of the number 5 are shown in Figure 91-right. In order to model this effect in the FEM simulation, a heating rate depending material model would be required.

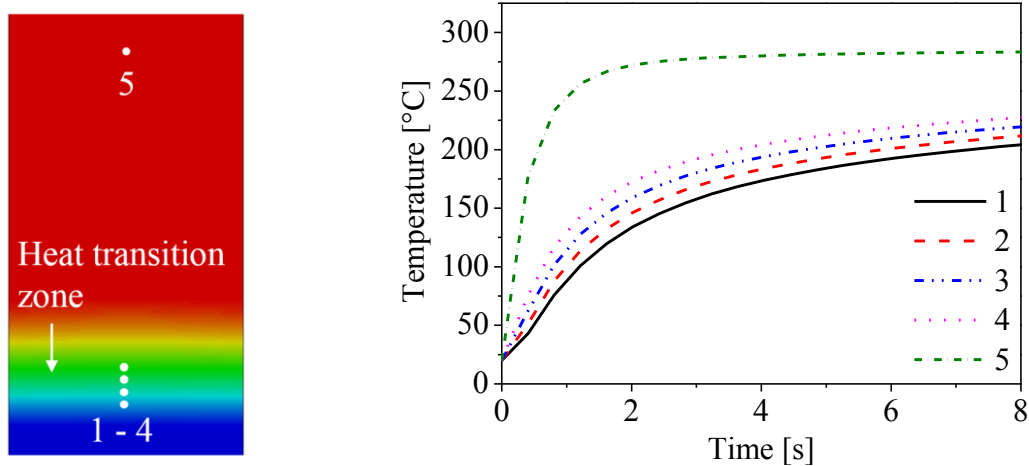


Figure 91 left: simulated temperature in the heat transition zone; right: temperature history in the marked spots

10.3 SHT simulation and forming simulation

In the following section the SHT and the forming processes conducted in chapter 8 are modelled and validated. To model the blank, a three node triangular element and a Belytschko-Tsay element type with two through-thickness integration points is used. Therefore, an element size of 0.6 mm in the area of the heat transition zone and 2 mm element size for the remaining area of the blank is used. The tools of the heating facility are modelled through tetrahedral volume elements, with an element edge length of 8 mm and a fully integrated characteristic (Figure 92). Both, blank and tools are defined as rigid in the conducted SHT FEM model which means that the thermal expansion and distortion of the blank is neglected. The heat loss from blank to the ambient is modelled by using a convection boundary condition with an HTC of 5 W/m²K. The heat transfer between blank surface and tool is described through an HTC of 2400 W/m²K for a corresponding contact pressure of 0.6 MPa (6.3). For the heat loss from blank to the insulating unit an HTC of 30 W/m²K is assumed. Moreover, initial conditions are applied on the blank by setting the measured temperature of 50 °C, which is determined at the experiment shortly before contact between tool and sheet, has started as well as an initial tool temperature of 270°C. In order to model the heat transfer from the heating cartridges into the heating plate and heating cylinder a constant temperature of 270°C is applied to the surface of the hole where the heating cartridges are fixed. The thermal behaviour of tools and specimen is modelled through a thermal isotropic material model, which is defined through the same input parameter as in 10.2.1, except for the insulating unit. For the insulating multilayer textile, a heat capacity of 1800 J/kgK and a thermal conductivity of 0.06 W/mK is applied [146]. In order to speed up the simulation model, a thermal speed up factor of 10000 is used.

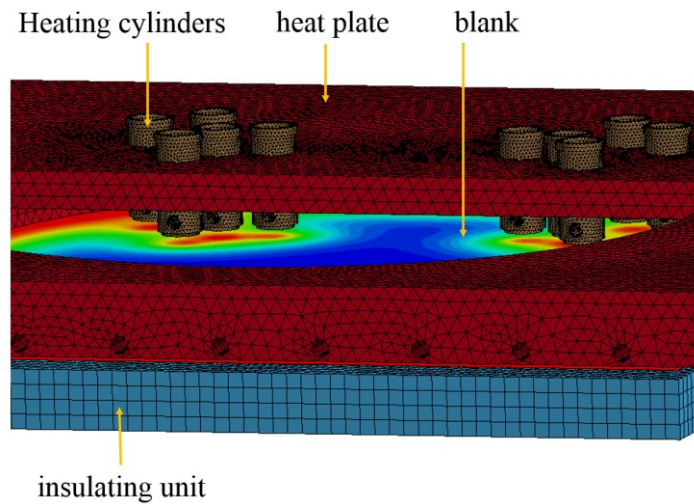


Figure 92 SHT simulation model

By modelling the forming process, the deep drawing tools are defined as rigid bodies, which means that elastic deformations of the forming tools are neglected (Figure 93-right). To model the blank, the Barlat1989 and Barlat-Yld2000-2d yield criterion as well as the mechanical and the thermo-mechanical coupled approaches are used in order to analyse their performance. Furthermore, a young's modulus of 73800 MPa and a poisson's ratio of 0.3 are set in the material model. For modelling the tribological characteristic between blank and tool surface a coefficient of friction (COF) of $\mu = 0.14$ is used [41,147]. To model the interaction between blank holder and die, a penalty contact formulation is implemented to describe the generated gap of 1.5 mm through using distance plates during forming. The gap is obtained by shifting the outer area of the blank holder for 1.5 mm in drawing direction (Figure 93-left). Additionally, a blank holder force of 180 kN is applied. To speed-up the forming simulation, a forming velocity of 5000 mm/s is used. The use of mass scaling in order to obtain faster calculation times has led to numerical errors.

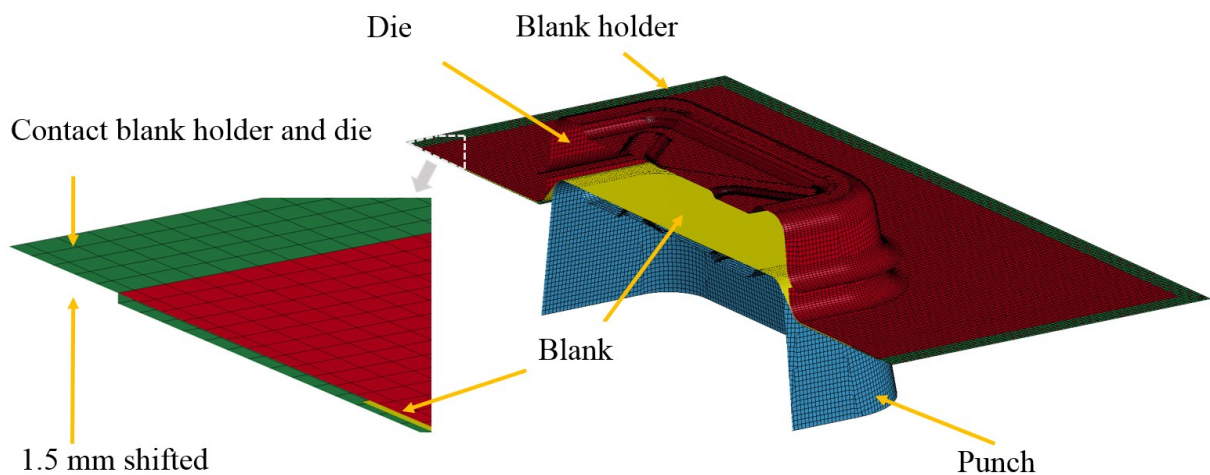


Figure 93 left: contact situation blank holder and die; right: sectional view - forming model

10.3.1 Validation and discussion of the simulation results

To validate the performance of the yield criterion Barlat1989 and Barlat-Yld2000-2d, for modelling the SHT and deep drawing process, the simulated and measured sheet thicknesses along the path marked in Figure 65 are compared. These results are shown in Figure 94 and are obtained through the simulated SHT layout X1. Thereby the simulation results calculated through the Barlat-Yld2000-2d yield criterion show a very accurate performance by comparing the simulation results to the experimental determined thickness. As expected, the simulation model conducted through the yield criterion Barlat1989 exhibits larger deviations to the obtained result in reality, compared to the sheet thickness distribution obtained using the yield criterion Barlat-Yld2000-2d. In particular in the area of the radius between flange and wall section, at position of 90 mm in Figure 94, a deviation of 0.025 mm to the measured sheet thickness of the drawn part occurs. In the critical zone of the part, which is located in the radius area between wall and bottom at a position of 175 mm a deviation of 0.012 mm, is observed.

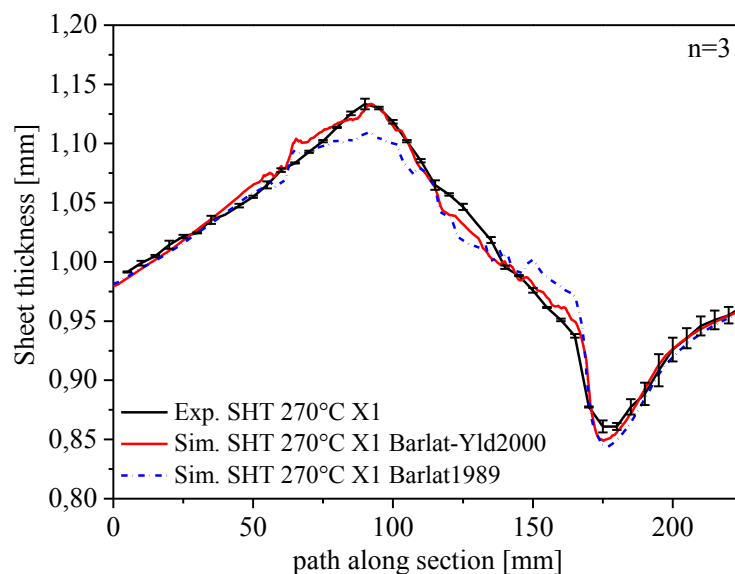


Figure 94 Validation of yield criterions by comparing the sheet thickness along a path of simulation and experiment (SHT conducted through SHT layout X1)

In the next evaluation step the SHT layout X2 is modeled and validated to analyze the performance of the simulation model for SHT layouts which exhibit a more complex design. The obtained results through the yield criterion Barlat1989 and Barlat-Yld2000-2d are plotted and compared to the measured sheet thickness in Figure 95. It is observed that a maximum variation of 0.01 mm occurs in the critical zone between simulation and the experimental determined sheet thickness, when the yield criterion Barlat-Yld2000-2d is used. For the simulation model described through Barlat1989, a maximum deviation of 0.022 mm in the radius area between flange and wall is detected. It is also observed that the Barlat-Yld2000-2d model shows a more accurate correlation in the area which is affected by the small SHT spots near the critical zone, compared to the simulation described through Barlat1989. Furthermore, it can be noticed that the sheet thickness distribution in the wall zone obtained by a simulation shows a more unsteady correlation to the measured sheet thickness, compared to the simulated results of SHT layout X1. This is explained by increased wrinkling in the wall zone due to the SHT spots located in the wall area and the pronounced heat transition zone when SHT layout X2 is conducted.

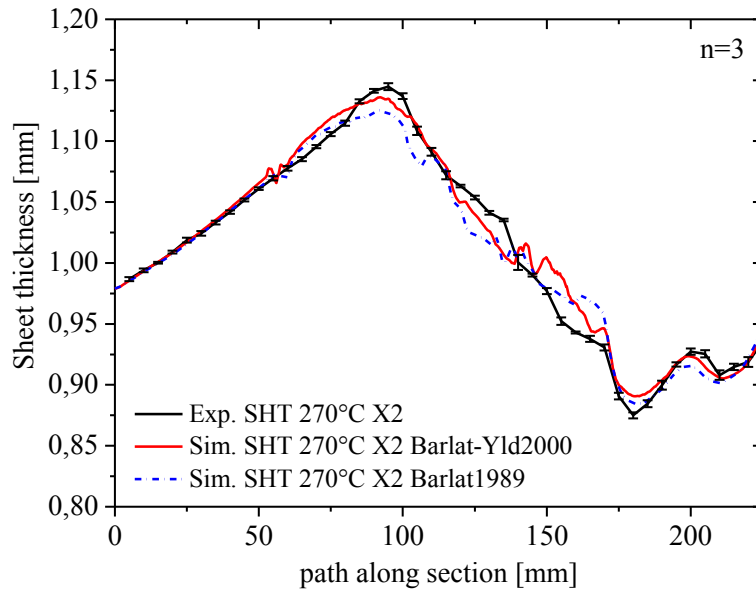


Figure 95 Validation of yield criterions by comparing the sheet thickness along a path of simulation and experiment (SHT conducted through SHT layout X2)

In practice, the forming limit diagram (2.11) is primarily used to predict the forming behaviour of sheet metals. To validate the obtained FLD through simulation, by using the yield criterion Barlat1989 and Barlat-Yld2000-2d, the simulated and measured major and minor strain in the area marked in Figure 65 is plotted in Figure 96. Thereby, the simulation described through the yield criterion Barlat-Yld2000-2d is in a favourable agreement with the measured major and minor strain distribution. By observing the simulation results calculated through the yield criterion Barlat1989, a higher variation to the experimentally determined strain distribution is observed.

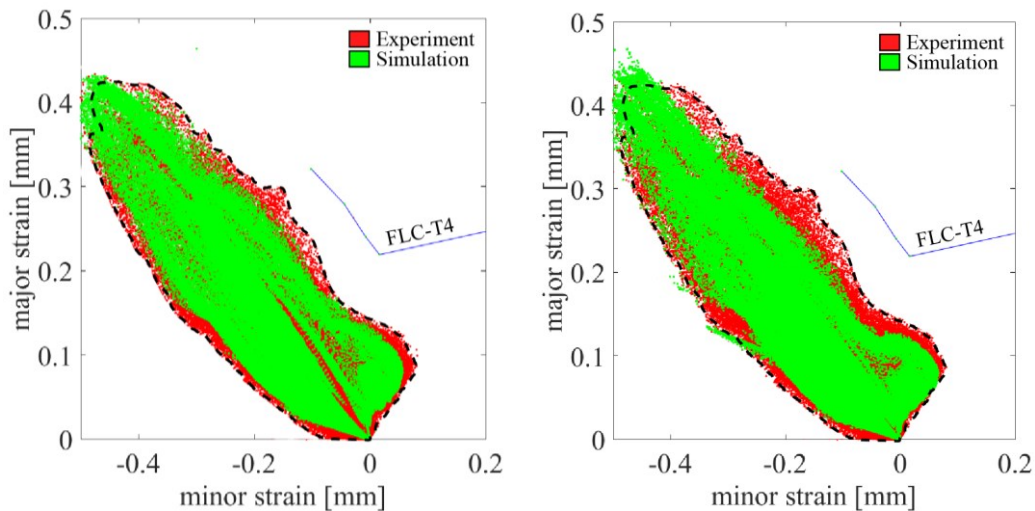


Figure 96 Validation of simulation and experiment (FLD): left: simulation modelled through Barlat-Yld2000-2d; right: simulation modelled through Barlat1989

For further validation the sheet thicknesses along a path are plotted in Figure 97 for evaluating the performance of the mechanical approach and the model described through the thermo-mechanical coupled

approach, to the measurement results obtained from the formed part in 8.3. To model the plastic material behaviour, the Barlat-Yld2000-2d yield criterion is used for both simulation models. Figure 97 clearly shows the effect of neglecting the heat transition zone by using the mechanical approach in the simulation model for the simulated SHT layout X2. In particular in the heat transition zone between the small SHT spots near the critical zone, at position 200 mm and 225 mm in Figure 97, a sudden change of the sheet thickness is observed. It is also noted that the simulation results differ in the area of the SHT spot located in the wall area, in particular where large wrinkling occurs (position of 150 mm on path in Figure 97). In the area of the radius between flange and wall (position of 90 mm on path in Figure 97) only small deviations occur, by using the mechanical approach, compared to the results of the simulation model described through the thermo-mechanical approach.

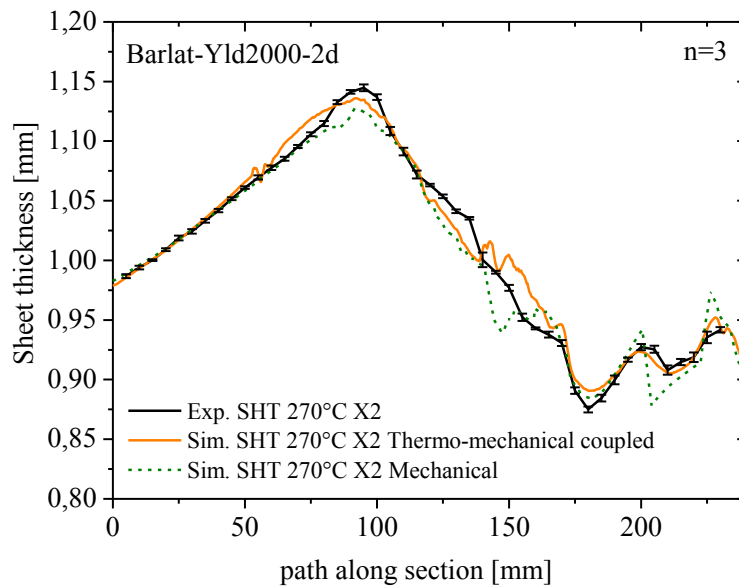


Figure 97 Validation of the mechanical and the thermo-mechanical coupled approach by comparing the sheet thickness along a path of simulation and experiment (SHT conducted through SHT layout X2)

In Figure 98, the error between simulated and measured sheet thickness is visually illustrated. The sheet thickness distribution in the area shown in Figure 65 is determined by the optical analysis ARGUS (4.5.1). After measuring the sheet thickness of the formed part, the error of the simulated sheet thickness is determined through the software provided by GOM-ARGUS, and plotted on the sheet surface (Figure 98). In Figure 98-right the deviation of the simulation results can be clearly seen. They are obtained through the mechanical approach, and occur particularly in the heat transition zone of the small SHT spots. These deviations are definitely caused by neglecting the heat transition zone, as illustrated in Figure 98-right, by using the mechanical approach. Contrary to these results, the simulated sheet thickness, using the thermo-mechanical coupled approach, shows no recognizable deviations in the bottom area where the material is modified through the SHT spots (Figure 98-left). It is also noted that both simulation results shown in Figure 98 exhibit large deviations in the wall area where wrinkles occur.

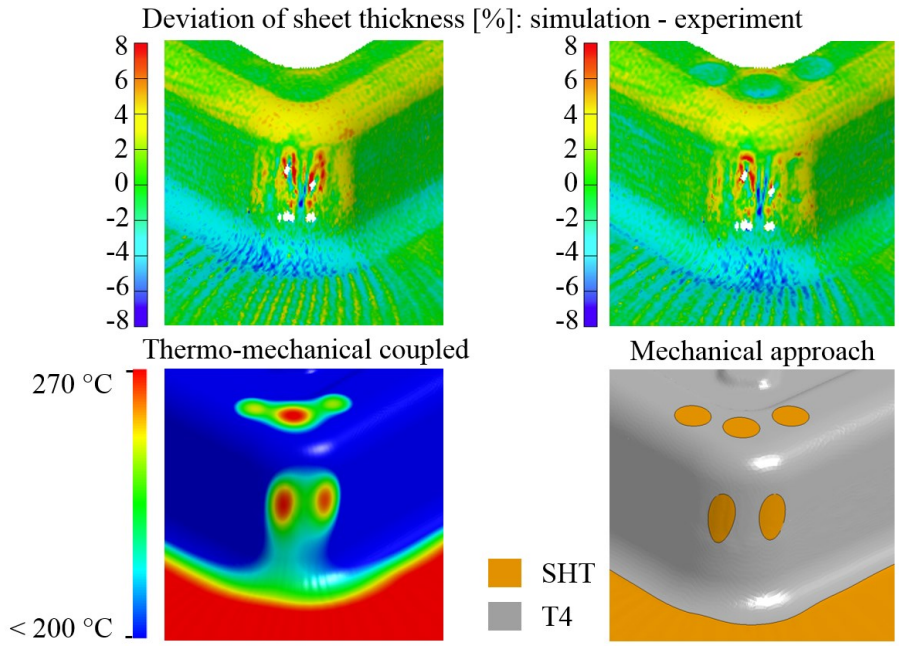


Figure 98 Error between simulated and measured sheet thickness: left: thermo-mechanical coupled approach; right: mechanical approach

Figure 99 shows the prediction of the forming limit through the FLD, which is determined by using the mechanical approach and the thermo-mechanical coupled approach in the simulation model. Thereby, Figure 99-right shows substantial deviations to the measured strain values in direction of the strain combination deep drawing ($\phi_1 = -\phi_2$ explained in Figure 24), when the mechanical approach is conducted. These deviations occur in the area of the SHT spots located in the wall zone, at a level of major strain higher than 0.4 (Figure 98-right). Except these variances the simulation results obtained through the mechanical approach are in a reasonable agreement with the experiment.

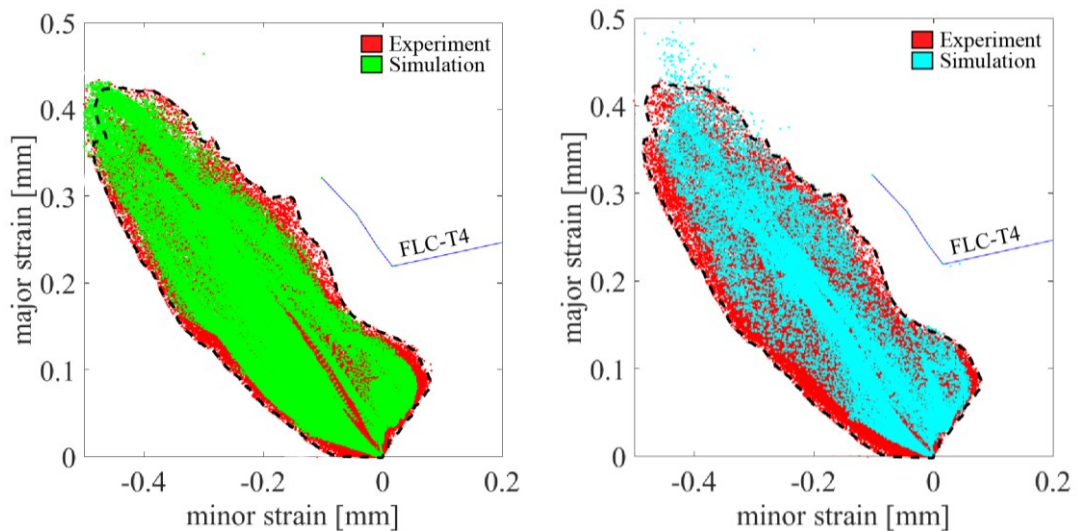


Figure 99 Validation of simulation and experiment (FLD): left: simulation modelled through thermo-mechanical coupled approach; right: simulation modelled through mechanical approach

For a conclusive evaluation of the simulation model, the predicted formability of the untreated blank (T4 state) and of THTB, conducted through SHT layout X2, is illustrated in Figure 100. By comparing Figure 100 with Figure 66-right, it is evident that a similar crack formation at a drawing depth of circa 70 mm occurs when no SHT is executed before forming. Figure 100 also shows the manufactured part without the occurrence of cracks when SHT layout X2 is used in the process.

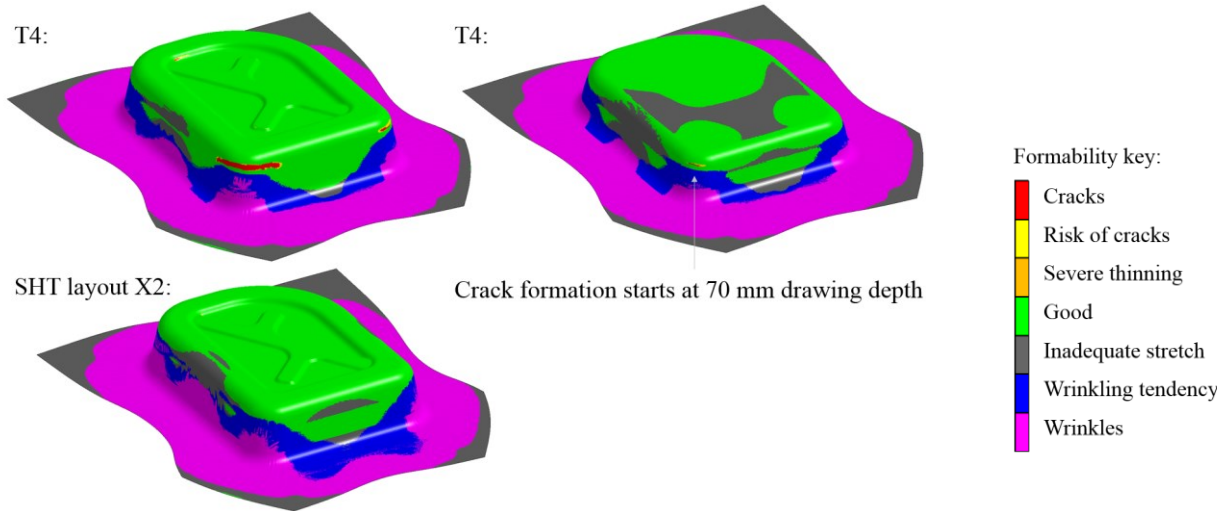


Figure 100 Formability simulation AA6016 T4 and THTB (SHT layout X2)

10.4 Summarizing evaluation of the analysed simulation model

In brief, by evaluating the performance of the conducted simulations presented in this chapter, it can be concluded that a higher effort to characterize the AA6016 material for the Barlat-YLD2000-2d results in a better agreement between simulation and the conducted SHT and forming process in chapter 8.3.

The thermo-mechanical approach exhibits a highly accurate description of the SHT and forming process, particularly in the area where a pronounced heat transition zone occurs. However, by only using a mechanical approach to model THTB of AA6016 alloys, adequate results can also be obtained. Concluding the investigation in chapter 10, it can be recommended to use the mechanical approach in the first stage of the virtual development in order to find the optimal SHT layout. This is justified due to a much lower modelling effort and computing time, which enables more iterative steps to find the required SHT layout. In the final stage, the use of the thermo-mechanical coupled approach is suggested to be able to exclude material failure in the heat transition zone.

11 Summary and Outlook

Tailored heat treated blanks (THTB) is a method with the capability to enhance the forming performance of sheet metals. Tailored properties of Al-Mg-Si alloys can be produced through a short-term heat treatment (SHT), which reduces the strength of the material due to a partial or complete dissolution of the coherent distributed MgSi-clusters in the material's micro structure. The SHT procedure for the material AA6016 T4 (Superlite 220 ST) was investigated within this thesis, aiming to determine the optimal SHT process parameter, in order to obtain an optimal improvement of drawability, and an optimal hardening performance during paint baking. Furthermore, the interacting effects caused through the SHT and the paint baking process on the mechanical properties were analysed. Apart from experimental investigations of the SHT process and its effect on the forming performance, also a simulation model was built, which describes the investigated manufacturing method virtually by using the FEM solver LsDyna. Different modelling approaches were used, as well as different material models, to achieve this aim. Therefore, the effect of these models on the simulation results is analysed and evaluated through experimentally determined data.

Within this work, tensile tests were performed, using a quenching- and deformation dilatometer to characterize the AA6016 (Superlite 220 ST) material and to simulate the SHT and paint baking process. Out of these tests the optimal SHT temperature of 270 °C, which influences the paint baking process beneficially in terms of an enhanced hardening performance, was determined. These findings do not correlate with investigations found in literature, conducted for the material AA6016PX (AC140) and AA6181PX. Hence, this research result underlines the high influence of divergences in the alloy's composition on the optimal SHT process parameters. Further investigations within this thesis have determined that the most efficient hardening through paint baking is obtained by executing the artificial aging procedure shortly after the SHT. The influence of storage times between SHT and paint baking, in a time frame of 4 weeks, on the properties of strength and ductility were analysed. It was also found that in the period of 1 week, the largest amount of strength is regained due to natural aging when SHT is performed through 270 °C temperature on the AA6016 material (Superlite 220 ST).

The beneficial impact of the SHT, with an optimal temperature of 270 °C, on the mechanical properties was also proved by characterizing a drawn part manufactured through a multi stage forming process. Measurement results showed that zones which exhibit insufficient strengthening can compensate their poor hardening characteristic through an enhanced artificial aging behaviour, when SHT is conducted with a temperature of 270 °C. Also, an improvement of ductility was measured in two spots on the formed part, contrary to the remaining areas of the part. A scientific explanation of this opposing behaviour was not obtained within this work.

A conduction heating facility was developed within this thesis to evaluate different SHT process parameters in regard to their influence on the subsequently forming process. This heating tool is designed to enable fast heating rates, definable holding times and temperatures, as well as the ability to use different SHT layout combinations. For the validation procedure, a forming tool was manufactured and designed which exhibits similar design elements to a spare wheel recess part used for industrial applications.

Through these facilities, the process parameter holding time was analysed for a time range of 0 s to 10 s. Thereby, a slight reduction of the drawing performance was observed when a holding time of 10 s was performed compared to shorter holding times.

Contrary to the process parameter holding time, considerable influences on the drawability were detected for conducted storage times higher than 16 hours, between the SHT procedure and the forming process due to natural aging. To that issue, the effect of storage times, in a time frame of 1 week on the drawing performance were analysed. Minor deviations were measured between conducted storage times of 100 hours and 164 hours.

Also, different designs of the SHT layout were performed and evaluated through the forming limit diagram. Thereby, it was observed that the lowered resistance against necking of SHT treated areas, due to an SHT temperature of 270 °C, leads to a less robust forming process. Therefore, the SHT conducted in the flange area is recommended in order to ensure a more robust forming behaviour, if zones are modified through SHT outside of the flange area. An enhanced SHT layout, which exhibits tailored zones in the flange section and near to the critical zones, showed considerable decrease of critical thinning.

The forming results of a multi stage forming process have pointed out that an optimal SHT layout, tailored to the first forming step, does not consequently lead to optimal drawing properties in the second forming stage. This emphasises the importance of the virtual development of the SHT layout.

By investigating the tribological performance of the applied dry film lubricant Fuchs PL39SX, a poor resistance against SHT temperatures was determined. Out of this investigation, when the dry film lubricant remains on the blank surface during the SHT procedure, it causes a decreasing drawing performance for applied SHT temperatures higher than 240 °C. Therefore, to remove the lubricant before the SHT is performed is absolutely essential for a successful performance of the SHT process.

The SHT process and the subsequently forming process conducted within this thesis were modelled through a mechanical and thermo-mechanical coupled approach. Using the thermo-mechanical coupled approach, which exhibits more effort in material characterization and modelling than the mechanical approach, led to a good simulation performance, particularly in areas where a heat transition zone occurs. However, the simulation results obtained through the mechanical approach were in an adequate agreement with the real forming process. Hence, it is concluded that the use of the mechanical modelling approach is more efficient in order to find the optimal design of the SHT layout, due to significantly lower modelling effort and computing time, which enables the possibility of more iterative design steps. For the final evaluation step, the thermo-mechanical coupled modelling approach is suggested to be able to predict material failure caused in the heat transition zone. The validation results of the material models Barlat1989 and Barlat-Yld2000-2d showed recognizable deviations in their performance. Therefore, the Barlat-Yld2000-2d is recommended for describing the plastic behaviour of the AA6016 material and for modelling the SHT and forming process.

The gathered knowledge within this thesis provides useful guidance for implementing the method of THTB, conducted through a short-term heat treatment before forming, in a manufacturing process for industrial application. The determined material data and the modelled simulation models in LsDyna showed a good performance and could be used in the virtual design process of THTB.

References

- [1] U.S. EPA, OA, Global Greenhouse Gas Emissions Data, available at <https://www.epa.gov/ghgemissions/global-greenhouse-gas-emissions-data> (accessed on December 5, 2016).
- [2] IPCC, Fifth Assessment Report - Mitigation of Climate Change, available at <https://www.ipcc.ch/report/ar5/wg3/> (accessed on December 5, 2016).
- [3] W. Ruch, Die Strategische Bedeutung der Al-Technologie im Karosserieleichtbau bei AUDI, in: 2nd European Al-Automobile Conference, Bad Nauheim, 2002.
- [4] H.E. Friedrich (Ed.), Leichtbau in der Fahrzeugtechnik, 2nd ed., Springer Fachmedien Wiesbaden GmbH, Wiesbaden, 2016.
- [5] G.S. Cole, A.M. Sherman, Light weight materials for automotive applications, *Materials Characterization* 35 (1) (1995) 3–9.
- [6] VDI-Gesellschaft Materials Engineering, Studie der Werkstoffinnovationen für nachhaltige Mobilität und Energieversorgung, Düsseldorf, 2014.
- [7] Drucker Worldwide, The road ahead - automotive materials, available at www.ducker.com.
- [8] N. Lutsey, Review of technical literature and trends related to automobile mass-reduction technology, Davis, 2010.
- [9] A. M. Sherman, A. R. Krause, P. A. Friedman, D. A. Steenkamer, D. Q. Housten, Automotive Body Materials, in: *Encyclopedia of Materials, Science and Technology*, 2006, pp. 415–421.
- [10] A. Lakeit, Die Karosserie der Zukunft im Spannungsfeld der Anforderungen, in: *Neue Wege zum wirtschaftlichen Leichtbau, Innovative Lösungen zur Blechumformung und mechanischen Fügetechnik*, 27th ed., 2007, pp. 15–22.
- [11] W. Miller, L. Zhuang, J. Bottema, A. Wittebrood, P. de Smet, A. Haszler, A. Viergge, Recent development in aluminum alloys for the automotive industry, *Materials Science and Engineering: A* 280 (1) (2000) 37–49.
- [12] E. Mayr, Mit Fusion öffnen wir die Tür für Aluminium noch weiter, in: *Werkstoffe im Automobilbau*, 2007, pp. 26–28.
- [13] J. Hirsch, Aluminium in Innovative Light-Weight Car Design, *MATERIALS TRANSACTIONS* 52 (5) (2011) 818–824.
- [14] AUDI, 2017-audi-q7-body-external - Google-Suche, available at https://www.google.at/search?q=audi+q7+external&biw=1280&bih=934&site=webhp&source=lnms&tbm=isch&sa=X&ved=0ahUKEwiU6Lbp5uHQAhVrDcAKHRqnCLsQ_AUIBigB#tbm=isch&q=2017-audi-q7-body-external&imgc=A05S9hsjV6ocMM%3A (accessed on December 7, 2016).
- [15] G. Charca Ramos, M. Stout, R.E. Bolmaro, J.W. Signorelli, P. Turner, Study of a drawing-quality sheet steel. I: Stress/strain behaviors and Lankford coefficients by experiments and micromechanical simulations, *International Journal of Solids and Structures* 47 (17) (2010) 2285–2293.
- [16] K. Siegert (Ed.), Neuere Entwicklung in der Blechumformung, Werkstoff-Informationsgesellschaft.

References

- [17] H.E. Theis, Handbook of Metalforming Processes, Taylor & Francis, 1999.
- [18] P. Furrer, M. Bloeck, Aushärtbare Aluminiumlegierungen für den Karosseriebau, in: Neuere Entwicklung in der Blechumformung, Fellbach, Werkstoff-Informationsgesellschaft, pp. 385–402.
- [19] J. Meinhardt, W. Wohnig, F. Fischer, Umformbarkeit von neuartigen Karosseriewerkstoffen, in: Bleche Rohre Profile 42, 1995, pp. 758–767.
- [20] F. Vollertsen, K. Lange, Enhancement of Drawability by Local Heat Treatment, CIRP Annals - Manufacturing Technology 47 (1) (1998) 181–184.
- [21] H.-H. Braess (Ed.), Vieweg Handbuch Kraftfahrzeugtechnik: Mit 69 Tabellen, 3rd ed., Vieweg, Wiesbaden, 2003.
- [22] S. Ahmadi, A.R. Eivani, A. Akbarzadeh, An experimental and theoretical study on the prediction of forming limit diagrams using new BBC yield criteria and M–K analysis, Computational Materials Science 44 (4) (2009) 1272–1280.
- [23] C. Kammer, Aluminium-Taschenbuch, 16th ed., Beuth, Berlin, 2012.
- [24] Stangen, Rohre, Profile, Drähte, Vormaterial, 2nd ed., Beuth, Berlin [u.a.], 2009.
- [25] A. Birkert, S. Haage, M. Straub, Umformtechnische Herstellung komplexer Karosserieteile: Auslegung von Ziehanlagen, Springer Berlin Heidelberg, Berlin, Heidelberg, 2013.
- [26] W. König, F. Klocke, Fertigungsverfahren: Blechbearbeitung Düsseldorf, 5th ed., VDI Verlag, 1995.
- [27] DIN 8584-1, 2003-09 Fertigungsverfahren Zugdruckumformen - Teil 1: Allgemeines; Einordnung, Unterteilung, Begriffe.
- [28] Schuler GmbH, Handbuch der Umformtechnik, Springer, Berlin, 1996.
- [29] E. Doege, B.-A. Behrens, Handbuch Umformtechnik: Grundlagen, Technologien, Maschinen, Springer-Verlag Berlin Heidelberg, Berlin Heidelberg, 2010.
- [30] M. Klamsner, Ziehen von Blechformteilen auf einfachwirkenden Pressen mit hydraulischer Zieheinrichtung im Pressentisch. Zugl.: Stuttgart, Univ., Diss., 1994, DGM-Informationsges, Oberursel, 1994.
- [31] K. Lange, Umformtechnik Handbuch für Industrie und Wissenschaft: Band 2: Massivumformung, Springer Berlin Heidelberg, Berlin, Heidelberg, s.l., 1988.
- [32] F. Dinkel, Umformbarkeit von Aluminium-Karosserieblechen mit neuartigen Oberflächen. Zugl.: München, Techn. Univ., Diss., 1997, Hieronymus, München, 1997.
- [33] K. Siegert and S. Wagner, Formability Characteristics of Aluminum Sheet, 1994.
- [34] K. Siegert, Hydromechanical deep drawing of auto body components, in: ALUMINUM - International Journal, 80. Jahrgang, Verlag Giesel Verlag GmbH, Hannover, 2004, pp. 20–24.
- [35] A. Mertens, Tailored Blanks: Stahlprodukte für den Fahrzeug-Leichtbau, Verl. Moderne Industrie, München, 2003.
- [36] M. Meiler, M. Pfestorf, M. Geiger, M. Merklein, The use of dry film lubricants in aluminum sheet metal forming, Wear 255 (7-12) (2003) 1455–1462.

References

- [37] L. Ju, T. Mao, J. Malpica, T. Altan, Evaluation of Lubricants for Stamping of Al 5182-O Aluminum Sheet Using Cup Drawing Test, *J. Manuf. Sci. Eng* 137 (5) (2015) 51010.
- [38] F. Ostermann, *Anwendungstechnologie Aluminium*, 2nd ed., Springer-Verlag Berlin Heidelberg, Berlin Heidelberg, 2007.
- [39] AIP Conference Proceedings, AIP, 2004.
- [40] S. Wagner, 3D-Beschreibung der Oberflächenstrukturen von Feinblechen. Zugl.: Stuttgart, Univ., Diss., 1996, DGM-Informationsges. Verl., Oberursel, 1996.
- [41] N. Bay, T. Nakamura, S. Schmid, Green Lubricants for Metal Forming, in: *Tribology of manufacturing processes: Proceedings of the 4th International Conference on Tribology in Manufacturing Processes, (ICTMP 2010)*; Nice, France, June 13th - 15th, 2010, Presses des Mines, Paris, 2010, pp. 5–28.
- [42] K. Hyunok, T. Altan, Evaluating dry film lubricants for automotive applications Part I, 2006, available at <http://www.thefabricator.com/article/stamping/evaluating-dry-film-lubricants-for-automotive-applications-part-i>.
- [43] M. Merklein, M. Johannes, M. Lechner, A. Kuppert, A review on tailored blanks-Production, applications and evaluation, *Journal of Materials Processing Technology* 214 (2) (2014) 151–164.
- [44] F. Vollertsen, Tailored Blanks, in: *Bleche Rohre Profile* 42, 1995, pp. 172–178.
- [45] E. Knabe, Ziehen von Blechformteilen aus zusammengeschnittenen Platinen unterschiedlicher Blechdicke und Güte ("tailored blanks"), *Werkstoff-Informationsges*, Oberursel i.e. Frankfurt (Main), 1997.
- [46] K. Lamprecht, M. Merklein, Characterisation of mechanical properties of laser welded tailored and patchwork blanks, in: *Proceedings of the 4th International Conference on Laser Assisted Net Shape Engineering (LANE2004)*, pp. 349–358.
- [47] H. Kleinert, S. Bräunling, I. Jansen, R. Häßler, F. Liebrecht, Patchworkkleben - partielle Verstärkung von Blechbauteilen für Fahrzeuge, in: *Internationale Fachtagung Swiss Bonding*, 2003, pp. 142–154.
- [48] R. Kopp, P. Böhlke, A New Rolling Process for Strips with a Defined Cross Section, *CIRP Annals - Manufacturing Technology* 52 (1) (2003) 197–200.
- [49] R. Kopp, C. Wiedner, A. Meyer, Flexibly Rolled Sheet Metal and Its Use in Sheet Metal Forming, *AMR* 6-8 (2005) 81–92.
- [50] U. Vogt and M. Merklein, Design principles of tailored heat treated blanks for the manufacturing of complex car body parts, in: *Conference Best in Class Stamping*, June 16 - 18, 2008, Olofström, Schweden, Olofström, 2008, pp. 557–568.
- [51] E. Siebel, H. Beisswänger, Ziehversuche mit hartgewalzten und partiell geglühten Ronden zur Erhöhung des Ziehverhältnisses, in: *Mitteilungen für die Mitglieder der Forschungsgesellschaft Blechverarbeitung*, Düsseldorf, 1953, pp. 89–93.

References

- [52] M. Hogg, Herstellung und Umformung lokal wärmebehandelter Platinen. Zugl.: Stuttgart, Univ., Diss., 2006, MAT-INFO DGM Informationsges, Frankfurt Main, 2006.
- [53] K. Siefert, M. Merklein, A. Nester, M. Grünbaum, Intermediate Heat Treatment – A New Proceeding for Aluminum Alloys Using Forming Limit Diagrams, in: Key Engineering Materials, 2011, pp. 428–435.
- [54] A.R. Hofmann, Erweiterung von Formgebungsgrenzen beim Umformen von Aluminiumwerkstoffen durch den Einsatz prozessangepasster Platinen. Zugl.: Erlangen-Nürnberg, Univ., Diss., 2002, Meisenbach, Bamberg, 2002.
- [55] C. Haase, H. Wurst, Zur Frage der Kalt- und Warmaushärtung bei Aluminium-Magnesium Silizium-Legierungen, in: Metallkunde 33, 1941, pp. 399–403.
- [56] U. Vogt, Seriennahe Auslegung von Aluminum Tailored Heat Treated Blanks. Univ., Diss.–Erlangen-Nürnberg, 2009, Meisenbach, Bamberg, 2009.
- [57] K. Lange (Ed.), Umformtechnik Handbuch für Industrie und Wissenschaft, Band 3, 2nd ed., Springer, Berlin [u.a.], 1990.
- [58] S. Keller, E. Brünger, D. Wieser, Aluminiumwerkstoffe für den Fahrzeugbau. Firmenschrift der Hydro Aluminium Deutschland GmbH, 2006.
- [59] J. Hirsch, Aktuelle und zukünftige Einsatzpotentiale von Aluminium und Magnesium, in: Vision of Materials and processes for Future Generations of Automobiles, Berlin, 2002, pp. 26–27.
- [60] G.E. Dieter, Mechanical metallurgy, 3rd ed., McGraw-Hill, New York NY u.a., 1986.
- [61] C. Henkel, P. J. Uggowitzer, Recent results to the integration of artificial aging into paint baking process, in: Internationaler Expertenkreis Al-Umformung, Bad Nauheim, 2001, pp. 279–287.
- [62] D. Altenpohl, Aluminium von innen betrachtet: Eine Einführung in die Metallkunde der Aluminiumverarbeitung, 3rd ed., Aluminium-Verl., Düsseldorf, 1972.
- [63] R. Vissers, M.A. van Huis, J. Jansen, H.W. Zandbergen, C.D. Marioara, S.J. Andersen, The crystal structure of the β' phase in Al–Mg–Si alloys, Acta Materialia 55 (11) (2007) 3815–3823.
- [64] K. Vieregge, J. Hirsch, Metallurgie und Technologie der Aluminium-Werkstoffe. DGM, Bonn.
- [65] J.E. Hatch, A. Association, A.S.f. Metals, Aluminum: Properties and physical metallurgy, 1984.
- [66] C.Haase, H.Wurst, Zur Frage der Kalt- und Warmaushärtung bei Aluminium-Magnesium-Silizium-Legierungen. Z. Metallkunde 33 (1941) S. 399–403.
- [67] S. Pogatscher, H. Antrekowitsch, H. Leitner, T. Ebner, P.J. Uggowitzer, Mechanisms controlling the artificial aging of Al–Mg–Si Alloys, Acta Materialia 59 (9) (2011) 3352–3363.
- [68] H.Uchida, H.Yoshida, Improvement in paint bake response of an Al-Mg-Si alloy by reversion. Conference on Aluminum and Magnesium for Automotive Applications, Cleveland, Ohio, 29. Oct.-2. Nov. 1995, The Minerals, Metals and Materials Society, 1996, pp. 97–104.

References

- [69] Mitsubishi Aluminum Co: Reversion treatment for aluminum alloy sheet naturally age hardened by air cooling after solution hardening treatment. Japan: Patent JP 5044000, 1993.
- [70] F.-J. Dirks, Tiefziehen vorverfestigter und partiell geglühter Ronden aus Aluminium und Aluminiumlegierungen. Dissertation, Technische Universität Berlin, 1971.
- [71] M. Kerausch, Simulationsgestützte Prozessauslegung für das Umformen lokal wärmebehandelter Aluminiumplatten. Univ., Diss.--Erlangen-Nürnberg, 2007, Meisenbach, Bamberg, 2007.
- [72] M. Geiger, M. Merklein, Microstructural Investigation of Aluminum Tailored Heat Treated Blanks, in: Annals of the German Academic Society for Production Engineering WGP, 2004, pp. 47–50.
- [73] D. Staud, Effiziente Prozesskettenauslegung für das Umformen lokal wärmebehandelter und geschweißter Aluminiumbleche. Dissertation, Technischen Fakultät der Universität Erlangen-Nürnberg, 2009.
- [74] M. Geiger, M. Merklein, U. Vogt, Aluminum tailored heat treated blanks, Prod. Eng. Res. Devel. 3 (4-5) (2009) 401–410.
- [75] Sumitomo Light Metal Ind.: Production of aluminum alloy material for forming excellence in hardenability of coating/baking, Formability and shape freezability. Japan: Patent JP 5279822, 1993.
- [76] M. Geiger, M. Merklein, M. Kerausch, Finite Element Simulation of Deep Drawing of Tailored Heat Treated Blanks, CIRP Annals - Manufacturing Technology 53 (1) (2004) 223–226.
- [77] Konzernnorm TL 100 Volkswagen AG, 2003.
- [78] M. Meiler, Grossserientauglichkeit trockenschmierstoffbeschichteter Aluminiumbleche im Presswerk: Grundlegende Untersuchungen zur Tribologie, zum Umformverhalten und Bauteilversuche, Meisenbach, Bamberg, 2005.
- [79] J. Christlein, L. Schüler, Audi Space Frame 2. Generations: Realisierung eines zukunftsweisenden Leichtbau-Karosseriekonzepts mit Hilfe der Simulation. In: Verein der Deutschen Ingenieure (Hrsg.): VDI-Berichte 1543: Entwicklung im Karosseriebau. Düsseldorf: VDI-Verlag, 2000, pp. 107-119.
- [80] A. E. Tekkaya, A. Brosius, Simulation in der Umformtechnik: Das Werkzeug für Innovationen. In: Kawalla, R. (Hrsg.): 14. Sächsische Fachtagung Umformtechnik, 04.-05.12.2007, Freiberg: TU Bergakademie Freiberg, 2007, pp. 113-126.
- [81] K. Roll, T. Altan, E. Tekkaya, M. Herrmann, Virtuelle Umformtechnik. In: Geiger, M. (Hrsg.): Umformtechnik 2000 Plus. Bamberg: Meisenbach, 1999, pp. 255-274.
- [82] K. Roll, Simulation of Sheet Metal Forming – Necessary Developments In The Future, in: P. Hora (Ed.), Numisheet 2008: September 1 - 5, 2008, Interlaken, Switzerland, ETH Zurich Inst. of Virtual Manufacturing, Zurich, pp. 3–10.
- [83] T. Heller, G. Deinzer, G. Steinbeck, Verkürzung der Markteinführung neuer Stähle durch Definition eines Werkstofffreigabeprozesses. In:

References

- Forschungsvereinigung Stahlanwendung e. V. (Hrsg.): 7. Stahl-Symposium - Werkstoffe, Anwendung, Forschung. Simulation als Werkzeug zur Verarbeitung von Stahlfeinblech. 25.04.2007, Düsseldorf.
- [84] Abaqus, available at <http://www.3ds.com/products-services/simulia/products/abaqus/> (accessed on December 29, 2016).
- [85] MSC Software Corporation | Simulating Reality, Delivering Certainty, available at <http://www.mssoftware.com/de> (accessed on December 29, 2016).
- [86] PAM-STAMP - Stamping Simulation Solution, available at <https://www.esi-group.com/software-solutions/virtual-manufacturing/sheet-metal-forming/pam-stamp-stamping-simulation-solution> (accessed on December 29, 2016).
- [87] LS-DYNA | Livermore Software Technology Corp., available at <http://www.lstc.com/products/ls-dyna> (accessed on December 29, 2016).
- [88] AutoForm Engineering GmbH, Softwarelösungen für die Blechumformung | AutoForm Engineering, available at <http://www.autoform.com/de/> (accessed on December 29, 2016).
- [89] H. Gese, S. Keller, V. Yeliseyev, H. Dell, Ermittlung von Fließwiderstandskurven bei großen Formänderungen für die Blechumformsimulation, in: H. Frenz (Ed.), Kennwertermittlung für die Praxis: 20. Tagung Werkstoffprüfung, Wiley-VCH, Weinheim, 2007, pp. 242–249.
- [90] P. Hora, U. Feurer, A. Wahlen, J. Reissner, Methods for handling of FEM input and output data with the goal of higher computational reliability. In: Proceedings of the European Congress on Computational Methods in Applied Sciences and Engineering Engineering Publications, 2000, 1-19.
- [91] P. Ludwik, Elemente der Technologischen Mechanik. Springer: Berlin, Germany, 1909.
- [92] H.W. Swift, Plastic instability under plane stress, *Journal of the Mechanics and Physics of Solids* 1 (1) (1952) 1–18.
- [93] A. Gosh, A physically-based constitutive model for metal deformation. *Acta Metall* 28 (1980), pp. 1443–1465.
- [94] E. Voce, The relationship between stress and strain for homogeneous deformation. *J. Inst. Met.* 1948, 74, 537–562.
- [95] J.E. Hockett, O.D. Sherby, Large strain deformation of polycrystalline metals at low homologous temperatures, *Journal of the Mechanics and Physics of Solids* 23 (2) (1975) 87–98.
- [96] P.F. Bariani, T. Dal Negro, S. Bruschi, Testing and Modelling of Material Response to Deformation in Bulk Metal Forming, *CIRP Annals - Manufacturing Technology* 53 (2) (2004) 573–595.
- [97] K. Roll, Tendencies and New Requirements in the Simulation of Sheet Metal Forming Processes. In: Umformtechnik im Wandel der Zeit e. V. (Hrsg.): Kolloquium - Umformtechnik im Wandel der Zeit, pp. 105-131.
- [98] V. Goedel, M. Merklein, Variation of deep drawing steel grades' properties in dependency of the stress state and its impact on FEA, *Int J Mater Form* 4 (2) (2011) 183–192.

References

- [99] L. Kessler, H. Richter, K. Roll and A. Faust, A contribution on yield loci modeling compared to the application of variable hardening curves in forming simulations, in: May 21 - 23, 2008, Miskolc, Ungarn, Miskolc, 2007, pp. 101–107.
- [100] L. Lăzărescu, I. Nicodim, I. Ciobanu, D.S. Comșa, D. Banabic, Determination of material parameters of sheet metals using the hydraulic bulge test, *Acta Metall. Slovaca* 19 (1) (2013).
- [101] L. Lăzărescu, I. Ciobanu, I.P. Nicodim, D.S. Comșa, D. Banabic, Effect of the Mechanical Parameters Used as Input Data in the Yield Criteria on the Accuracy of the Finite Element Simulation of Sheet Metal Forming Processes, *KEM 554-557* (2013) 204–209.
- [102] P. Hora, M. Gorji, B. Berisha, Modelling of fracture effects in the sheet metal forming based on an extended FLC evaluation method in combination with fracture criterions, *IOP Conf. Ser.: Mater. Sci. Eng.* 159 (2016) 12030.
- [103] N. Hung, M. Marion, Improved Formability of Aluminum Alloys using Laser Induced Hardening of Tailored Heat Treated Blanks, *Physics Procedia* 39 (2012) 318–326.
- [104] A. Werber, M. Liewald, W. Nester, M. Grünbaum, K. Wiegand, J. Simon, J. Timm, W. Hotz, Assessment of forming limit stress curves as failure criterion for non-proportional forming processes, *Prod. Eng. Res. Devel.* 7 (2-3) (2013) 213–221.
- [105] D. Banabic, *Sheet metal forming processes: Constitutive modelling and numerical simulation*, Springer, Berlin, 2010.
- [106] R. Hill, A Theory of the Yielding and Plastic Flow of Anisotropic Metals, *Proceedings of the Royal Society A: Mathematical, Physical and Engineering Sciences* 193 (1033) (1948) 281–297.
- [107] K. Mattiasson, L. Nilsson, FE-simulations - possibilities and limitations Today and tomorrow. In: Nasder Asnafi (Hrsg.): *Proceedings of the IDDRG 2008*, 16.-18.06.2008, Olofström, Schweden.
- [108] J. Woodthorpe, R. Pearce, The anomalous behaviour of aluminum sheet under balanced biaxial tension, *International Journal of Mechanical Sciences* 12 (4) (1970) 341–347.
- [109] H. Aretz, Modellierung des anisotropen Materialverhaltens von Blechen mit Hilfe der Finite-Elemente-Methode. In: Hirt, G; Raabe, D; Kopp, R. (Hrsg.): *Umformtechnische Schriften*, Bd. 106, Aachen / Düsseldorf: Shaker, 2003.
- [110] D. Banabic, H.-J. Bunge, K. Pöhlandt, A.E. Tekkaya (Eds.), *Formability of Metallic Materials: Plastic Anisotropy, Formability Testing, Forming Limits*, Springer, Berlin, Heidelberg, 2000.
- [111] F. Barlat, D. J. Lege, J. C. Brem, A six-component yield function for anisotropic materials. *Int. J. Plasticity* 7 (1991), 693–712.
- [112] F. Barlat, R.C Becker, Y. Hayashida, Y. Maeda, M. Yanagawa, K. Chung, J. C. Brem, D. J. Lege, K. Matsui, S. J. Murtha, S. Hattori, Yielding description for solution strengthened aluminum alloys. *Int. J. Plasticity* 13 (1997a), 385–401.

References

- [113] F. Barlat, Y. Maeda, K. Chung, M. Yanagawa, J. C. Brem, Y. Hayashida, D. J. Lege, K. Matsui, S. J. Murtha, S. Hattori, R. C. Becker, S. Makosey, Yield function development for aluminum alloy sheets. *J. Mech. Phys. Solids* 45 (1997b), 1727–1763.
- [114] F. Barlat, J.C. Brem, J.W. Yoon, K. Chung, R.E. Dick, D.J. Lege, F. Pourboghrat, S.-H. Choi, E. Chu, Plane stress yield function for aluminum alloy sheets—part I: Theory, *International Journal of Plasticity* 19 (9) (2003) 1297–1319.
- [115] S. Tamura, S. Sumikawa, T. Uemori, H. Hamasaki, F. Yoshida, Experimental Observation of Elasto-Plasticity Behavior of Type 5000 and 6000 Aluminum Alloy Sheets, *MATERIALS TRANSACTIONS* 52 (5) (2011) 868–875.
- [116] J.-W. Yoon, F. Barlat, R.E. Dick, K. Chung, T.J. Kang, Plane stress yield function for aluminum alloy sheets—part II: FE formulation and its implementation, *International Journal of Plasticity* 20 (3) (2004) 495–522.
- [117] A. Güner, C. Soyarslan, A. Brosius, A.E. Tekkaya, Characterization of anisotropy of sheet metals employing inhomogeneous strain fields for Yld2000-2D yield function, *International Journal of Solids and Structures* 49 (25) (2012) 3517–3527.
- [118] D. Yanaga, T. Kuwabara, N. Uema, M. Asano, Material modeling of 6000 series aluminum alloy sheets with different density cube textures and effect on the accuracy of finite element simulation, *International Journal of Solids and Structures* 49 (25) (2012) 3488–3495.
- [119] T.B. Stoughton, J.W. Yoon, Sheet metal formability analysis for anisotropic materials under non-proportional loading, *International Journal of Mechanical Sciences* 47 (12) (2005) 1972–2002.
- [120] D. Daniel, C. Leppin, C. Lange, M. Gehrig, H. Gese, H. Dell, Formability Prediction of Aluminum Sheet for Car Body Panels. In: Nasder Asnafi (Hrsg.): *Proceedings of the IDDRG 2008*, 16.-18.06.2008, Olofström, Schweden.
- [121] M. Lechner, M. Johannes, A. Kuppert, M. Merklein, Influence of Pre-straining and Heat Treatment on the Yield Surface of Precipitation Hardenable Aluminum Alloys, *Physics Procedia* 56 (2014) 1400–1409.
- [122] ARGUS Software, available at <http://www.gom.com/3d-software/gom-system-software/argus-software.html> (accessed on January 6, 2017).
- [123] G. Spur, R. Neugebauer, H. Hoffmann, *Handbuch Umformen*, Carl Hanser Verlag GmbH & Company KG, 2012.
- [124] Bichiş, I Banabic, D Comşa, D.S, Research on the shock heat treatment method used for modifying the formability of aluminum alloys, *Annals of MTEM* (2011) 21–24.
- [125] Home | Aleris, available at <http://www.aleris.com/> (accessed on January 10, 2017).
- [126] Norm DIN EN 10002, Zugversuch, Teil 1, Prüfverfahren (bei Raumtemperatur). Berlin: Beuth-Verlag, 1991.
- [127] J.R. Davis, *Tensile testing*, 2nd ed., 2004.

References

- [128] R.H. Wagoner, J.-L. Chenot, Metal forming analysis, Cambridge University Press, Cambridge, 2001.
- [129] B07 Committee, Test Method for Shear Testing of Thin Aluminum Alloy Products, ASTM International, West Conshohocken, PA, 2005.
- [130] D. Staud, M. Merklein, M. Borsutzki, S. Geisler, Zug-Druck-Versuche an Miniaturproben zur Erfassung von Parametern für kinematische Verfestigungsmodelle, Tagungsband Werkstoffprüfung, Düsseldorf (2009), pp. 211–218.
- [131] Q. Yin, B. Zillmann, S. Suttner, G. Gerstein, M. Biasutti, A.E. Tekkaya, M.F.-X. Wagner, M. Merklein, M. Schaper, T. Halle, A. Brosius, An experimental and numerical investigation of different shear test configurations for sheet metal characterization, *International Journal of Solids and Structures* 51 (5) (2014) 1066–1074.
- [132] S. Keller, W. Hotz, H. Friebe, Yield curve determination using the bulge test combined with optical measurement. In: IDDRG 2009 international conference. Golden (2009), CO., Ohio.
- [133] NN (2008) Metallic materials – sheet and strip – determination of forming-limit-curves. ISO/FDIS 12004, International Standard, Final Draft.
- [134] DIL 805A/D/T Quenching Dilatomers – TA Instruments, available at <http://www.tainstruments.com/dil-805adt-quenching-dilatometers/> (accessed on January 14, 2017).
- [135] W. Weiß, M. Machhammer, F. Krall, R. Kolley, Simulation of the Hot Forming Process in Consideration of the Thermal State of the Tools, in: M. Oldenburg (Ed.), Proceedings: June 9 - 12, 2013, Luleå, Sweden, Verl. Wiss. Scripten, Auerbach, 2013, pp. 91–98.
- [136] K. Teichmann, C. D. Marioara, S. J. Andersen, K. O. Pedersen, S. M. K. Gulbrandsen-Dahl, M. Kolar, R. Holmestad, K. Marthinsen, HRTEM study of the effect of deformation on the early precipitation behaviour in an AA6060 Al–Mg–Si alloy. *Philosophical Magazine*, 2011, 91 (28) 3744–3754.
- [137] C.-H. Shen, Pre-treatment to Improve the Bake-hardening Response in the Naturally Aged Al-Mg-Si Alloy, *Journal of Materials Science & Technology* 27 (3) (2011) 205–212.
- [138] K. Wang, B. He, J.E. Carsley, R.S. Raghavan, J. Li, S.E. Hartfield-Wünsch, L. Zhang, Structure–property characterization of an age hardenable Al–Mg–Si alloy after straining and flash annealing, *Materials Science and Engineering: A* 595 (2014) 25–33.
- [139] F. Barlat, K. Lian, Plastic behavior and stretchability of sheet metals. Part I: A yield function for orthotropic sheets under plane stress conditions, *International Journal of Plasticity* 5 (1) (1989) 51–66.
- [140] D. Banabic, Advances in Plastic Anisotropy and Forming Limits in Sheet Metal Forming, *J. Manuf. Sci. Eng* 138 (9) (2016) 90801.
- [141] P. Jurco, D. Banabic, A user-friendly programme for calculating forming limit diagrams. In: Banabic D (ed) Proc. 8th ESAFORM Conference on Material

References

- Forming. Cluj-Napoca April 2005. The Publishing House of the Romanian Academy Bucharest, pp. 423–427.
- [142] D. Banabic, H. Aretz, D. S. Comsa, L. Paraianu, An improved analytical description of orthotropy in metallic sheets. *International Journal of Plasticity*, 21 (3) (2005) 493-512.
- [143] F. Barlat, J.W. Yoon, O. Cazacu, On linear transformations of stress tensors for the description of plastic anisotropy, *International Journal of Plasticity* 23 876–896.
- [144] 6016-T4 Aluminum MakeItFrom.com, available at <http://www.makeitfrom.com/material-properties/6016-T4-Aluminum> (accessed on March 6, 2017).
- [145] 1.1730 steel heat capacity - Google-Suche, available at https://www.google.at/search?q=tetrahedral+volume+mesh&biw=1164&bih=849&site=webhp&source=lnms&sa=X&ved=0ahUKEwiX1KC_9sHSAhXBPxQKHcdxCHwQ_AUIBygA&dpr=1.1#q=1.1730+steel+heat+capacity&* (accessed on March 6, 2017).
- [146] AGK Hochleistungswerkstoffe GmbH, hitzebeständige Nadelmatte - Nadelvliesmatten - Nadelfilzmatten, available at http://www.agk.de/html/isolierwerkstoffe/nadelvlies_matten.htm (accessed on March 7, 2017).
- [147] W.C. Emmens, J. Bottema, Friction of Aluminium in Deep Drawing; IDDRG CONGRESS 1998.